

# **ACOUSTIC TRANSDUCTION – MATERIALS AND DEVICES**

**Period 31 July 1996 to 31 December 1997**

**Annual Report**

**VOLUME V**

**OFFICE OF NAVAL RESEARCH  
Contract No: N00014-96-1-1173**

**APPROVED FOR PUBLIC RELEASE –  
DISTRIBUTION UNLIMITED**

**Reproduction in whole or in part is permitted for any  
purpose of the United States Government**

**Kenji Uchino**

**PENNS**STATE



---

**THE MATERIALS RESEARCH LABORATORY  
UNIVERSITY PARK, PA**

19980910 005



## GENERAL INSTRUCTIONS FOR COMPLETING SF 298

The Report Documentation Page (RDP) is used in announcing and cataloging reports. It is important that this information be consistent with the rest of the report, particularly the cover and title page. Instructions for filling in each block of the form follow. It is important to *stay within the lines* to meet optical scanning requirements.

**Block 1. Agency Use Only (Leave blank).**

**Block 2. Report Date.** Full publication date including day, month, and year, if available (e.g. 1 Jan 88). Must cite at least the year.

**Block 3. Type of Report and Dates Covered.** State whether report is interim, final, etc. If applicable, enter inclusive report dates (e.g. 10 Jun 87 - 30 Jun 88).

**Block 4. Title and Subtitle.** A title is taken from the part of the report that provides the most meaningful and complete information. When a report is prepared in more than one volume, repeat the primary title, add volume number, and include subtitle for the specific volume. On classified documents enter the title classification in parentheses.

**Block 5. Funding Numbers.** To include contract and grant numbers; may include program element number(s), project number(s), task number(s), and work unit number(s). Use the following labels:

C - Contract	PE - Project
G - Grant	TA - Task
PE - Program Element	WU - Work Unit Accession No.

**Block 6. Author(s).** Name(s) of person(s) responsible for writing the report, performing the research, or credited with the content of the report. If editor or compiler, this should follow the name(s).

**Block 7. Performing Organization Name(s) and Address(es).** Self-explanatory

**Block 8. Performing Organization Report Number.** Enter the unique alphanumeric report number(s) assigned by the organization performing the report.

**Block 9. Sponsoring/Monitoring Agency Name(s) and Address(es).** Self-explanatory.

**Block 10. Sponsoring/Monitoring Agency Report Number.** (If known)

**Block 11. Supplementary Notes.** Enter information not included elsewhere such as: Prepared in cooperation with...; Trans. of...; To be published in.... When a report is revised, include a statement whether the new report supersedes or supplements the older report.

**Block 12a. Distribution/Availability Statement.** Denotes public availability or limitations. Cite any availability to the public. Enter additional limitations or special markings in all capitals (e.g. NOFORN, REL, ITAR).

DOD - See DoDD 5230.24, "Distribution Statements on Technical Documents."

DOE - See authorities.

NASA - See Handbook NHB 2200.2.

NTIS - Leave blank.

**Block 12b. Distribution Code.**

DOD - Leave blank.

DOE - Enter DOE distribution categories from the Standard Distribution for Unclassified Scientific and Technical Reports.

NASA - Leave blank.

NTIS - Leave blank.

**Block 13. Abstract.** Include a brief (Maximum 200 words) factual summary of the most significant information contained in the report.

**Block 14. Subject Terms.** Keywords or phrases identifying major subjects in the report.

**Block 15. Number of Pages.** Enter the total number of pages.

**Block 16. Price Code.** Enter appropriate price code (NTIS only).

**Blocks 17. - 19. Security Classifications.** Self-explanatory. Enter U.S. Security Classification in accordance with U.S. Security Regulations (i.e., UNCLASSIFIED). If form contains classified information, stamp classification on the top and bottom of the page.

**Block 20. Limitation of Abstract.** This block must be completed to assign a limitation to the abstract. Enter either UL (unlimited) or SAR (same as report). An entry in this block is necessary if the abstract is to be limited. If blank, the abstract is assumed to be unlimited.

## ABSTRACT

The report documents work carried out over the period 31 July 1996 to 31 December 1997 on a Multi-University Research Initiative (MURI) program under Office of Naval Research (ONR) sponsorship. The program couples transducer materials research in the Materials Research Laboratory (MRL), design and testing studies in the Applied Research Laboratory (ARL) and vibration and flow noise control in the Center for Acoustics and Vibration (CAV) at Penn State.

The overarching project objective is the development of acoustic transduction materials and devices of direct relevance to Navy needs and with application in commercial products. The initial focus of studies is upon high performance sensors and high authority high strain actuators. This objective also carries the need for new materials, new device designs, improved drive and control strategies and a continuing emphasis upon reliability under a wide range of operating conditions.

In *Material Studies*, undoubtedly major breakthroughs have occurred in the ultra-high strain relaxor ferroelectric systems. Earlier reports of unusual piezoelectric activity in single crystal perovskite relaxors have been amply confirmed in the lead zinc niobate : lead titanate, and lead magnesium niobate : lead titanate systems for compositions of rhombohedral symmetry close to the Morphotropic Phase Boundary (MPB) in these solid solutions. Analysis of the unique properties of 001 field poled rhombohedral ferroelectric crystals suggests new intrinsic mechanisms for high strain and carries the first hints of how to move from lead based compositions. A major discovery of comparable importance is a new mode of processing to convert PVDF:TrFE copolymer piezoelectric into a relaxor ferroelectric in which electrostrictive strains of 4% have been demonstrated at high fields. Both single crystal and polymer relaxors appear to offer energy densities almost order of magnitude larger than in earlier polycrystal ceramic actuators.

*Transducer Studies* have continued to exploit the excellent sensitivity and remarkable versatility of the cymbal type flextensional element. Initial studies of a small cymbal arrays show excellent promise in both send and receive modes, and larger arrays are now under construction for tests at ARL. New studies in constrained layer vibration damping and in flow noise reduction are yielding exciting new results.

In *Actuator Studies*, an important advance in piezoelectric generated noise control now permits wider use of acoustic emission as a reliability diagnostic technique. Joint studies with NRL, Washington have developed a completely new  $d_{15}$  driven torsional actuator and the CAV program element has designed an exciting high strain high force inchworm.

Finite element analysis continues to be an important tool for understanding the more complex composite structures and their beam forming capability in water. *Thin and Thick Thin Film Studies* are gearing up to provide the material base for micro-tonpils arrays. New exploitation of ultra sensitive strain and permittivity measurements is providing the first reliable data of electrostriction in simple solids, and suggesting new modes for separating the polarizability contributors in dielectrics and electrostrictors.

## APPENDICES

### VOLUME I

#### GENERAL SUMMARY PAPERS

1. Ito, Y. and K. Uchino, Wiley Encyclopedia of Electrical and Electronics Engineering, J. G. Webster, Edit., (Partial Charge "Piezoelectricity"), John Wiley & Sons (1998). [in press].
2. Newnham, R.E., "Molecular Mechanisms in Smart Materials," MRS Bulletin (May 1997).
3. Swartz, S.L., T.R. Shrout, and T. Takenaka, "Electronic Ceramics R&D in the U.S., Japan, Part I: Patent History," The American Ceramic Society Bulletin **76** (8) (1997).

#### 2.0 MATERIALS STUDIES

##### 2.1 Polycrystal Perovskite Ceramics

4. Alberta, E.F., and A.S. Bhalla, "Piezoelectric Properties of  $\text{Pb}(\text{InNb})_{1/2}\text{O}_3\text{-PbTiO}_3$  Solid Solution Ceramics," J. Korean Phys. Soc. **32**, S1265-S1267 (February 1998).
5. Alberta, E.F. and A.S. Bhalla, "High Strain and Low Mechanical Quality Factor Piezoelectric  $\text{Pb}[\text{Sc}_{1/2}\text{Nb}_{1/2}]_{0.575}\text{Ti}_{0.425}\text{O}_3$  Ceramics" (1997).
6. Zhang, Q.M. and J. Zhao, "Polarization Responses in Lead Magnesium Niobate Based Relaxor Ferroelectrics," Appl. Phys. Lett. **71** (12, 1649-1651 (1997).
7. Glazounov, A.E., J. Zhao, and Q.M. Zhang, "Effect of Nanopolar Regions on Electrostrictive Coefficients of a Relaxor Ferroelectric," Proceedings Williamsburg Meeting, Williamsburg, Virginia (1998).
8. Zhao, J. A.E. Glazounov, Q.M. Zhang, and B. Toby, "Neutron Diffraction Study of Electrostrictive Coefficients of Prototype Cubic Phase of Relaxor Ferroelectric  $\text{PbMg}_{1/3}\text{Nb}_{2/3}\text{O}_3$ ," Appl. Phys. Lett. **72** (9), 1-3 (1998).
9. Park, S.-E., T.R. Shrout, P. Bridenbaugh, J. Rottenberg, and G.M. Loiacono, "Electric Field Induced Anisotropy in Electrostrictive  $\text{Pb}(\text{Mg}_{1/3}\text{Nb}_{2/3})\text{O}_3\text{-PbTiO}_3$  Crystals," Ferroelectrics (1997).
10. You, H. and Q.M. Zhang, "Diffuse X-Ray Scattering Study of Lead Magnesium Niobate Single Crystals," Phys. Rev. Lett. **79** (20), 3950-3953 (1997).
11. Zhao, J., V. Mueller, and Q.M. Zhang, "The Influence of the External Stress on the Electromechanical Response of Electrostrictive  $0.9\text{Pb}(\text{Mg}_{1/3}\text{Nb}_{2/3})\text{O}_3\text{-}0.1\text{PbTiO}_3$  in the DC Electrical Field Biased State," J. Mat. Res. (1998).

### VOLUME II

12. Yoon, S.-J., A. Joshi, and K. Uchino, "Effect of Additives on the Electromechanical Properties of  $\text{Pb}(\text{Zr,Ti})\text{O}_3\text{-Pb}(\text{Y}_{2/3}\text{W}_{1/3})\text{O}_3$  Ceramics," J. Am. Ceram. Soc **80** (4), 1035-39 (1997).
13. Hackenberger, W., M.-J. Pan, V. Vedula, P. Pertsch, W. Cao, C. Randall, and T. Shrout, "Effect of Grain Size on Actuator Properties of Piezoelectric Ceramics," Proceedings of the SPIE's 5th International Symposium on Smart Structures and Materials, San Diego, CA (March 1-5, 1998).

**THIS PAGE LEFT INTENTIONALLY BLANK**

## *Materials Studies—continued*

14. Mueller, V. and Q.M. Zhang, "Shear Response of Lead Zirconate Titanate Piezoceramics," *J. Appl. Phys.* (1998).
15. Park, S.-E., M.-J. Pan, K. Markowski, S. Yoshikawa, and L.E. Cross, "Electric Field Induced Phase Transition of Antiferroelectric Lead Lanthanum Zirconate Titanate Stannate Ceramics," *J. Appl. Phys.* **82** (4), 1798-1803 (1997).
16. Yoshikawa, S., K. Markowski, S.-E. Park, M.-J. Pan, and L.E. Cross, "Antiferroelectric-to-Ferroelectric Phase Switching Lead Lanthanum Zirconate Stannate Titanate (PLZST) Ceramics," Proceedings of SPIE's 4th Annual Symposium on Smart Structures and Materials, San Diego, CA (March 3-6, 1997).
17. Pan, M.-J., S.-E. Park, K.A. Markowski, W.S. Hackenberger, S. Yoshikawa, and L.E. Cross, "Electric Field Induced Phase Transition in Lead Lanthanum Stannate Zirconate Titanate (PLSnZT) Antiferroelectrics: Tailoring Properties through Compositional Modification" (1997).
18. Pan, M.-J., P. Pertsch, S. Yoshikawa, T.R. Shrout, and V. Vedula, "Electroactive Actuator Materials: Investigations on Stress and Temperature Characteristics," Proceedings of the SPIE's 5th International Symposium on Smart Structures and Materials, San Diego, CA (March 1-5, 1998).
19. Pan, M.-J. and S. Yoshikawa, "Effect of Grain Size on the Electromechanical Properties of Antiferroelectric-to-Ferroelectric Phase Switching PLSnZT Ceramics" (1997).

### *2.2 Relaxor Ferroelectric Single Crystal Systems*

20. Service, R.F., "Shape-Changing Crystals Get Shiftier," *Science* **275**, 1878 (28 March 1997).
21. Shrout, T.R., S.-E. Park, C.A. Randall, J.P. Shepard, L.B. Hackenberger, "Recent Advances in Piezoelectric Materials" (1997).
22. Park, S.-E. and T.R. Shrout, "Ultrahigh Strain and Piezoelectric Behavior in Relaxor Based Ferroelectric Single Crystals," *J. Appl. Phys.* **82** (4), 1804-1811 (1997).
23. Park, S.-E. and T. R. Shrout, "Characteristics of Relaxor-Based Piezoelectric Single Crystals for Ultrasonic Transducers," *IEEE Transactions, Ferroelectrics, and Frequency Control* **44** (5), 1140-1147 (1997).
24. Park, S.-E. and T.R. Shrout, "Relaxor Based Ferroelectric Single Crystals for Electro-Mechanical Actuators," *Mat. Res. Innov.* **1**, 20-25 (1997).
25. Park, S.-E., M.L. Mulvihill, G. Risch, and T.R. Shrout, "The Effect of Growth Conditions on the Dielectric Properties of  $\text{Pb}(\text{Zn}_{1/3}\text{Nb}_{2/3})\text{O}_3$  Single Crystals," *Jpn. J. Appl. Phys.* **36**, 1154-1158 (1997).
26. Mulvihill, M.L., L.E. Cross, W. Cao, and K. Uchino, "Domain-Related Phase Transitionlike Behavior in Lead Zinc Niobate Relaxor Ferroelectric Single Crystals," *J. Am. Ceram. Soc.* **80** (6), 1462-68 (1997).
27. Park, S.-E., P.D. Lopath, K.K. Shung, and T.R. Shrout, "Relaxor-Based Single Crystal materials for Ultrasonic Transducer Applications" (1997).
28. Lopath, P.D., S.-E. Park, K.K. Shung, and T.R. Shrout, " $\text{Pb}(\text{Zn}_{1/3}\text{Nb}_{2/3})\text{O}_3/\text{PbTiO}_3$  Single Crystal Piezoelectrics for Ultrasonic Transducers" (1997).
29. Lopath, P.D., S.-E. Park, K.K. Shung, and T.R. Shrout, "Single Crystal  $\text{Pb}(\text{Zn}_{1/3}\text{Nb}_{2/3})\text{O}_3/\text{PbTiO}_3$  (PZN/PT) in Medical Ultrasonic Transducers" (1997).

## *Materials Studies--continued*

### *2.3 New High Strain Polymer Materials*

30. Su, J., Q.M. Zhang, C.H. Kim, R.Y. Ting, and R. Capps, "Effect of Transitional Phenomena on the Electric Field Induced Strain-Electrostrictive Response of a Segmented Polyurethane Elastomer" (1997).
31. Su, J., Q.M. Zhang, and R.Y. Ting, "Space-Charge-Enhanced Electromechanical Response in Thin-Film Polyurethane Elastomers," *Appl. Phys. Lett* **71** (3), 386-388 (1997).

## **VOLUME III**

32. Su, J., Q.M. Zhang, P.-C. Wang, A.G. MacDiarmid, K.J. Wynne, "Preparation and Characterization of an Electrostrictive Polyurethane Elastomer with Conductive Polymer Electrodes," *Polymers for Adv. Tech.* (1998).
33. Zhang, Q.M., V. Bharti, and X. Zhao, "Giant Electrostriction and Relaxor Ferroelectric Behavior in Electron Irradiated Poly(vinylidene Fluoride-Trifluoroethylene) Copolymer," *Science* (1998).

### **3.0 TRANSDUCER STUDIES**

#### *3.1 Cymbal : Moonie : BB Composites*

34. Newnham, R.E., "Composite Sensors and Actuators" (1997).
35. Steele, B.CH., R.E. Newnham, and A.G. Evans, "Ceramics, Composites, and Intergrowth," *Current Opinion in Solid State & Materials Science* **2**, 563-565 (1997).
36. Tressler, J.F. S. Alkoy, and R.E. Newnham, "Piezoelectric Sensors and Sensor Materials" (1997).
37. Tressler, J.F., S. Alko, A. Dogan, and R.E. Newnham, "Functional Composites for Sensors, Actuators, and Transducers" (1997).
38. Dogan, A., K. Uchino, R.E. Newnham, "Composite Piezoelectric Transducer with Truncated Conical Endcaps 'Cymbal'," *IEEE Transactions on Ultrasonics, Ferroelectrics, and Frequency Control* **44** (3), 597-605 (1997).
39. Dogan, A., J.F. Fernandez, K. Uchino, and R.E. Newnham, "The 'Cymbal' Electromechanical Actuator" (1997).
40. Tressler, J.F., W. Cao, K. Uchino, and R.E. Newnham, "Ceramic-Metal Composite Transducers for Underwater Acoustic Applications" (1997).
41. Tressler, J.F. and R.E. Newnham, "Doubly Resonant Cymbal-Type Transducers," *IEEE Transactions on Ultrasonics, Ferroelectrics, and Frequency Control* **44** (5), 1175-1177 (1997).
42. Tressler, J.F., W. Cao, K. Uchino, and R.E. Newnham, "Finite Element Analysis of The Cymbal-Type Transducer" (1997).
43. Tressler, J.F., W.J. Hughes, W. Cao, K. Uchino, and R.E. Newnham, "Capped Ceramic Underwater Sound Projector" (1997).



**VOLUME IV**

- 44. Alkoy, S., P.D. Lopath, R.E. Newnham, A.-C. Hladky-Hennion, and J.K. Cochran, "Focused Spherical Transducers for Ultrasonic Imaging" (1997).
- 45. Alkoy, S., A. Dogan, A.-C. Hladky, P. Langlet, J.K. Cochran, and R.E. Newnham, "Miniature Piezoelectric Hollow Sphere Transducers (BBs)" (1997).
- 46. Zipparo, M.J., K.K. Shung, and T.R. Shrout, "Piezoceramics for High-Frequency (20 to 100 MHz) Single-Element Imaging Transducers," *IEEE Transactions on Ultrasonics, Ferroelectrics, and Frequency Control* **44** (5), 1038-1048 (1997).

**3.2 Frequency Agile Transducers**

- 47. Davis, C. and G.A. Lesieutre, "An Actively-Tuned Solid State Piezoelectric Vibration Absorber" (1997).
- 48. Davis, C.L., G.A. Lesieutre, and J. Dosch, "A Tunable Electrically Shunted Piezoceramic Vibration Absorber" (1997).
- 49. Lesieutre, G.A. and U. Lee, "A Finite Element for Beams Having Segmented Active Constrained Layers with Frequency-Dependent Viscoelastic Material Properties" (1997).
- 50. Hebert, C.A. and G.A. Lesieutre, "Rotocraft Blade Lag Damping Using Highly Distributed Tuned Vibration Absorbers," *American Institute of Aeronautics and Astronautics (AIAA 98-2001)*.
- 51. Lesieutre, G.A. and C.L. Davis, "Can a Coupling Coefficient of a Piezoelectric Device be Higher than Those of its Active Material?," *SPIE 4th Annual Symposium on Smart Structures and Materials, San Diego, CA (March 1997)*.

**3.3 3-D Acoustic Intensity Probes**

- 52. Lauchle, G.C., J.R. MacGillivray, and D.C. Swanson, "Active Control of Axial-flow Fan Noise," *J. Acoust. Soc. Am* **101** (1), 341-349 (1997).
- 53. McGuinn, R.S., G.C. Lauchle, and D.C. Swanson, "Low Flow-Noise Microphone for Active Noise Control Applications," *AIAA Journal* **35** (1), 29-34 (1997).
- 54. McGuinn, R.S., G.C. Lauchle, and D.C. Swanson, "Low Flow-Noise Pressure Measurements Using a "Hot-Mic," *AIAA -97-1665-CP*.
- 55. Capone, D.E., and G.C. Lauchle, "Designing a Virtual Sound-Level Meter in LabVIEW," *Education/Acoustics, LabVIEW, National Instruments*.

**VOLUME V**

**4.0 ACTUATOR STUDIES**

**4.1 Materials : Designs : Reliability**

- 56. Uchino, K., "Piezoelectric Actuators" (1997).
- 57. Uchino, K., "Overview: Materials Issues in Design and Performance of Piezoelectric Actuators," *SPIE Mtg.* (1997).
- 58. Uchino, K., "Shape Memory Ceramics," Chapter 8 (1997).

### *Actuator Studies—continued*

59. Aburatani, H., S. Yoshikawa, K. Uchino, and J.W.C. deVries, "A Study of Acoustic Emission in Piezoelectric Multilayer Ceramic Actuator," *Jpn. J. Appl. Phys.* **37**, 204-209 (1998).
60. Aburatani, H. and K. Uchino, "Acoustic Emission (AE) Measurement in Piezoelectric Ceramics" (1997).
61. Aburatani, H. and K. Uchino, "The Application of Acoustic Emission (AE) Method for Ferroelectric Devices and Materials," 8th US-Japan Seminar (1997).
62. Uchino, K., "Reliability of Ceramic Actuators" (1997).

### *4.2 Photostrictive Actuators*

63. Tonooka, K. P. Poosanaas, and K. Uchino, "Mechanism of the Bulk Photovoltaic Effect in Ferroelectrics," Proceedings of the 5th SPIE Mtg., San Diego, CA (1998).
64. Poosanaas, P. A. Dogan, S. Thakoor, and K. Uchino, "Dependence of Photostriction on Sample Thickness and Surface Roughness for PLZT Ceramics," Proceedings of the 1997 IEEE Ultrasonics Symposium, Toronto, Ontario, Canada (October 1997).
65. Poosanaas, P. A. Dogan, A.V. Prasadaraao, S. Komarneni, and K. Uchino, "Photostriction of Sol-Gel Processed PLZT Ceramics," *J. Electroceramics* **1** (1), 105-111 (1997).

## **VOLUME VI**

66. Poosanaas, P., A. Dogan, A.V. Prasadaraao, S. Komarneni, and K. Uchino, "Effect of Ceramic Processing Methods on Photostrictive Ceramics," *J. Adv. Perf. Mat.* (1997).
67. Thakoor, S., P. Poosanaas, J.M. Morookian, A. Yavrovian, L. Lowry, N. Marzwell, J. Nelson, R.R. Neurgaonkar, and K. Uchino, "Optical Microactuation in Piezoceramics" (1997).

### *4.3 New Torsional Amplifier/Actuators*

68. Glazounov, A.E., Q.M. Zhang, and C. Kim, "Piezoelectric Actuator Generating Torsional Displacement from Piezoelectric  $d_{15}$  Shear Response," *Appl Phys. Lett.* (1997).
69. Glazounov, A.E., Q.M. Zhang, and C. Kim, "A New Torsional Actuator Based on Shear Piezoelectric Response," Proceedings of SPIE Smart Materials, San Diego, CA (March 1998).

### *4.4 High Force Amplifiers and Inchworms*

70. Uchino, K., J. Zheng, A. Joshi, S. Yoshikawa, S. Hirose, S. Takahashi, and J.W.C. deVries, "High Power Characterization of Piezoelectric Materials" (1997).
71. Uchino, K., "High Electromechanical Coupling Piezoelectrics - How High Energy Conversion Rate is Possible," *Mat. Res. Soc. Symp. Proc.* **459**, 3-14 (1997).
72. Park, S.-E., V. Vedula, M.-J. Pan, W.S. Hackenberger, P. Pertsch, and T.R. Shrout, "Relaxor Based Ferroelectric Single Crystals for Electromechanical Actuators," Proceedings of the SPIE's 5th International Symposium on Smart Structures and Materials, San Diego, CA (March 1998).

### *Actuator Studies—continued*

73. Koopmann, G.H. G.A. Lesieutre, B.R. Dershem, W. Chen, and S. Yoshikawa, "Embeddable Induced Strain Actuators Using Framed 3-3 Piezoceramic Stacks: Modeling and Characterization," Proceedings of the SPIE's 4th Annual International Symposium on Smart Structures and Materials, San Diego, CA (March 1997).
74. Driesch, P.L., G.H. Koopmann, J. Dosch, and H. Iwata, "Development of a Surface Intensity Probe for Active Control Applications," IMECE, Dallas, Texas (November 1997).
75. Galante, T., J. Frank, J. Bernard, W. Chen, G.A. Lesieutre, and G.H. Koopmann, "Design, Modeling, and Performance of a High Force Piezoelectric Inchworm Motor" (1997).
76. Galante, T.P., "Design and Fabrication of a High Authority Linear Piezoceramic Actuator: The PSU H3 Inchworm," Master of Science Thesis, The Pennsylvania State University (August 1997).
77. Lesyna, M.W., "Shape Optimization of a Mechanical Amplifier for Use in a Piezoceramic Actuator," Master of Science Thesis, The Pennsylvania State University (May 1998).

## **VOLUME VII**

78. Uchino, K., "Piezoelectric Ultrasonic Motors: Overview," J. Smart Materials and Structures—Special Issue (1997).
79. Uchino, K., "Compact Piezoelectric Ultrasonic Motors," J. Medical Ultrasonics 24 (9), 1191-92 (1997).

### **5.0 MODELING and CHARACTERIZATION**

#### **5.1 Finite Element Methods**

80. Qi, W. and W. Cao, "Finite Element Analysis and Experimental Studies on the Thickness Resonance of Piezocomposite Transducer," Ultrasonic Imaging 18, 1-9 (1996).
81. Qi, W. and W. Cao, "Finite Element Study on Random Design of 2-2 Composite Transducer," SPIE 3037, 176-180 (1997).
82. Geng, X. and Q.M. Zhang, "Evaluation of Piezocomposites of Ultrasonic Transducer Applications—Influence of the Unit Cell Dimensions and the Properties of Constituents on the Performance of 2-2 Piezocomposites," IEEE Transactions on Ultrasonics, Ferroelectrics, and Frequency Control 44 (4), 857-872 (1997).
83. Zhang, Q. and X. Geng, "Acoustic Properties of the Interface of a Uniform Medium-2-2 Piezocomposite and the Field Distributions in the Composite," Jpn. J. Appl. Phys. 36, 6853-6861 (1997).
84. Geng, X. and Q.M. Zhang, "Analysis of the Resonance Modes and Losses in 1-3 Composites for Ultrasonic Transducer Applications," IEEE UFFC (1997).

# **ACTUATOR STUDIES**

# **Materials : Designs : Reliability**

# **APPENDIX 56**

## **Piezoelectric Actuators**

**Kenji Uchino**

**International Center for Actuators and Transducers**

**Materials Research Laboratory**

**The Pennsylvania State University**

**University Park, PA 16802, USA**

Piezoelectric and electrostrictive devices have become key components in smart actuator/sensor systems such as precision positioners, miniature ultrasonic motors and adaptive mechanical dampers. This article reviews developments of piezoelectric and related ceramic actuators with particular focus on the improvement of actuator materials, device designs and drive/control techniques of actuators. Developments will be compared among USA, Japan and Europe.

### Trends in Micro-Mechatronics

Piezoelectric actuators are forming a new field between electronic and structural ceramics [1-4]. Application fields are classified into three categories: positioners, motors and vibration suppressors. The manufacturing precision of optical instruments such as lasers and cameras, and the positioning accuracy for fabricating semiconductor chips, which must be adjusted using solid-state actuators, is of the order of  $0.1\text{ }\mu\text{m}$ . Regarding conventional electromagnetic motors, tiny motors smaller than  $1\text{ cm}^3$  are often required in office or factory automation equipment and are rather difficult to produce with sufficient energy efficiency. Ultrasonic motors whose efficiency is insensitive to size are superior in the mini-motor area. Vibration suppression in space structures and military vehicles using piezoelectric actuators is also a promising technology.

New solid-state displacement transducers controlled by temperature (shape memory alloy) or magnetic field (magnetostrictive alloy) have been proposed, but are generally inferior to the piezoelectric/electrostrictive ceramic actuators because of technological trends aimed at reduced driving power and miniaturization [4].



Actuator materials are classified into three categories; piezoelectric, electrostrictive and phase-change materials. Modified lead zirconate titanate [PZT,  $\text{Pb}(\text{Zr,Ti})\text{O}_3$ ] ceramics are currently the leading materials for piezoelectric applications. The PLZT [ $(\text{Pb,Lu})(\text{Zr,Ti})\text{O}_3$ ] 7/62/38 compound is one such composition [5]. The strain curve is shown in Fig.1(a) left. When the applied field is small, the induced strain  $x$  is nearly proportional to the field  $E$  ( $x = d E$ , where  $d$  is called the piezoelectric constant). As the field becomes larger (i.e., greater than about 1 kV/cm), however, the strain curve deviates from this linear trend and significant hysteresis is exhibited due to polarization reorientation. This sometimes limits the usage of such materials in actuator applications that require nonhysteretic response.

An interesting new family of actuators has been fabricated in Germany from a barium stannate titanate system [ $\text{Ba}(\text{Sn,Ti})\text{O}_3$ ] [6]. The useful property of  $\text{Ba}(\text{Sn}_{0.15}\text{Ti}_{0.85})\text{O}_3$  is its unusual strain curve, in which the domain reorientation occurs only at low fields, and there is then a long linear range at higher fields (Fig.1(a) right); i.e., the coercive field is unusually small. Moreover, this system is particularly intriguing since it contains no Pb ions, an essential feature as ecological concerns grow in the future.

The second category of actuators is based on electrostriction as in PMN [ $\text{Pb}(\text{Mg}_{1/3}\text{Nb}_{2/3})\text{O}_3$ ] based ceramics, developed in USA. Although a second-order phenomenon of electromechanical coupling ( $x = M E^2$ , where  $M$  is called electrostrictive constant), it can be extraordinarily large (more than 0.1 %) [7]. An attractive feature of these materials is the near absence of hysteresis (Fig.1(b)). The superiority of PMN to PZT was demonstrated in a Scanning Tunneling

Microscope (STM) [8]. The PMN actuator could provide extremely small distortion of the image even when the probe was scanned in the opposite direction.

The third category is based on phase-change-related strains, i. e. polarization-induced by switching from an antiferro-electric to a ferroelectric state, as systematically investigated by our group[9]. Figure 1(c) shows the field-induced strain curves taken for the lead zirconate stannate based system  $[\text{Pb}_{0.99}\text{Nb}_{0.02}((\text{Zr}_x\text{Sn}_{1-x})_{1-y}\text{Ti}_y)\text{O}_3]$ . The longitudinally induced strain reaches more than 0.3 %, which is much larger than that expected in normal piezoelectrics or electrostrictors. A rectangular-shape hysteresis in Fig.1(c) left, referred to as a "digital displacement transducer" because of the two on/off strain states, is interesting. Moreover, this field-induced transition exhibits a shape memory effect in appropriate compositions (Fig.1(c) right). Once the ferroelectric phase has been induced, the material "memorizes" its ferroelectric state even under zero-field conditions, although it can be erased with the application of a small reverse bias field [10]. This shape memory ceramic is used in energy saving actuators. A latching relay in Fig.2 is composed of a shape memory ceramic unimorph and a mechanical snap action switch, which is driven by a pulse voltage of 4 ms duration. Compared with the conventional electromagnetic relays, the new relay is much simple and compact in structure with almost the same response time.

### Novel Actuator Materials

A monomorph device has been developed to replace the conventional bimorphs, with simpler structure and manufacturing process. The principle is a superposed effect of piezoelectricity and semiconductivity [11]. As shown in Fig.3, the contact between a semiconductor and a metal (Schottky barrier) causes non-uniform distribution of the electric field, even in a compositionally uniform ceramic. When we apply an external voltage to this semiconductor plate, the field is generated only on one side of the plate. Suppose that the ceramic possesses also piezoelectricity,

only one side of a ceramic plate tends to contract, leading to a bending deformation in total. A monomorph plate with 30 mm in length and 0.5 mm in thickness can generate 200  $\mu\text{m}$  tip displacement, in equal magnitude of that of the conventional bimorphs [12]. The "rainbow" actuator by Aura Ceramics [13] is a modification of the above-mentioned semiconductive piezoelectric monomorphs, where half of the piezoelectric plate is reduced, rendering it semiconducting. This leads to bending of a total monomorph ceramic plate.

A photostrictive actuator is a fine example of an intelligent material, incorporating "illumination sensing" and self production of "drive/control voltage" together with final "actuation." In certain ferroelectrics, a constant electromotive force is generated with exposure to light, and a photostrictive strain results from the coupling of this bulk photovoltaic effect to inverse piezoelectricity. A bimorph unit has been made from PLZT 3/52/48 ceramic doped with tungsten [14]. The remnant polarization of one PLZT layer is parallel to the plate and in the direction opposite to that of the other plate. Upon irradiation with violet light onto one side of the PLZT bimorph, a photovoltage of 1 kV/mm is generated, causing a bending motion. The tip displacement of a 20 mm long bimorph with 0.4 mm in thickness is 150  $\mu\text{m}$ , with a response time of 1 s.

A photo-driven micro walking device has been developed [15]. As shown in Fig.4, it is simple in structure, having neither lead wires nor electric circuitry, with two bimorph legs fixed to a plastic board. When the legs are alternately irradiated with light, the device moves like an inchworm with a speed of 100 mm/min.

PZT:polymer composites play a key role in the design of transducers such as sonars with both actuator and sensor functions [16]. In general, two-phase composites can be categorized, according to the connectivity of each phase (1, 2 or 3 dimensionality), into 10 classes. Most popular composites are the 3-0 type, which is fabricated from a polymer matrix mixed with PZT ceramic powder, and the 3-1 composite which is composed of PZT fibers embedded in a polymer

matrix. A great enhancement in the effective piezoelectric (sensor) coefficient  $g^*$  can be expected in the composites while keeping the effective piezoelectric (actuator) coefficient  $d^*$  almost the same as  $d$  of the PZT itself. Although the PZT composites are very useful for acoustic transducer applications, care must be taken when using them in actuator applications. Under an applied dc field, the field induced strain exhibits a large hysteresis and creep, because of the viscoelastic property of the polymer matrix. More serious problems are found when they are driven under a high ac field; that is, heat generation. The heat generated by the ferroelectric hysteresis in the piezoceramic can not be dissipated easily due to the very low thermal conduction of the polymer matrix, which results in rapid degradation of piezoelectricity.

Another intriguing application of PZT composites is as a passive mechanical damper, where mechanical noise vibration is radically suppressed by the converted electric energy dissipation through Joule heat when a suitable resistance, equal to an impedance of the piezoelectric element  $1/\omega C$ , is connected to the piezo-element [17]. Piezoceramic:carbon black:polymer composites are promising useful designs for practical application. Figure 5 shows the damping time constant change with volume percentage of the carbon black. The minimum time constant (i.e. quickest damping) is obtained at 6 % carbon black, where a drastic electric conductivity change is observed (percolation threshold) [18].

### Actuator Designs

Two of the most popular actuator designs are multilayers [19] and bimorphs (see Fig.6). The multilayer, in which roughly 100 thin piezoelectric/electrostrictive ceramic sheets are stacked together, has advantages in low driving voltage (100 V), quick response (10  $\mu$ s), high generative force (1000 N) and high electromechanical coupling. But the displacement in the range of 10  $\mu$ m is not sufficient for some applications. This contrasts with the bimorph, consisting of multiple

piezoelectric and elastic plates bonded together to generate a large bending displacement of several hundred  $\mu\text{m}$ , but the response (1 ms) and the generative force (1 N) are low.

A 3-D positioning actuator with a stacked structure was also proposed by a German company as in Fig.7, where shear strain was utilized to generate the x and y displacements [20]. Polymer-packed PZT bimorphs have been commercialized in USA, aiming at vibration reduction/control applications in smart structures[21].

A composite actuator structure called the "moonie" (or "cymbal") has been developed at Penn State University to provide characteristics intermediate between the multilayer and bimorph actuators; this transducer exhibits an order of magnitude larger displacement than the multilayer, and much larger generative force with quicker response than the bimorph [22]. The device consists of a thin multilayer piezoelectric element and two metal plates with narrow moon-shaped cavities bonded together as shown in Fig.6. The moonie with a size of  $5 \times 5 \times 2.5 \text{ mm}^3$  can generate a  $20 \mu\text{m}$  displacement under 60 V, eighth times as large as the generative displacement of the multilayer with the same size [23]. This new compact actuator has been applied to make a miniaturized laser beam scanner.

### Drive/Control Techniques

Piezoelectric/electrostrictive actuators may be classified into two categories, based on the type of driving voltage applied to the device and the nature of the strain induced by the voltage (Fig.8): (1) rigid displacement devices for which the strain is induced unidirectionally along an applied dc field, and (2) resonating displacement devices for which the alternating strain is excited by an ac field at the mechanical resonance frequency (ultrasonic motors). The first can be further divided into two types: servo displacement transducers (positioners) controlled by a feedback system through a

position-detection signal, and pulse-drive motors operated in a simple on/off switching mode, exemplified by dot-matrix printers.

The materials requirements for these classes of devices are somewhat different, and certain compounds will be better suited to particular applications. The ultrasonic motor, for instance, requires a very hard type piezoelectric with a high mechanical quality factor  $Q$ , leading to the suppression of heat generation. Driving the motor at the antiresonant frequency, rather than at the resonant state, is also an intriguing technique to reduce the load on the piezo-ceramic and the power supply [24]. The servo-displacement transducer suffers most from strain hysteresis and, therefore, a PMN electrostrictor is used for this purpose. The pulse-drive motor requires a low permittivity material aiming at quick response with a certain power supply rather than a small hysteresis so that soft PZT piezoelectrics are preferred to the high-permittivity PMN for this application.

Pulse drive techniques for ceramic actuators are very important for improving the response of the device [25,26]. Figure 9 shows transient vibrations of a bimorph excited after a pseudo-step voltage is applied. The rise time is varied around the resonance period ( $n$  is the time scale with a unit of  $T_0/2$ , where  $T_0$  stands for the resonance period). It is concluded that the overshoot and ringing of the tip displacement is completely suppressed when the rise time is precisely adjusted to the resonance period of the piezo-device (i. e. for  $n = 2$ ) [25]. A flight actuator was developed using a pulse-drive piezoelectric element and a steel ball. A  $5\text{ }\mu\text{m}$  rapid displacement induced in a multilayer actuator can hit a 2 mm steel ball up to 20 mm in height [25]. A dot-matrix printer head has been developed using a flight actuator as shown in Fig.10 [27]. By changing the drive voltage pulse width, the movement of the armature was easily controlled to realize no vibrational ringing or double hitting.

## Device Applications

Table I compares the difference in the ceramic actuator developments among USA, Japan and Europe. The details will be described in this section.

### USA

The target of the development is mainly for military-oriented applications such as vibration suppression in space structures and military vehicles. Notice the up-sizing trend of the actuators for these purposes.

A typical example is found in a space truss structure proposed by Jet Propulsion Laboratory [28]. A stacked PMN actuator was installed at each truss nodal point and operated so that unnecessary mechanical vibration was suppressed immediately. A "hubble" telescope has also been proposed using multilayer PMN electrostrictive actuators to control the phase of the incident light wave in the field of optical information processing (Fig.11) [29]. The PMN electrostrictor provided superior adjustment of the telescope image because of negligible strain hysteresis.

The US Army is interested in developing a rotor control system in helicopters. Figure 12 shows a bearingless rotor flexbeam with attached piezoelectric strips [30]. Various types of PZT-sandwiched beam structures have been investigated for such a flexbeam application and for active vibration control [31].

Japanese industries seek to develop mass-consumer products, with the categories limited to mini-motor and positioner areas, with applications to office equipment and cameras/video cameras. In that sense, tiny actuators smaller than  $1\text{ cm}^3$  are the main focus.

A dot matrix printer is the first widely-commercialized product using ceramic actuators. Each character formed by such a printer is composed of a  $24 \times 24$  dot matrix. A printing ribbon is subsequently impacted by a multiwire array. A sketch of the printer head appears in Fig.13(a) [32]. The printing element is composed of a multilayer piezoelectric device, in which 100 thin ceramic sheets  $100\text{ }\mu\text{m}$  in thickness are stacked, together with a sophisticated magnification mechanism (Fig.13(b)). The magnification unit is based on a monolithic hinge lever with a magnification of 30, resulting in an amplified displacement of  $0.5\text{ mm}$  and an energy transfer efficiency greater than 50 %. A piezoelectric camera shutter is currently the largest production item (Fig.14). A piece of piezoelectric bimorph can open and close the shutter in a milli-second through a mechanical wing mechanism [33]. Piezoelectric gyro-sensors are now widely used to detect the noise motion of a handy video camera. Figure 15 shows a Tokin cylinder type gyroscope [34]. Among the 6 electrode strips, two of them are used to excite total vibration and the other two pairs of electrode are used to detect the Coriolis force or the rotational acceleration cause by the hand motion. By using the gyro signal, the image vibration can be compensated electrically on a monitor display.

Efforts have been made to develop high-power ultrasonic vibrators as replacements for conventional electromagnetic motors [35]. The ultrasonic motor is characterized by "low speed and high torque," which is contrasted with "high speed and low torque" of the electromagnetic motors. Two categories are being investigated in Japan for ultrasonic motors: a standing-wave type and a propagating-wave type.



The standing-wave type is sometimes referred to as a vibratory-coupler type or a "woodpecker" type, where a vibratory piece is connected to a piezoelectric driver and the tip portion generates flat-elliptical movement. Attached to a rotor or a slider, the vibratory piece provides intermittent rotational torque or thrust. The standing-wave type has, in general, high efficiency, but lack of control in both clockwise and counterclockwise directions is a problem. An ultrasonic linear motor equipped with a multilayer piezoelectric actuator and fork-shaped metallic legs has been developed as shown in Fig.16 [36]. Since there is a slight difference in the mechanical resonance frequency between the two legs, the phase difference between the bending vibrations of both legs can be controlled by changing the drive frequency. The walking slider moves in a way similar to a horse using its fore and hind legs when trotting. A trial motor  $20 \times 20 \times 5 \text{ mm}^3$  in dimension exhibited a maximum speed of 20 cm/s and a maximum thrust of 0.2 kgf with a maximum efficiency of 20 %, when driven at 98 kHz of 6 V (actual power = 0.7 W). This motor has been employed in a precision X-Y stage.

By comparison, the propagating-wave type (a surface-wave or "surfing" type) combines two standing waves with a 90 degree phase difference both in time and in space, and is controllable in both rotational directions (Fig.17) [37]. By means of the traveling elastic wave induced by the thin piezoelectric ring, a ring-type slider in contact with the "rippled" surface of the elastic body bonded onto the piezoelectric is driven in both directions by exchanging the sine and cosine voltage inputs. Another advantage is its thin design, which makes it suitable for installation in cameras as an automatic focusing device. 80 % of the exchange lenses in Canon "EOS" camera series have already been replaced by the ultrasonic motor mechanism.

Europe

Ceramic actuator development has begun relatively recently in Europe, and the research topics range widely. The current focus by major manufacturers is directed towards products such as lab-stages and steppers with sophisticated structures.

Figure 18 shows a walking piezo motor with 4 multilayer actuators [38]. The two shorter actuators function as clamps and the longer two provide the movement by an inchworm mechanism.

### Future of Ceramic Actuators

20 years have passed since the intensive development of piezoelectric actuators began in Japan, then spread worldwide. The focus has now shifted to practical device applications.

The markets in the USA are limited to military and defense applications, and it is difficult to estimate the sales amount. The current needs from the Navy are smart submarine skins, hydrophone actuators, propeller noise cancellation etc., from the Air Force smart aircraft skins, while the Army requires helicopter rotor twisting, aeroservoelastic control and cabin noise/seat vibration cancellation.

In Japan, piezoelectric camera shutters (Minolta Camera) and automatic focusing mechanisms in cameras (Canon), dot-matrix printers (NEC) and part-feeders (Sanki) are now being commercialized and mass-produced by tens of thousands of pieces per month. A number of patents have been disclosed particularly by NEC, TOTO Corporation, Matsushita Electric, Brother Industry, Toyota Motors, Tokin, Hitachi Metal, and Toshiba.

We estimate the annual sales in 2005 in Japan, of ceramic actuator units, camera-related devices and ultrasonic motors to reach \$500 million, \$300 million and \$150 million, respectively [39]. These are installed in final actuator-related products, likely reaching \$10 billion.

Future research trends will be divided into two ways: up-sizing in space structures and down-sizing in office equipment. Further down-sizing will also be required in medical diagnostic applications such as blood test kits and surgical catheters. The Penn State University is developing separate component motors with a diameter as small as 3 mm, using a "windmill" shape torsional vibration coupler, which provide a torque around 0.1 mN·m [40]. Piezoelectric thin films compatible with silicon technology will be of much focus in micro-electromechanical systems. An ultrasonic rotary motor as tiny as 2 mm in diameter, fabricated on a silicon membrane is a good example (see Fig.19) [41]. However, these thin/thick film actuators cannot separately be used and the whole device size is relatively large. Photo-driven actuators with remote control capability will be developed not only for light-weight flexible space structures, but also for micro-robot applications.

With expansion of applications of ceramic actuators, durability and reliability become more important. The final goal is to develop much tougher actuator ceramics mechanically and electrically. However, the reliability can be improved significantly if the degradation mechanisms can be monitored.

Safety systems or health monitoring systems have been proposed with two feedback mechanisms: position feedback which can compensate position drift and hysteresis, and breakdown detection feedback which can stop the actuator system safely without causing any serious damage onto the work, e.g. in a lathe machine [42]. Acoustic emission and internal potential measurements, and resistance monitoring of a strain-gauge type internal electrode embedded in a piezo-actuator under a cyclic electric field drive are good predictors of life time [43].

## Bibliography

- [1] K.Uchino, *Piezoelectric/Electrostrictive Actuators*, Morikita Publishing, Tokyo (1986)
- [2] K.Uchino, Bull.Am.Ceram.Soc., **65**(4), 647 (1986)
- [3] K.Uchino, MRS Bull., **18**(4), 42 (1993)
- [4] K.Uchino, *Piezoelectric Actuators and Ultrasonic Motors*, Kluwer Academic Publishers, MA (1996)
- [5] K.Furuta and K.Uchino, Adv.Ceram.Mater., **1**, 61 (1986)
- [6] J.von Cieminski and H.Beige, J.Phys.D, **24**, 1182 (1991)
- [7] L.E.Cross, S.J.Jang, R.E.Newnham, S.Nomura and K.Uchino, Ferroelectrics, **23**(3), 187 (1980)
- [8] K.Uchino, Ceramic Data Book'88 (Chap.:Ceramic Actuators), Inst. Industrial Manufacturing Tech., Tokyo (1988)
- [9] K.Uchino and S.Nomura, Ferroelectrics, **50**(1), 191 (1983)
- [10] A.Furuta, K.Y.Oh and K.Uchino, Sensors and Mater., **3**(4), 205 (1992)
- [11] K.Uchino, M.Yoshizaki, K.Kasai, H.Yamamura, N.Sakai and H.Asakura, Jpn. J. Appl. Phys., **26**(7), 1046 (1987)
- [12] K.Uchino, M.Yoshizaki and A.Nagao, Ferroelectrics, **95**, 161 (1989)
- [13] Aura Ceramics, Inc., Catalogue "Rainbow"
- [14] M.Tanimura and K.Uchino, Sensors and Mater., **1**, 47 (1988)
- [15] K.Uchino, J.Rob.Mech., **1**(2), 124 (1989)
- [16] K.Uchino, S.Nomura and R.E.Newnham, Sensor Tech. **2**, No.7, 81 (1982)
- [17] K.Uchino and T.Ishii, J.Jpn.Ceram.Soc., **96**(8), 863 (1988)
- [18] Y.Suzuki, K.Uchino, H.Gouda, M.Sumita, R.E.Newnham and A.R.Ramachandran, J.Jpn.Ceram.Soc., **99**(11), 1135 (1991)

- [19] S. Takahashi, A. Ochi, M. Yonezawa, T. Yano, T. Hamatsuki and I. Fujui, *Ferroelectrics*, **50**, 181 (1993)
- [20] A. Bauer and F. Moller, *Proc. 4th Int'l Conf. New Actuators, Germany*, p.128 (1994)
- [21] Active Control Experts, Inc. Catalogue "PZT Quick Pack" (1996)
- [22] Y. Sugawara, K. Onitsuka, S. Yoshikawa, Q.C. Xu, R.E. Newnham and K. Uchino, *J. Am. Ceram. Soc.*, **75**(4), 996 (1992)
- [23] H. Goto, K. Imanaka and K. Uchino, *Ultrasonic Techno*, **5**, 48 (1992)
- [24] N. Kanbe, M. Aoyagi, S. Hirose and Y. Tomikawa, *J. Acoust. Soc. Jpn. (E)*, **14**(4), 235 (1993)
- [25] S. Sugiyama and K. Uchino, *Proc. Int'l. Symp. Appl. Ferroelectrics'86*, IEEE, p.637 (1986)
- [26] C. Kusakabe, Y. Tomikawa and T. Takano, *IEEE Trans. UFFC*, **37**(6), 551 (1990)
- [27] T. Ota, T. Uchikawa and T. Mizutani, *Jpn. J. Appl. Phys.*, **24**, Suppl.24-3, 193 (1985)
- [28] J.T. Dorsey, T.R. Sutter and K.C. Wu, *Proc. 3rd Int'l Conf. Adaptive Structures*, p.352 (1992)
- [29] B. Wada, *JPL Document D-10659*, p.23 (1993)
- [30] F.K. Straub, *Smart Mater. Struct.*, **5**, 1 (1996)
- [31] P.C. Chen and I. Chopra, *Smart Mater. Struct.*, **5**, 35 (1996)
- [32] T. Yano, E. Sato, I. Fukui and S. Hori, *Proc. Int'l Symp. Soc. Information Display*, p.180 (1989)
- [33] Y. Tanaka, *Handbook on New Actuators for Precision Control*, Fuji Technosystem, p.764 (1994)
- [34] H. Abe, T. Yoshida and K. Tsuruga, *Jpn. J. Appl. Phys.*, **31**, 3061 (1992)
- [35] S. Ueha and Y. Tomikawa, *Ultrasonic Motors*, Clarendon Press, Oxford (1993)
- [36] M. Tohda, S. Ichikawa, K. Uchino and K. Kato, *Ferroelectrics*, **93**, 287 (1989)
- [37] Y. Akiyama (Editor), *Ultrasonic Motors/Actuators*, Triceps, Tokyo (1986)
- [38] M.P. Koster, *Proc. 4th Int'l Conf. New Actuators, Germany*, p.144 (1994)
- [39] K. Uchino, *Proc. 9th Int'l Symp. Appl. Ferroelectrics*, p.319 (1995)

- [40] B.Koc: Ph.D. Thesis, Electr. Engin. Dept., Penn State University, University Park (1998)  
[in press]
- [41] A.M.Flyn, L.S.Tavrow, S.F.Bart, R.A.Brooks, D.J.Ehrlich, K.R.Udayakumar and  
L.E.Cross, J. Microelectromechanical Systems, **1**, 44 (1992)
- [42] K.Uchino, J.Industrial Education Soc. Jpn., **40**, 28 (1992)
- [43] K.Uchino and H.Aburatani, Proc. 2nd Int'l Conf. Intelligent Materials, p.1248 (1994)

## Figure Captions

**Fig.1** Electric field-induced strains in ceramics; (a) Piezoelectric  $(\text{Pb},\text{La})(\text{Zr},\text{Ti})\text{O}_3$  and  $\text{Ba}(\text{Sn},\text{Ti})\text{O}_3$ . (b) Electrostrictive  $\text{Pb}(\text{Mg}_{1/3}\text{Nb}_{2/3},\text{Ti})\text{O}_3$ . (c) Phase-change material  $\text{Pb}(\text{Zr},\text{Sn},\text{Ti})\text{O}_3$ .

**Fig.2** Latching relay using a shape memory ceramic unimorph. The drive requires a 4 ms pulse voltage, not a continuous voltage, which provides a  $150\text{ }\mu\text{m}$  tip displacement to the unimorph.

**Fig.3** Electron energy band (Schottky barrier) model in monomorph devices (n-type semiconductor). When an external voltage is applied to this semiconductor plate, the field is generated only on one side (cathode) of the plate. Through its piezoelectricity, only cathode side of a ceramic plate tends to contract, leading to a bending deformation in total.

**Fig.4** Structure of a photo-driven walking device and the illumination directions. Each leg is composed of two photostrictive PLZT plates bonded together, with the remnant polarization of one ceramic layer parallel to the plate and in the direction opposite to that of the other plate.

**Fig.5** Damping time constant change with volume percentage of carbon black in piezoelectric composite dampers. The minimum time constant (quickest damping) is obtained at the percolation threshold.

**Fig.6** Typical designs for ceramic actuators: multilayer, moonie and bimorph.

**Fig.7 3-D positioning multilayer actuator. Notice that the x- and y-stacks are using shear mode with the spontaneous polarization perpendicular to the applied electric field direction.**

**Fig.8 Classification of piezoelectric/electrostrictive actuators.**

**Fig.9 Transient vibration of a bimorph excited after a pseudo-step voltage applied.  $n$  is a time scale with a unit of half of the resonance period, i. e.  $2n$ =resonance period.**

**Fig.10 Dot-matrix printer head using a flight actuator mechanism.**

**Table I Difference in the ceramic actuator developments among USA, Japan and Europe.**

**Fig.11 "Hubble" telescope using three PMN electrostrictive actuators for optical image correction.**

**Fig.12 Bearingless rotor flexbeam with attached piezoelectric strips. Slight change of the blade angle provides drastic enhancement of controllability.**

**Fig.13 Structure of a printer head (a), and a differential-type piezoelectric printer-head element (b). A sophisticated monolithic hinge lever mechanism amplifies the actuator displacement by 30 times.**

**Fig.14 Camera shutter mechanism using a piezoelectric bimorph actuator.**

**Fig.15 Piezo-ceramic cylinder vibratory gyroscope for detecting rotary acceleration.**

**Fig.16 Ultrasonic linear motor of a vibratory coupler type. Choosing slightly different size legs, 90 degree phase lag of the vibration can be obtained by tuning the drive frequency, which corresponds to "trotting" mode.**



**Fig.17** Design of the surface wave type motor (a), and its electrode configuration (b) by Shinsei Industries. Most of the ultrasonic motor researches are tracing this design.

**Fig.18** Walking piezo motor using an inchworm mechanism with 4 multilayer piezoelectric actuators by Philips.

**Fig.19** Ultrasonic micro-motor on a silicon diaphragm.

## **Article Title List**

ferroelectric devices  
ferroelectric materials  
photovoltaic effects  
piezoelectric actuators  
piezoelectric devices  
piezoelectric materials  
piezoelectric motors  
piezoelectric transducers  
piezoelectricity  
Schottky effect

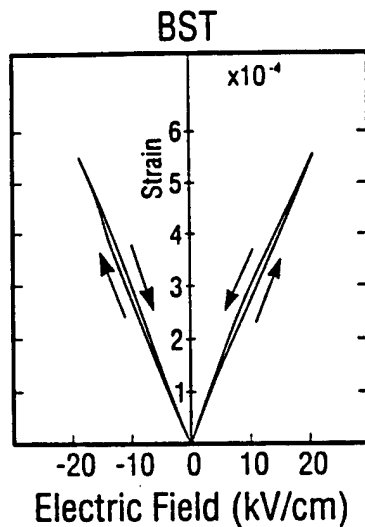
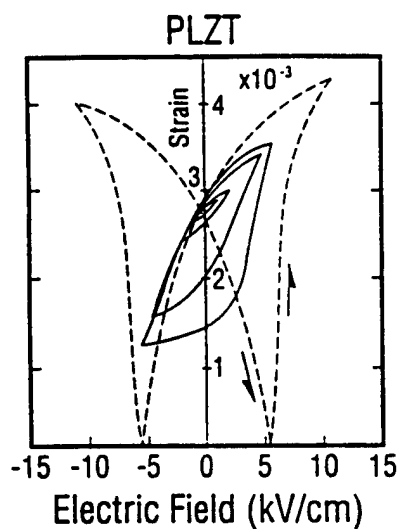
## **Keyword List**

piezoelectric actuators  
ultrasonic motors  
piezoelectric materials  
electrostrictive materials  
phase change materials  
photostriction  
monomorphs  
bimorphs  
multilayer actuators

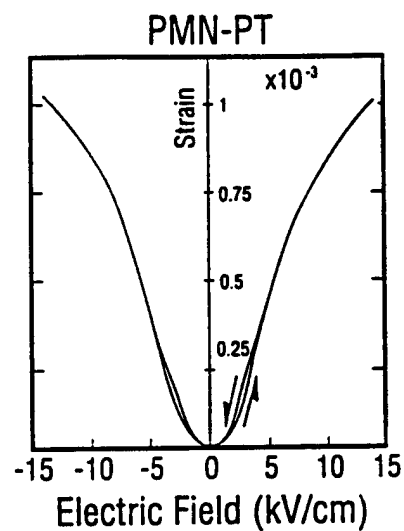
	US	Japan	Europe
TARGET	Military-oriented product	Mass-consumer product	Lab-equipment product
CATEGORY	Vibration suppressor	Mini-motor Positioner	Mini-motor Positioner Vibration suppressor
APPLICATION FIELD	Space structure Military vehicle	Office equipment Camera Precision machine Automobile	Lab stage/stepper Airplane Automobile Hydraulic system
ACTUATOR SIZE	Up-sizing (30cm)	Down-sizing (1cm)	Intermediate size (10cm)
MAJOR MANUFACTURER	AVX/Kyocera Morgan Matroc Itek Opt. Systems Burleigh AlliedSignal	Tokin Corp. NEC Hitachi Metal Mitsui-Sekka Canon Seiko Instruments	Philips Siemens Hoechst CeramTec Ferropem Physik Instrumente

Table I

a) Piezoelectric



b) Electrostrictor



c) Phase-Change Material

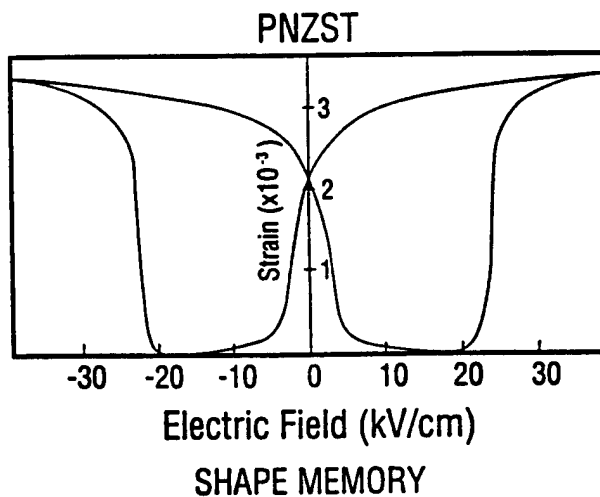
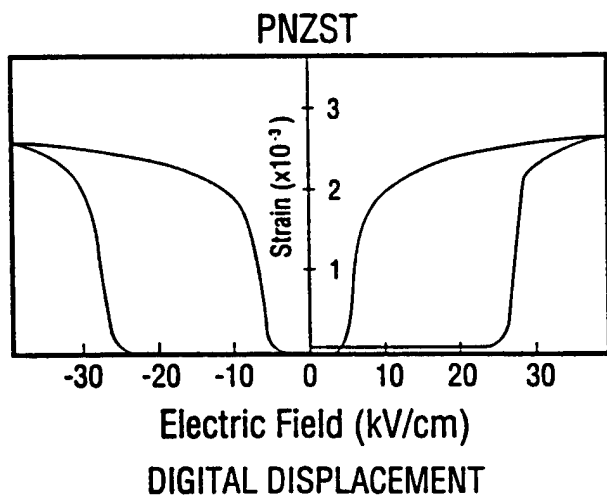


Fig. 1

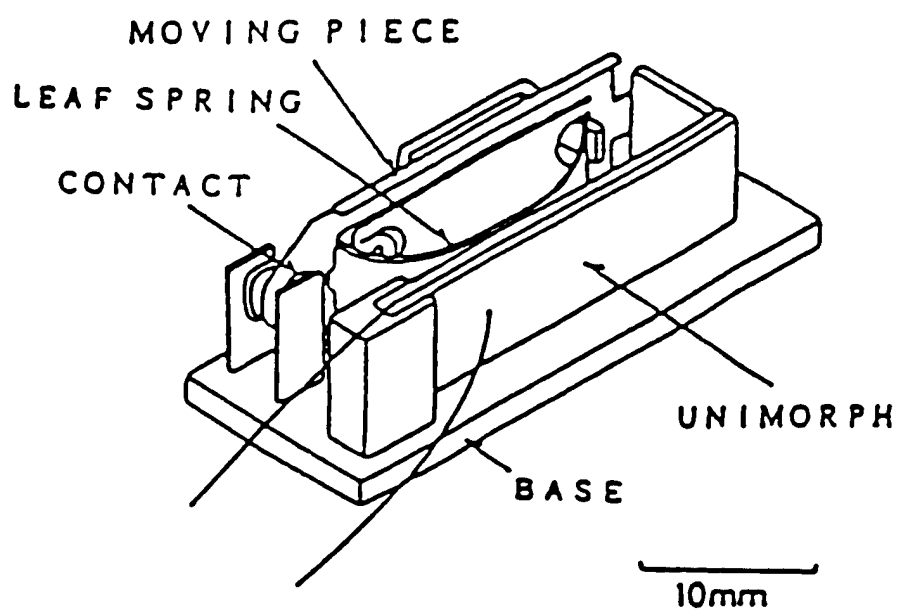
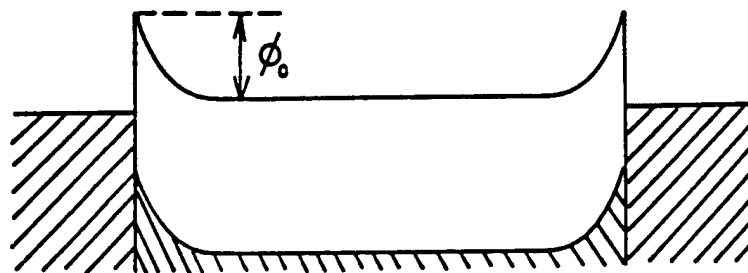


Fig. 2

(a)

Metal      Monomorph      Metal



(b)

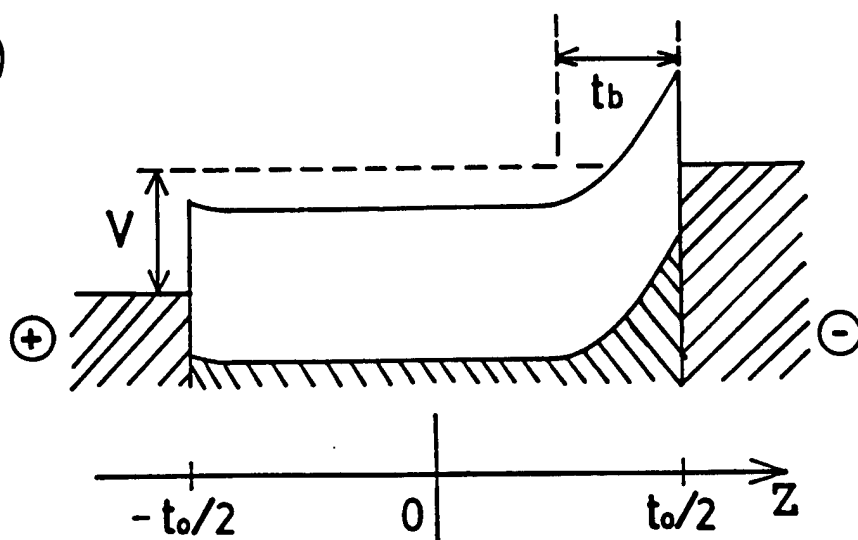


Fig. 3

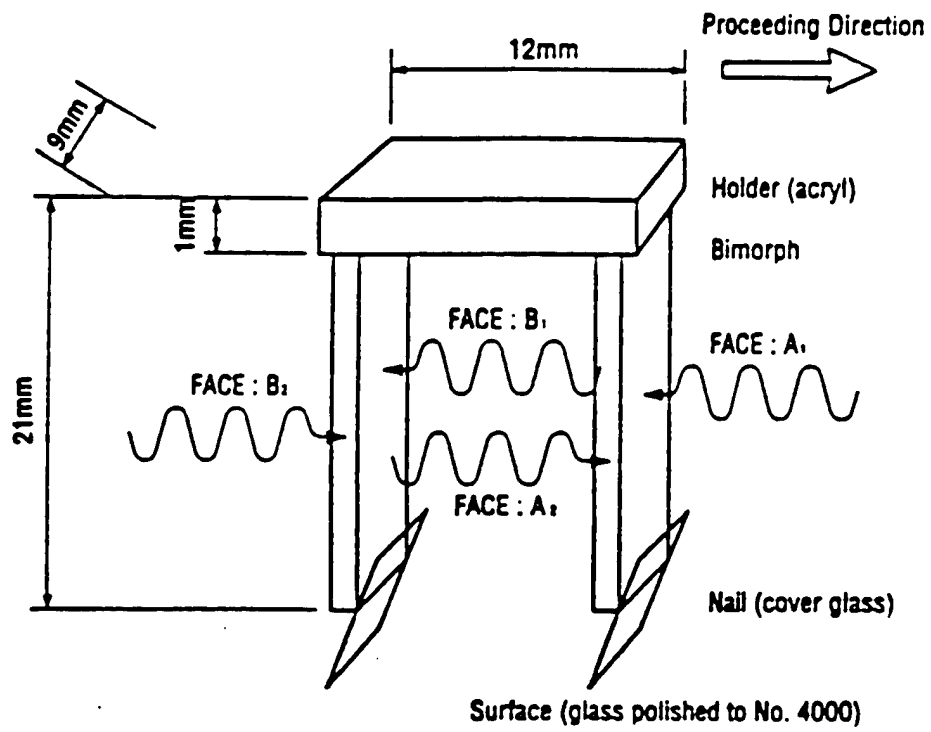


Fig. 4

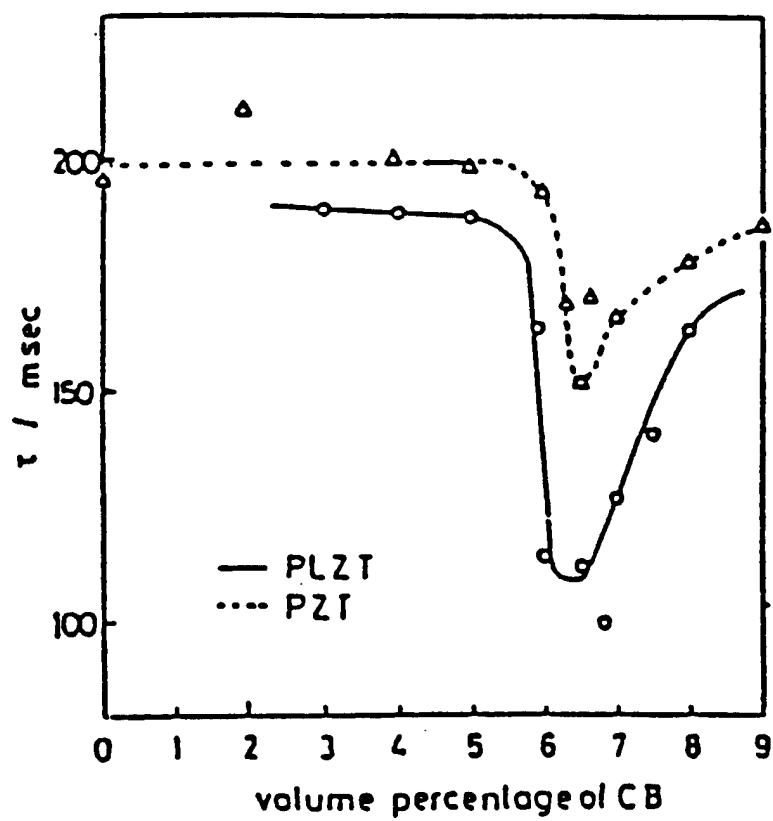


Fig. 5



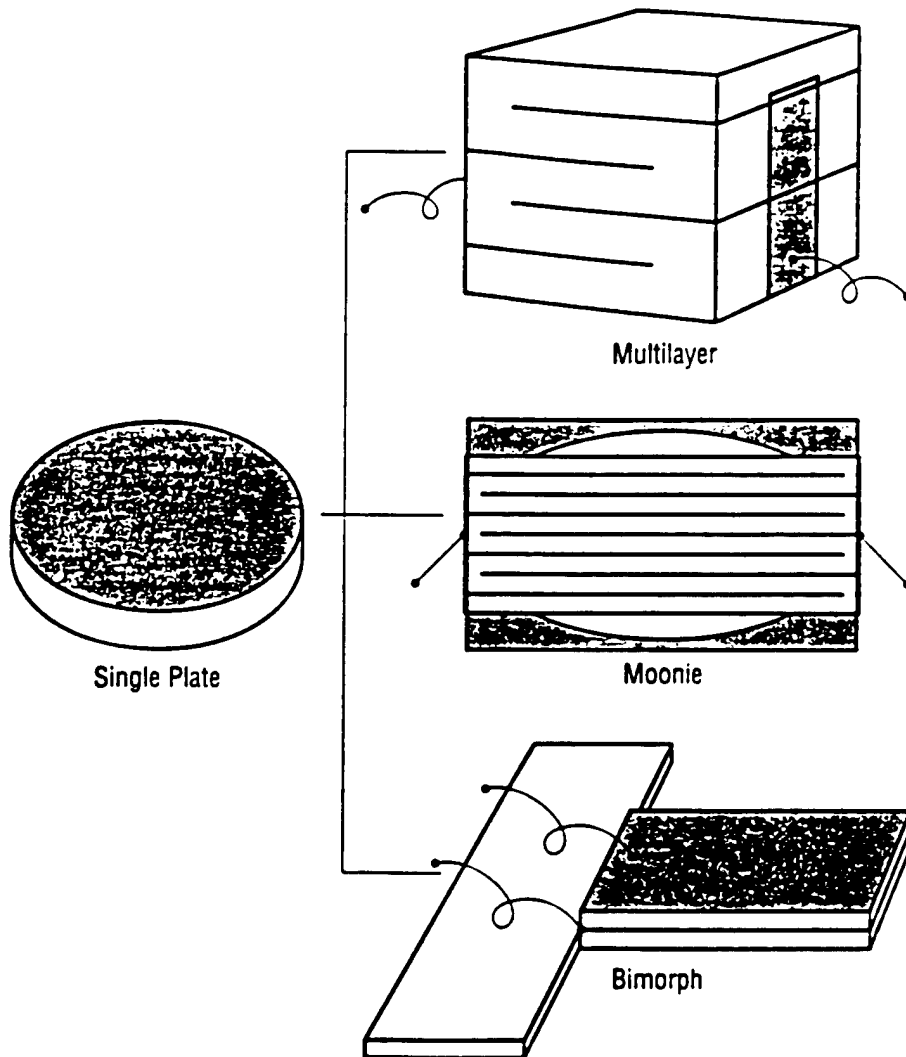


Fig. 6

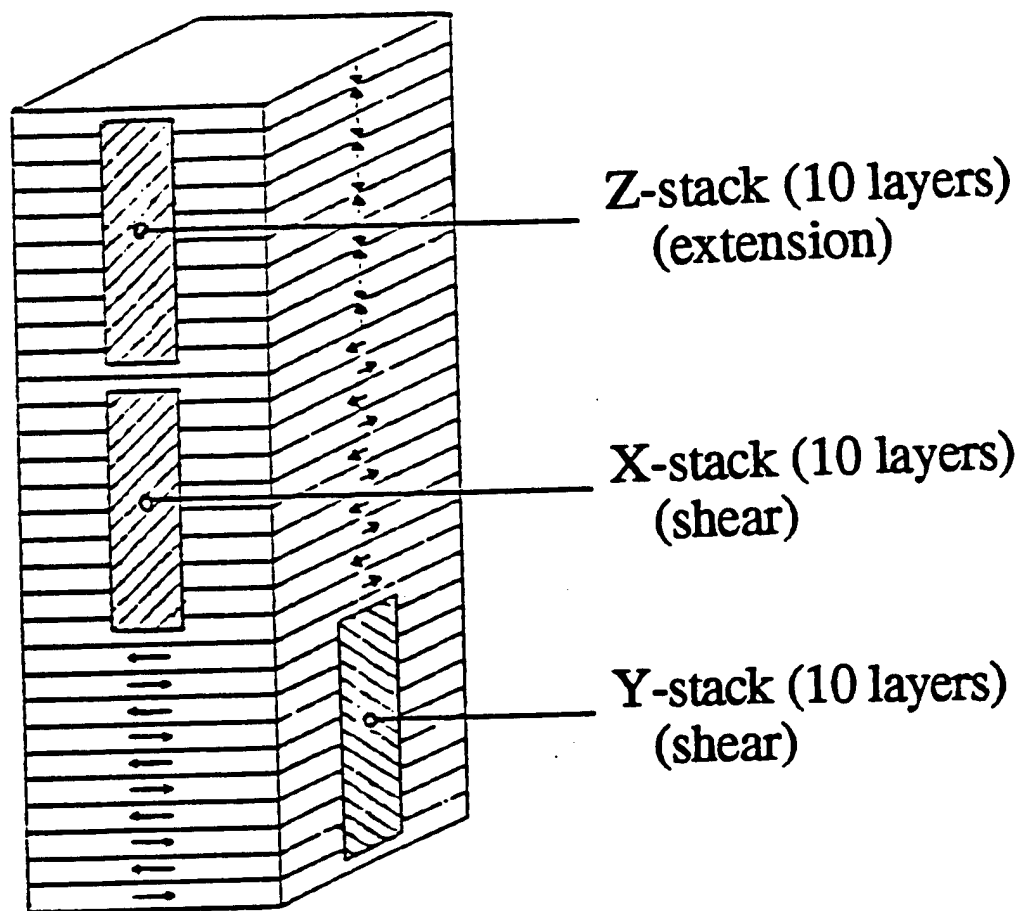


Fig. 7

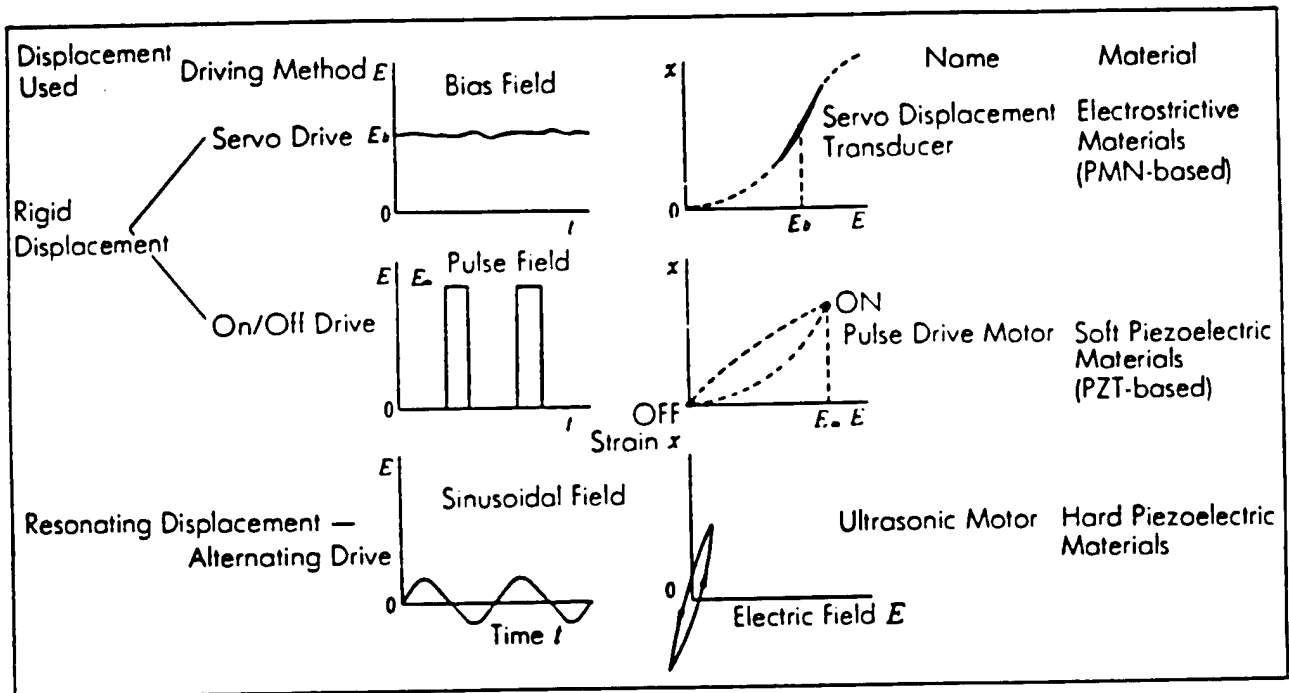


Fig. 8

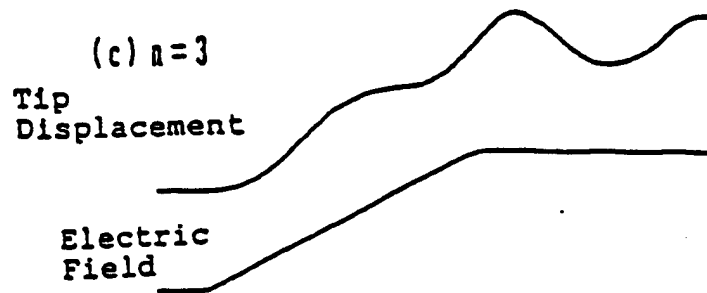
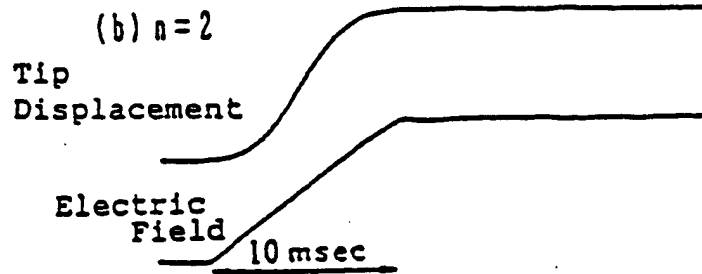
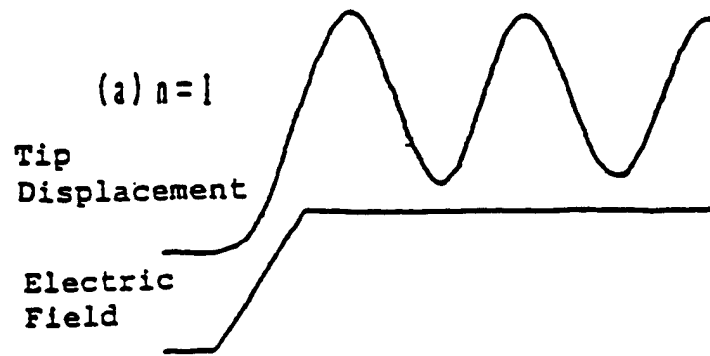


Fig. 9

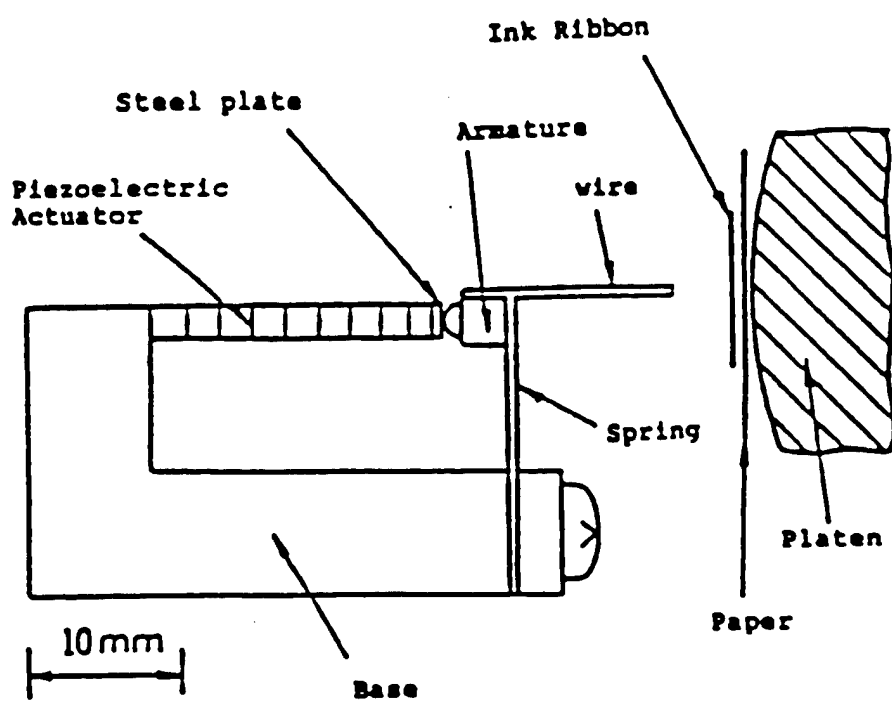


Fig. 10

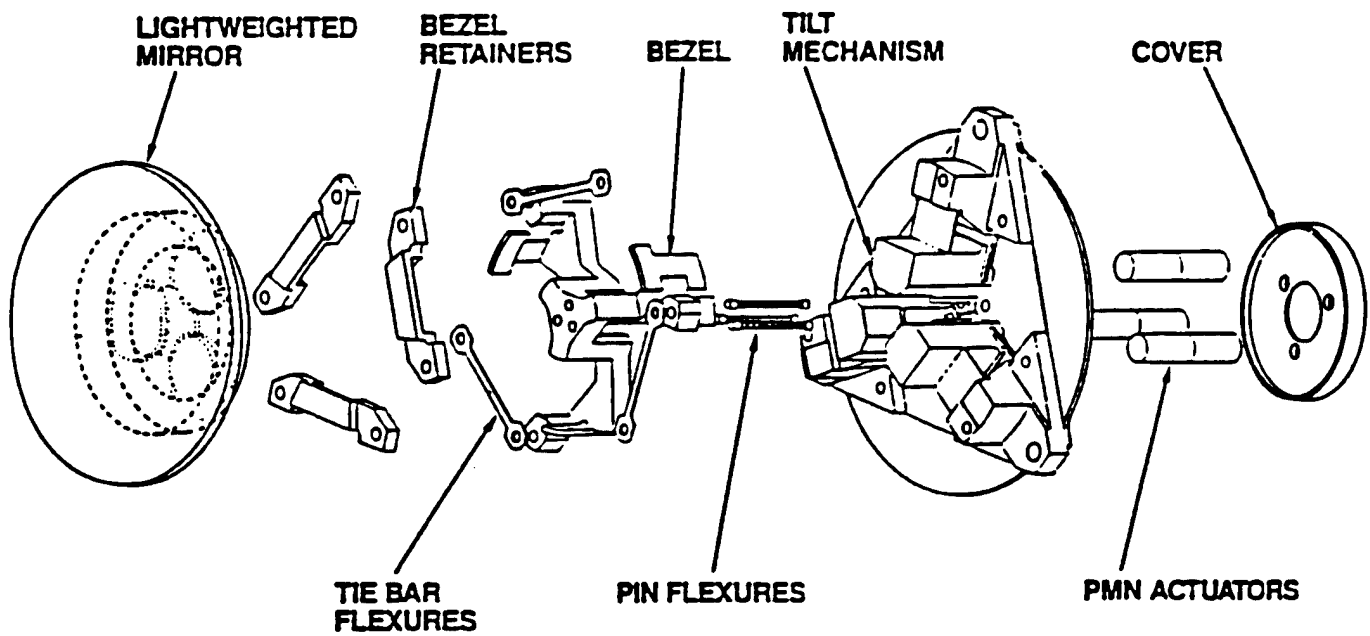


Fig. 11

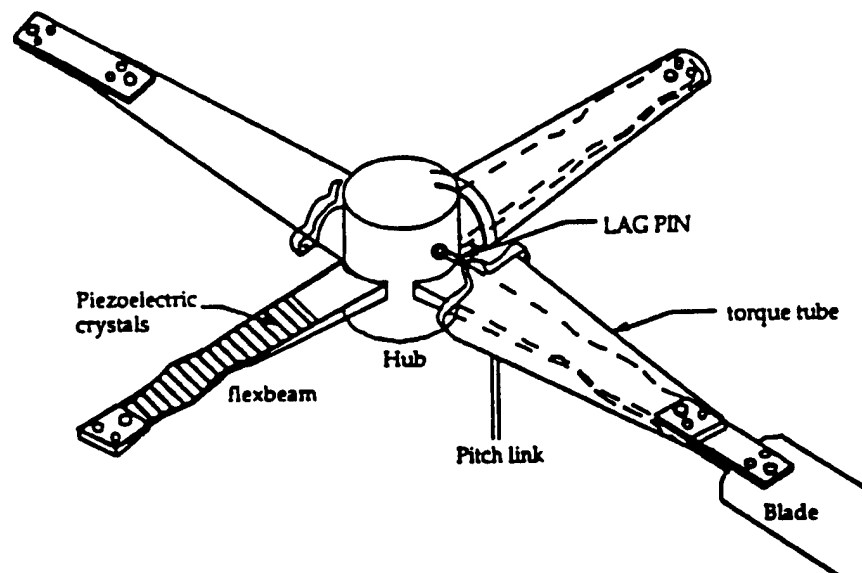


Fig. 12

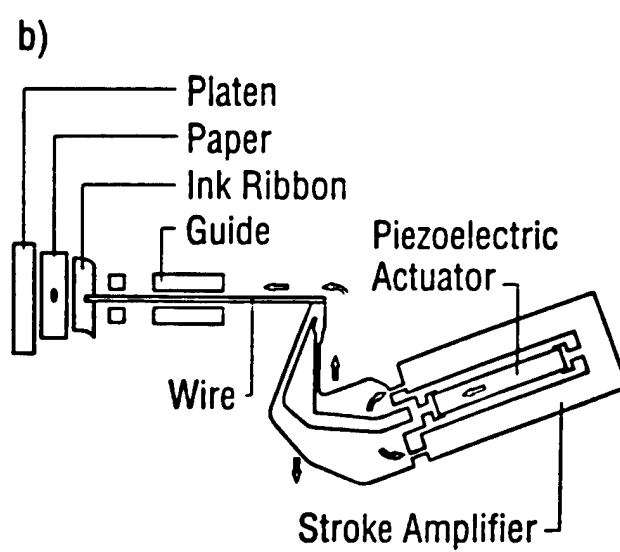
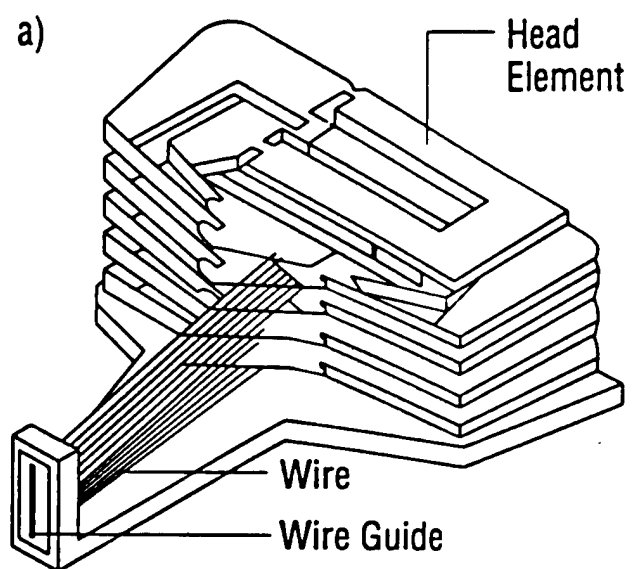


Fig. 13



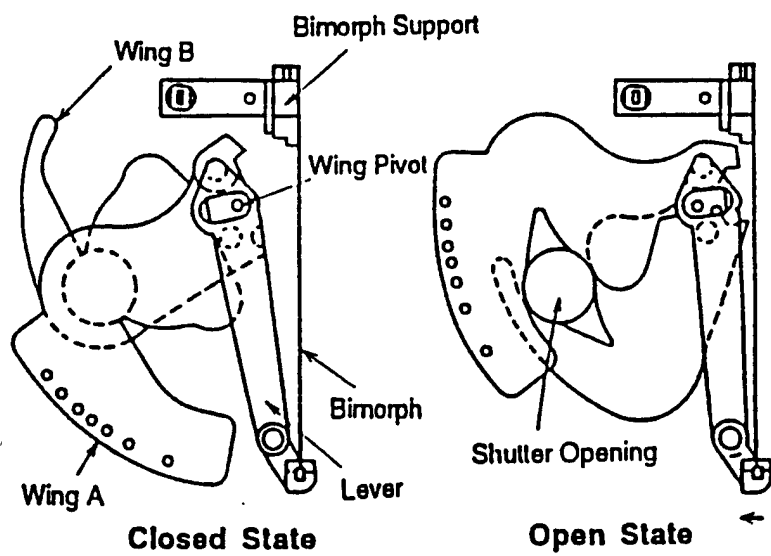


Fig. 14

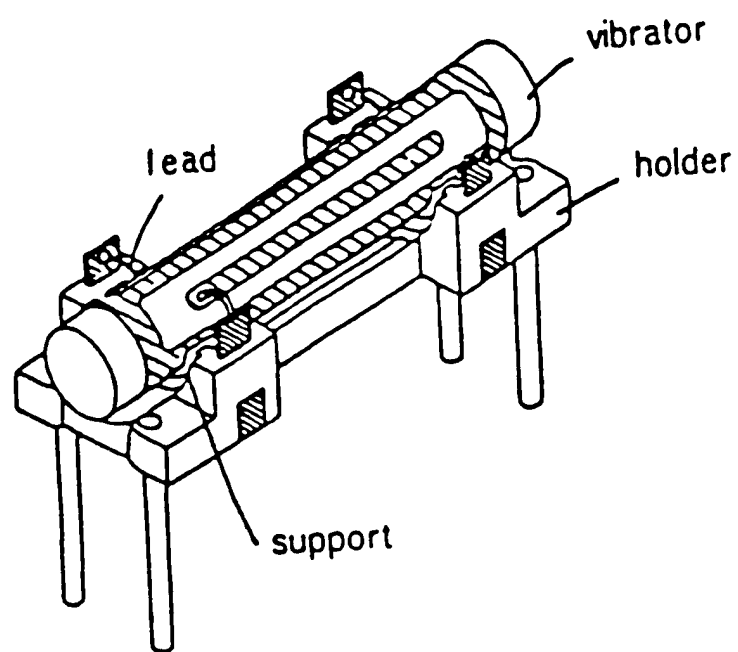


Fig. 15

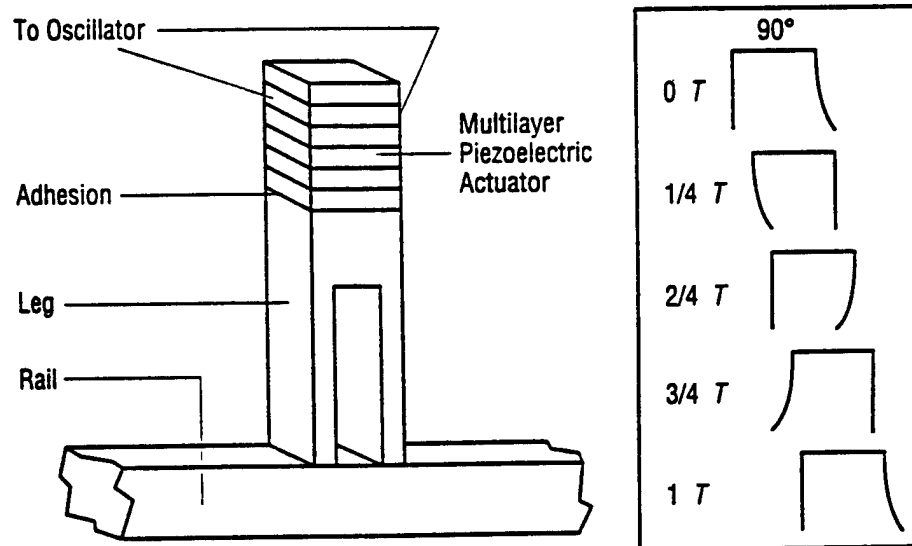


Fig. 16

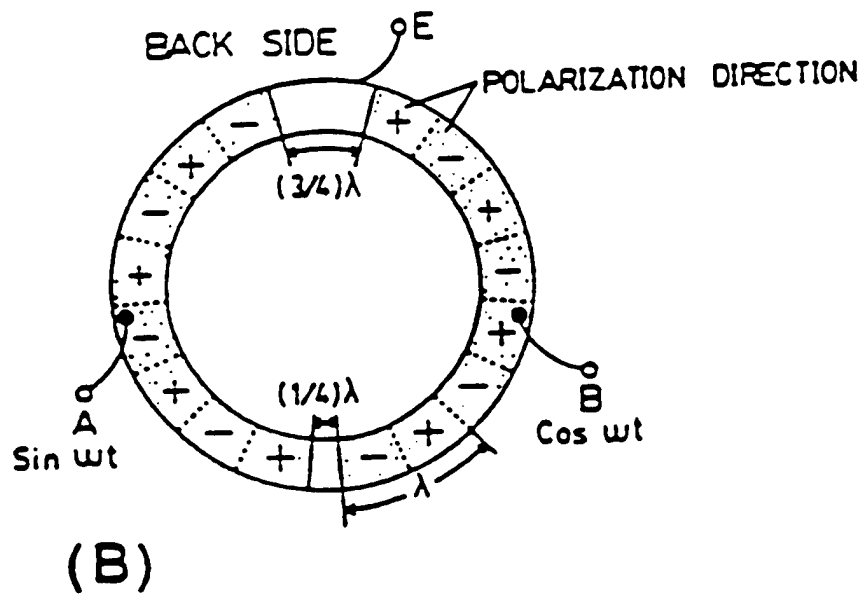
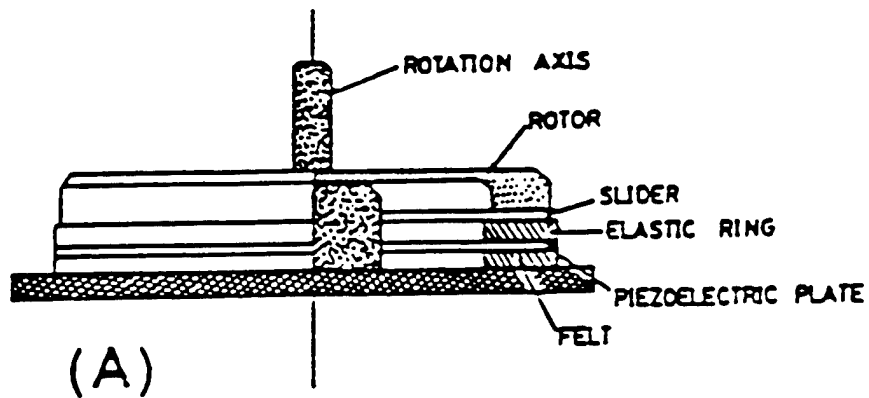


Fig. 17

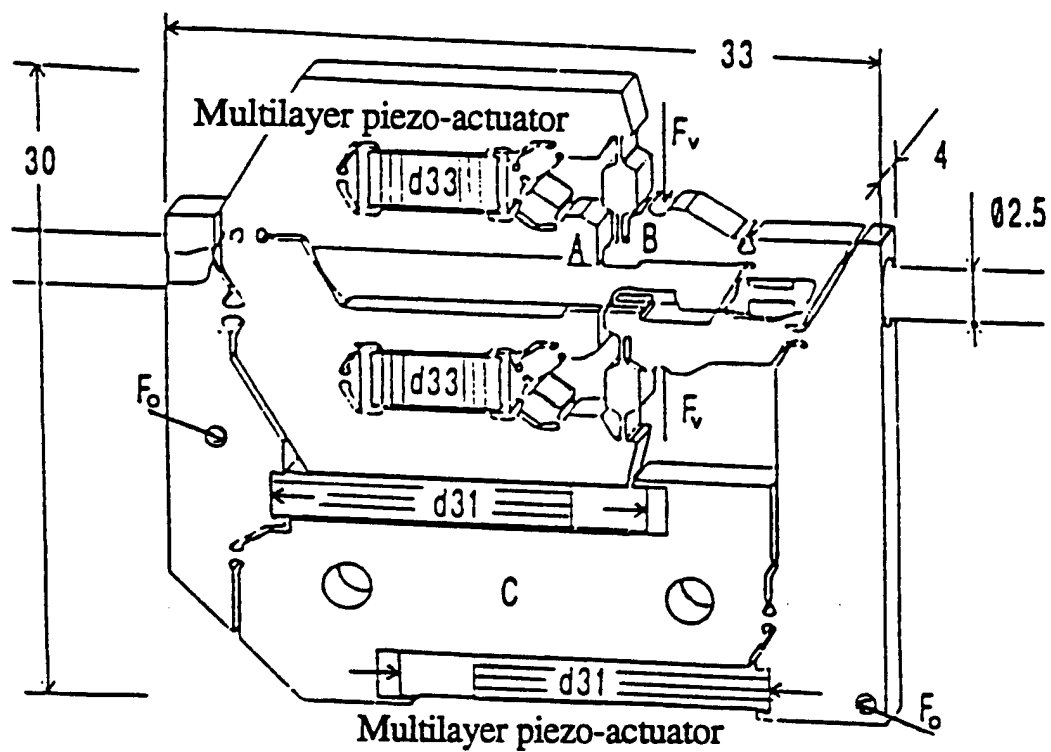


Fig. 18

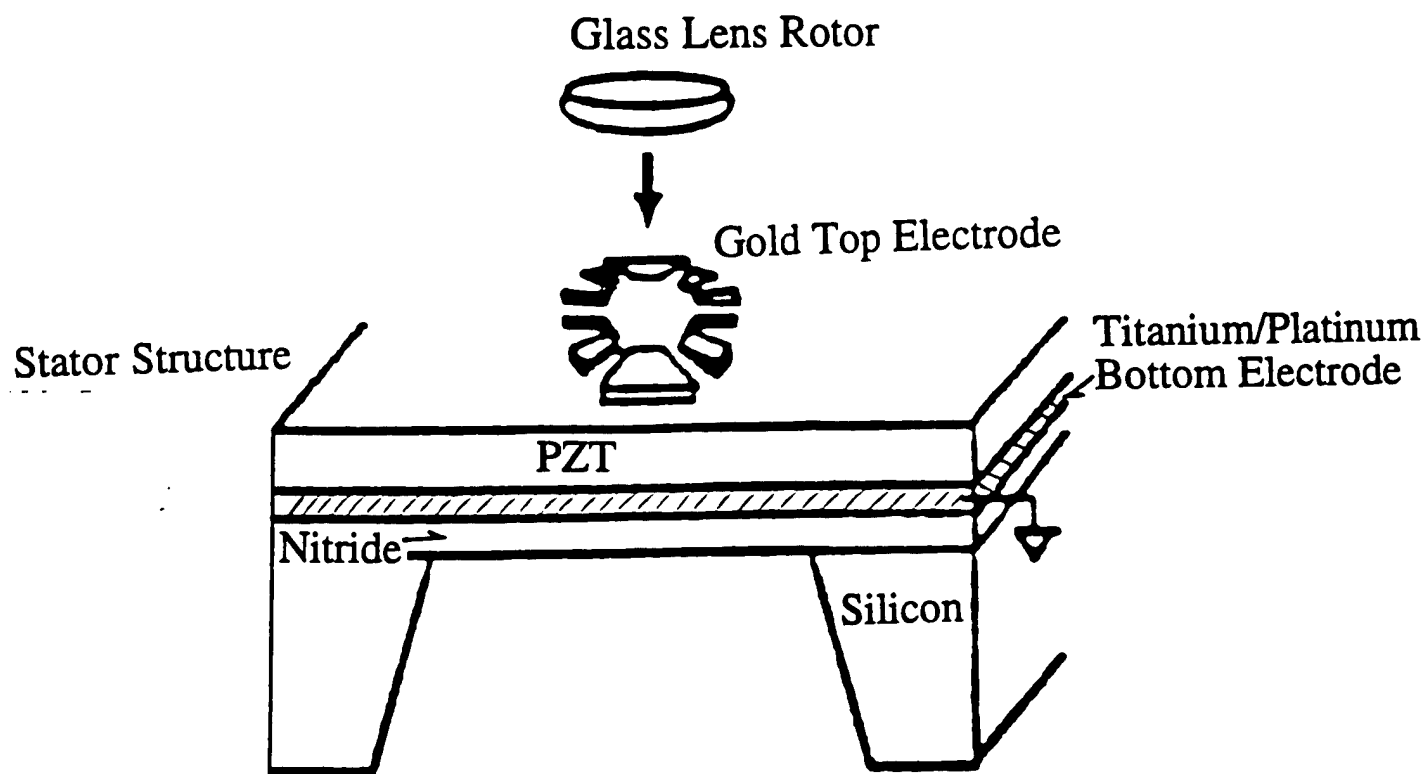


Fig. 19

# **APPENDIX 57**

**OVERVIEW: MATERIALS ISSUES IN DESIGN AND PERFORMANCE  
OF PIEZOELECTRIC ACTUATORS**

**Kenji Uchino**

**International Center for Actuators and Transducers, Materials Research Laboratory  
The Pennsylvania State University, University Park, PA 16802, Phone: 814-863-8035**

**Abstract**

Performance of ceramic actuators is dependent on complexed factors, which are divided into three major categories: properties of the ceramic itself, coupled issues with the device design and drive technique. This paper reviews important issues from these viewpoints. Investigation on the compositional change of the actuator ceramics and the doping effect is a primary issue to enhance the induced strains and to stabilize temperature and external stress dependence. The device design affects considerably its durability and life time. Failure detection or health monitoring methods of ceramic actuators will increase the reliability against their users remarkably. Regarding drive techniques of the ceramic actuators, pulse drive and ac drive require special attention; the vibration overshoot after applying a sharp-rise step/pulse voltage onto the actuator causes a large tensile force and a long-term application of ac voltage generates considerable heat.



## I. INTRODUCTION

The application area of ceramic actuators has become remarkably wide [1,2]. New actuator materials such as phase change materials, reduced piezoelectric monomorphs and photostrictors have also been proposed, which seem to be very promising. There still remain, however, problems in reliability that need to be addressed before these devices can become general-purpose commercialized products. Performance of ceramic actuators is dependent on complexed factors, which are divided into three major categories: properties of the ceramic itself, coupled issues with the device design and drive technique. This paper reviews important issues from these viewpoints.

## II. MATERIALS IMPROVEMENTS

The reproducibility of the strain characteristics depends strongly on grain size, porosity and impurity content. Increasing the grain size enhances the magnitude of the field-induced strain, but degrades the fracture toughness and increases the hysteresis [3]. The grain size should be optimized for each application. Hence, fine powders made from wet chemical processes such as coprecipitation and sol-gel will be required.

Porosity does not affect the strain behavior significantly. Figure 1 shows the tip deflection of a unimorph made from  $\text{Pb}(\text{Mg}_{1/3}\text{Nb}_{2/3})\text{O}_3$  based material plotted as a function of sample porosity [4]. The deflection did not show a difference below 8 % of porosity.

The impurity, donor- or acceptor-type, provides remarkable changes in strain. Figure 2 shows dopant effect on the field induced strain in  $(\text{Pb}_{0.73}\text{Ba}_{0.27})(\text{Zr}_{0.75}\text{Ti}_{0.25})\text{O}_3$  [5]. Since donor doping provides "soft" characteristics, the sample exhibits larger strains and less hysteresis when driven under a high electric field (1 kV/mm). On the contrary, the

acceptor doping provides "hard" characteristics, leading to a very small hysteretic loss and a large mechanical quality factor when driven under a small AC electric field (i. e. ultrasonic motor applications!).

Figure 3 shows the temperature rise versus vibration velocity for undoped, Nb-doped and Fe-doped  $\text{Pb}(\text{Zr},\text{Ti})\text{O}_3$  samples. The suppression of heat generation is remarkable in the Fe-doped (acceptor-doped) ceramic [6].

The temperature dependence of the strain characteristics must be stabilized using either composite or solid solution techniques [7]. The recent new trends are found in developing high temperature actuators for engine surroundings and cryogenic actuators for laboratory equipment and space structures.

Ceramic actuators are recommended to be used under bias compressive stress, because the ceramic is, in general, relatively weak for externally applied tensile stress. Figure 4 shows compressive uniaxial stress dependence of the weak-field piezoelectric constants  $d$  in various PZT. Note the significant enhancement in the  $d$  values for hard piezoelectric ceramics [8]. Systematic studies on stress dependence of induced strains are eagerly awaited, including the composition dependence of mechanical strength.

Although the aging effect is very important, not many investigations have been done so far. The aging effect arises from two factors: depoling and destruction. Creep and zero-point drift of the displacement are caused by the depoling of the ceramic. Another serious degradation of the strain is produced by a very high electric field under an elevated temperature, humidity and mechanical stress. Change in lifetime of a multilayer piezoelectric actuator with temperature and DC bias voltage has been reported by Nagata [9]. The lifetime under DC bias voltage obeys an empirical rule:

$$t_{\text{DC}} = A E^{-n} \exp(W_{\text{DC}} / kT), \quad (1)$$

where  $W_{\text{DC}}$  is an activation energy ranging from 0.99 - 1.04 eV.

### III. NOVEL CERAMIC ACTUATOR MATERIALS

Novel functions of materials are sometimes realized by superimposing two different effects. Newly discovered materials, shape memory ceramics, monomorphs and photostrictors, are using sophisticatedly coupled effects of piezoelectricity with another different phenomenon. The shape memory function arises from a phase transition, while the monomorph and the photostriction are associated with a semiconductor contact effect and a bulk photovoltaic effect, respectively. These "very smart" multifunctional actuator materials will be utilized for future promising devices.

#### SHAPE MEMORY CERAMICS

Concerning the phase-change-related strains, polarization induction by switching from a macroscopically nonpolar into a polar state, as in switching from an antiferroelectric to a ferroelectric state, has been proposed. Different from a shape memory alloy, the strain control is made electrically in the antiferroelectric ceramic, leading to much faster response and lower drive power than in the alloy. After the first report by Berlincourt et al. [10], lead zirconate based ceramics were investigated intensively on the field induced strain characteristics, and a shape memory effect was discovered [11,12].

Figure 5 shows the field-induced strain curves taken for the lead zirconate stannate-based system  $[\text{Pb}_{0.99}\text{Nb}_{0.02}((\text{Zr}_x\text{Sn}_{1-x})_{1-y}\text{Ti}_y)\text{O}_3]$ . The longitudinally induced strain reaches up to 0.4%, which is much larger than that expected in normal piezoelectrics or electrostrictors. A rectangular-shape hysteresis in Fig. 5 left, referred to as a "digital displacement transducer" because of the two on/off strain states, is interesting. Moreover, this field-induced transition exhibits a shape memory effect in appropriate compositions (Fig. 5 right). Once the ferroelectric phase has been induced, the material will "memorize" its ferroelectric state even under a zero-field condition, although it can be erased with the

application of a small reverse bias field. Recent researches by other groups were focused on sample fabrication processes and composition search for obtaining larger induced strains [13,14].

This shape memory ceramic was used in energy saving actuators. A latching relay in Fig. 6 was composed of a shape memory ceramic unimorph and a mechanical snap action switch, which was driven by a pulse voltage of 4ms [15]. Compared with the conventional electromagnetic relays, the new relay was much simple and compact in structure with almost the same response time.

## **MONOMORPH ACTUATORS**

A conventional bimorph-type actuator consists of two piezoelectric plates bonded together and electroded so that their piezoelectric expansion/contraction directions are opposing one another. This actuator will execute a large bending motion of several 100 $\mu$ m with the application of an electric field. The most serious problem associated with this type of actuator concerns the bonding of the ceramic plates and the elastic shim. Poor adhesion between these individual elements results in the rapid deterioration of the device after repeated use and displacement drift (creep). The monomorph actuator made from only one ceramic plate, which can achieve the bending displacement, will be a promising design in its simple construction. While avoiding the bonding problems of the bimorph structure, it also allows for significant cost reduction and production efficiency in manufacturing.

The operating principle is based on the coupling of a semiconductor contact phenomenon with the piezoelectric/electrostrictive effect [16]. When metal electrodes are applied to both surfaces of a semiconductor plate and a voltage is applied as shown in Fig. 7(a), electric field is concentrated on one side (Schottky barrier), thereby generating a non-uniform field within the plate. By making the piezoelectric slightly semiconductive in this manner, contraction along the surface occurs through the piezoelectric effect only on the

side at which the electric field is concentrated. The non-uniform field distribution generated in the ceramic causes an overall bending of the entire plate. Figure 7(b) is a modified structure, where a very thin insulative layer improves the breakdown voltage [17].

Research is underway focused on barium titanate-based and lead zirconate titanate-based piezoelectric ceramics to which additives have been doped to produce semiconductive properties. The PZT ceramics were made semiconductive by preparing solid solutions with a semiconductive perovskite compound  $(K_{1/2}Bi_{1/2})ZrO_3$ . When 300V was applied to a ceramic plate with 20 mm in length and 0.4 mm in thickness, fixed at one end, the tip deflection as much as 200  $\mu m$  could be obtained, equal in magnitude to that of bimorphs (Fig. 8) [18].

The "rainbow" actuator by Aura Ceramics [19] is a modification of the above-mentioned semiconductive piezoelectric monomorphs, where half of the piezoelectric plate is reduced so as to make a thick semiconductive electrode to cause a bend. Figure 7(c) shows the electron energy band structure of the "rainbow". The monomorph was applied to a simple speaker. Though its acoustic characteristics were not satisfactory in comparison with the conventional piezoelectric unimorph types, the monomorph speaker has advantages in mass-production and cheap cost.

## PHOTOSTRICTIVE ACTUATORS

The photostrictive effect is a phenomenon in which strain is induced in the sample when it is illuminated. This effect is focused especially in the field of micromechanism. On decreasing the size of miniaturized robots/actuators, the weight of the electric lead wire connecting the power supply becomes significant, and remote control will be definitely required for sub-millimeter devices. A photo-driven actuator is a very promising candidate for micro-robots [20].

In certain ferroelectrics, a constant electromotive force is generated with exposure of light, and a photostrictive strain results from the coupling of this bulk photovoltaic effect to inverse piezoelectricity. A bimorph unit has been made from PLZT 3/52/48 ceramic doped with slight addition of niobium or tungsten [21]. The remnant polarization of one PLZT layer is parallel to the plate and in the direction opposite to that of the other plate. Figure 9 shows the structure of a photo-driven bimorph in contrast to a voltage-driven one. Notice large illumination area, small capacitance and  $d_{33}$  usage, leading to large bending with quick response. When a violet light is irradiated to one side of the PLZT bimorph, a photovoltaic voltage of 1 kV/mm is generated, causing a bending motion. The tip displacement of 150  $\mu\text{m}$  was obtained within a couple of seconds for a 20 mm bimorph with 0.4 mm in thickness.

A photo-driven micro walking device, designed to begin moving by light illumination, has been developed [22]. As shown in Fig. 10, it is simple in structure, having neither lead wires nor electric circuitry, with two bimorph legs fixed to a plastic board. When the legs are irradiated alternately with light, the device moves like an inchworm with a speed of 100  $\mu\text{m}/\text{min}$ .

Very recently photo-mechanical resonance of a PLZT ceramic bimorph has been successfully induced using chopped near-ultraviolet irradiation, having neither electric lead wires nor electric circuits [23]. A dual beam method was used to irradiate the two sides of the bimorph alternately. The achievement of photo-induced mechanical resonance suggests the promise of photostrictors as vibration actuators such as "ultrasonic motors."

#### IV. RELIABILITY OF DEVICES

Popular silver electrodes have a serious problem of migration under a high electric field and high humidity. This problem can be overcome with usage of a silver-palladium alloy

(or more expensive Pt). To achieve inexpensive ceramic actuators, we need to introduce Cu or Ni electrodes, which requires a sintering temperature as low as 900°C. Low temperature sinterable actuator ceramics will be the next target to research.

Delamination of the electrode layer is another problem in multilayer types as well as bimorphs. To enhance adhesion, composite electrode materials with metal and ceramic powder colloid, ceramic electrodes, and electrode configurations with via holes are recommended for use [24]. To suppress the internal stress concentration which initiates the crack in the actuator device, several electrode configurations have been proposed, as shown in Fig. 11: plate-through type, slit-insert type, and float-electrode-insert type [25]. The reason why the lifetime is extended with decreasing layer thickness has not yet been clarified.

Lifetime prediction or health monitoring systems have been proposed using failure detection techniques [26]. Figure 12 shows such an "intelligent" actuator system with AE monitoring. The actuator is controlled by two feedback mechanisms: position feedback, which can compensate the position drift and the hysteresis, and breakdown detection feedback which can stop the actuator system safely without causing any serious damages to the work, e.g. in a lathe machine. Acoustic emission measurement of a piezo-actuator under a cyclic electric field is a good predictor for lifetime. AE was detected largely when a crack propagates in the ceramic actuator at the maximum speed. During a normal drive of a 100-layer piezoelectric actuator, the number of AE was counted and a drastic increase by three orders of magnitude was detected just before complete destruction. Note that part of the piezo-device can be utilized as an AE sensor.

A recent new electrode configuration with a strain gauge type (Fig. 13) is another intriguing alternative for the health monitoring [27]. By measuring the resistance of the strain gauge shaped electrode embedded in a ceramic actuator, we can monitor both electric-field induced strain and the symptom of cracks in the ceramic.

## V. DRIVE TECHNIQUES

Pulse drive of the piezoelectric / electrostrictive actuator generates very large tensile stress in the device, sometimes large enough to initiate cracks. In such cases, compressive bias stress should be employed on the device through clamping mechanisms such as a helical spring and a plate spring.

Temperature rise is occasionally observed particularly when the actuator is driven cyclically, i.e. in pulse drive or ultrasonic motor applications. Temperature rise is due to the imbalance between heat generation basically caused by dielectric hysteresis loss and the heat dissipation determined by the device size (surface area!) [28]. Figure 14 shows a linear relation between temperature rise and the  $v_e/A$  value, where  $v_e$  is the effective volume and  $A$  the surface area of a multilayer actuator, when driven at a fixed magnitude and frequency of the electric field. We need to select a suitable drive power or a driving duty ratio so as not to produce a temperature rise of more than 20°C, in particular, when used in a polymer-embedded state, which suppresses the heat dissipation drastically.

Regarding ultrasonic motors, the usage of the antiresonance mode has been proposed [29]. Quality factor  $Q$  and temperature rise have been investigated on a PZT ceramic rectangular bar, and the results for the fundamental resonance (A-type) and antiresonance (B-type) modes are illustrated in Fig. 15 as a function of vibration velocity. It is recognized that  $Q_B$  is higher than  $Q_A$  over the whole vibration velocity range. In other words, the antiresonance mode can provide the same mechanical vibration level without generating heat.

All the previous ultrasonic motors have utilized the mechanical resonance mode at the so-called "resonance" frequency. However, the mechanical resonant mode at the "antiresonance" frequency reveals higher  $Q$  and efficiency than the "resonance" state. Moreover, the usage of "antiresonance," whose admittance is very low, requires low current and high voltage for driving, in contrast to high current and low voltage for the



"resonance." This means that a conventional inexpensive power supply may be utilized for driving the ultrasonic motor.

## **VI. CONCLUSION**

There are many possibilities to improve the durability and reliability of ceramic actuators. Future wide commercialization will be rather promising. This work was partly supported by US Army Research Office and Office of Naval Research through Contracts No. DAAL 03-92-G-0244, No. N00014-91-J-4145 and N00014-96-1-1173.

## REFERENCES

- [1] K.Uchino, *Ceramic Actuators and Ultrasonic Motors*, Kluwer Academic Pub., 1997.
- [2] K.Uchino, "Ceramic Actuators: Principles and Applications," MRS Bull., vol.18, p.42, 1993.
- [3] K.Uchino and T.Takasu, "Evaluation Method of Piezoelectric Ceramics from a Viewpoint of Grain Size," Inspec., vol.10, p.29, 1986.
- [4] K.Abe, K.Uchino and S.Nomura, "The Electrostrictive Unimorph for Displacement Control," Jpn. J. Appl. Phys., vol.21, p.L408, 1982.
- [5] A.Hagimura and K.Uchino, "Impurity Doping Effect on Electrostrictive Properties of (Pb,Ba)(Zr,Ti)O<sub>3</sub>," Ferroelectrics, vol.93, p.373, 1989.
- [6] S.Takahashi and S.Hirose, Jpn. J. Appl. Phys., vol.32, Pt.1, p.2422, 1993.
- [7] K.Uchino, J.Kuwata, S.Nomura, L.E.Cross and R.E. Newnham, "Interrelation of Electrostriction with Phase Transition Diffuseness," Jpn. J. Appl. Phys., vol.20, Suppl.20-4, p.171, 1981.
- [8] Q.M.Zhang, J.Zhao, K.Uchino and J.Zheng, "Change of the Weak Field Properties of Pb(Zr,Ti)O<sub>3</sub> Piezoceramics with Compressive Uniaxial Stresses," J. Mater. Res., vol.12, p.226, 1997.
- [9] K.Nagata, "Lifetime of Multilayer Actuators," Proc. 49th Solid State Actuator Study Committee, JTTAS, Tokyo, 1995.1) K.Uchino, "Ceramic Actuators: Principles and Applications," Mater. Res. Soc. Bull. vol.18, p.42, 1993.
- [10] D.Berlincourt, H.H.A.Krueger and B.Jaffe, J. Phys. & Chem. Solids., vol.25, p.659, 1964.
- [11] K.Uchino and S.Nomura, "Electrostriction in PZT-Family Antiferroelectrics," Ferroelectrics, vol.50, p.191, 1983.
- [12] K.Y.Oh, A.Furuta and K.Uchino, "Shape Memory Unimorph Actuators Using Lead Zirconate-Based Antiferroelectrics," J. Ceram. Soc. Jpn., vol.98, p.905, 1990.

- [13] W.Y.Pan, Q.Zhang, A.Bhalla and L.E.Cross, J. Amer. Ceram. Soc., vol.72, p.571, 1989.
- [14] Z.Xu, D.Viehland and D.A.Payne, J. Appl. Phys., vol.74, p.3406, 1993.
- [15] A.Furuta, K.Y.Oh and K.Uchino, "Shape Memory Ceramics and Their Application to Latching Relays," Sensors and Mater., vol.3, p.205, 1992.
- [16] K.Uchino, M.Yoshizaki, K.Kasai, H.Yamamura, N.Sakai and H.Asakura, Jpn. J. Appl. Phys., vol.26, p.1046, 1987.
- [17] K.Uchino, M.Yoshizaki and A.Nagao, Jpn. J. Appl. Phys., vol.26, Suppl.26-2, p.201, 1987.
- [18] K.Uchino, M.Yoshizaki and A.Nagao, "Monomorph Characteristics in  $\text{Pb}(\text{Zr,Ti})\text{O}_3$  Based Ceramics," Ferroelectrics, vol.95, p.161, 1989.
- [19] F.Furman, G.Li and G.H.Haertling, "An Investigation of the Resonance Properties of Rainbow Devices," Ferroelectrics, vol.160, p.357, 1994.
- [20] K.Uchino, "Review: Photostriction and Its Applications," J. Innovations in Mater. Res., vol.1, p.11, 1995.
- [21] M.Tanimura and K.Uchino, Sensors and Mater., vol.1, p.47, 1988.
- [22] K.Uchino, "Micro Walking Machines Using Piezoelectric Actuators," J. Rob. Mech., vol.1, p.124, 1989.
- [23] S.Y.Chu, Z.Ye and K.Uchino, J. Adv. Performance Mater., vol.1, p.129, 1994.
- [24] K.Abe, K.Uchino and S.Nomura, "Barium Titanate-Based Actuator with Ceramic Internal Electrodes," Ferroelectrics, vol.68, p.215, 1986.
- [25] H.Aburatani, K.Uchino, A.Furuta and Y.Fuda, "Destruction Mechanism and Destruction Detection Technique for Multilayer Ceramic Actuators," Proc. 9th Int'l Symp. Appl. Ferroelectrics, p.750, 1995.
- [26] K.Uchino and H.Aburatani, "Destruction Detection Techniques for Safety Piezoelectric Actuator Systems," Proc. 2nd Int'l Conf. Intelligent Mater., p.1248, 1994.

- [27] K.Uchino, "Reliability of Ceramic Actuators," Proc. Int'l Symp. Appl. Ferroelectrics, 1997 (in press).
- [28] J.Zheng, S.Takahashi, S.Yoshikawa, K.Uchino and J.W.C. de Vries, "Heat Generation in Multilayer Piezoelectric Actuators," J. Amer. Ceram. Soc., vol.79, p.3193, 1996.
- [29] S.Hirose, M.Aoyagi, Y.Tomikawa, S.Takahashi and K. Uchino, "High-Power Characteristics at Anti-resonance Frequency of Piezoelectric Transducers," Proc. Ultrasonic Int'l, p.1, 1995.

## FFIGURE CAPTIONS

- Fig.1. Tip deflection of a PMN unimorph plotted as a function of the sample porosity.
- Fig.2. Dopant effect on the field induced strain in  $(\text{Pb}_{0.73}\text{Ba}_{0.27})(\text{Zr}_{0.75}\text{Ti}_{0.25})\text{O}_3$ .
- Fig.3. Temperature rise versus effective vibration velocity for PZT samples doped with Nb or Fe.
- Fig.4. Compressive uniaxial stress dependence of the weak-field piezoelectric constant  $d$  in PZT (from top to bottom, "soft" to "hard").
- Fig.5 Electric field-induced strains in phase-change materials  $\text{Pb}(\text{Zr},\text{Sn},\text{Ti})\text{O}_3$ .
- Fig.6 Latching relay using a shape memory ceramic unimorph.
- Fig.7 Energy band models for the monomorph actuator: (a) Schottky type, (b) Metal-Insulator-Semiconductor structure with very thin insulative layers, (c) MIS structure with a very thick insulative layer.
- Fig.8 Drive voltage versus tip displacement of a monomorph plate. The sample was made of  $0.7\text{Pb}(\text{Zr}_{0.9}\text{Ti}_{0.1})\text{O}_3-0.3(\text{K}_{1/2}\text{Bi}_{1/2})\text{ZrO}_3$  (20mm x 10mm x 0.4mm in size).
- Fig.9 Structures of voltage- and photo-driven bimorphs and their driving principles.
- Fig.10 Structure of the photo-driven micro walking machine and the illumination direction.
- Fig.11 Various electrode configurations for multilayer ceramic actuators.
- Fig.12 Intelligent actuator system with both position feedback and breakdown detection feedback mechanisms.
- Fig.13 Multilayer ceramic actuator with a strain-gauge type electrode.
- Fig.14 Temperature rise versus  $v_e/A$  for various size multilayer ceramic actuators (applied field: 3 kV/mm at 300Hz).
- Fig.15 Vibration velocity dependence of the quality factor and temperature rise for both A- and B-type resonances of a PZT resonator.

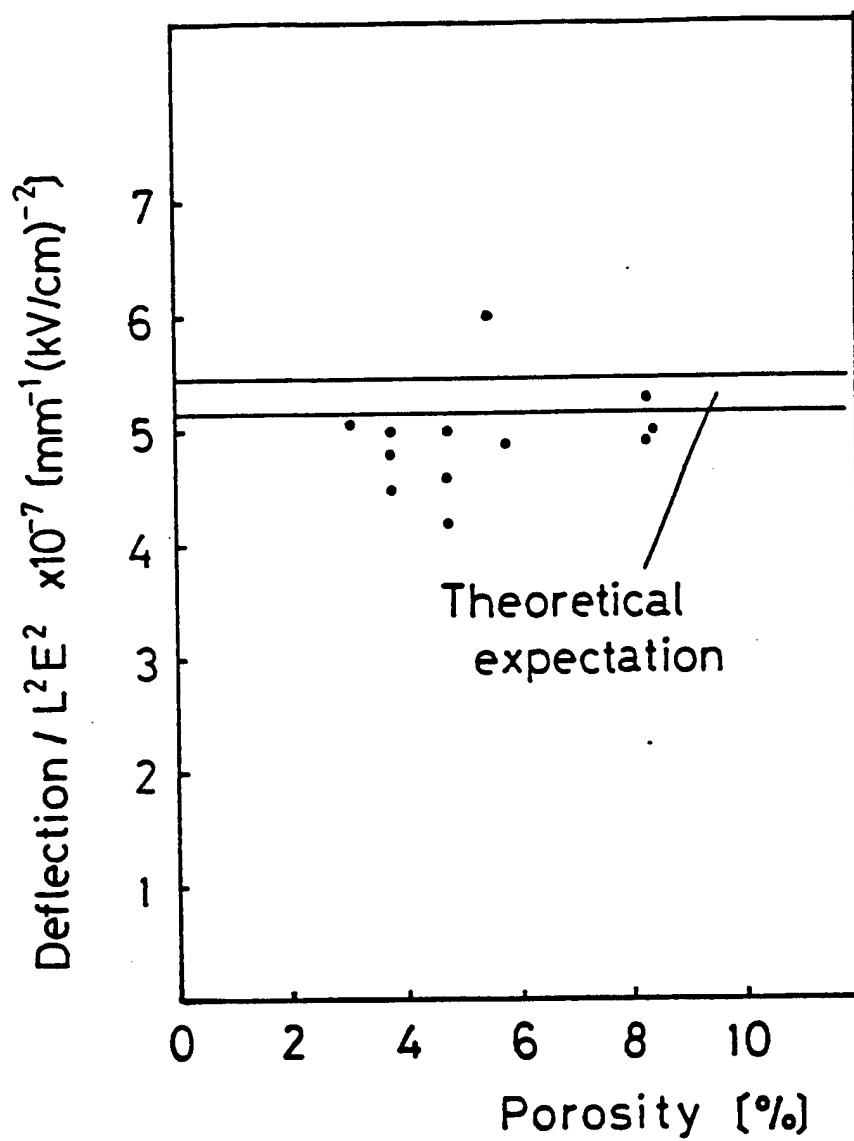


Fig 1 Uchino

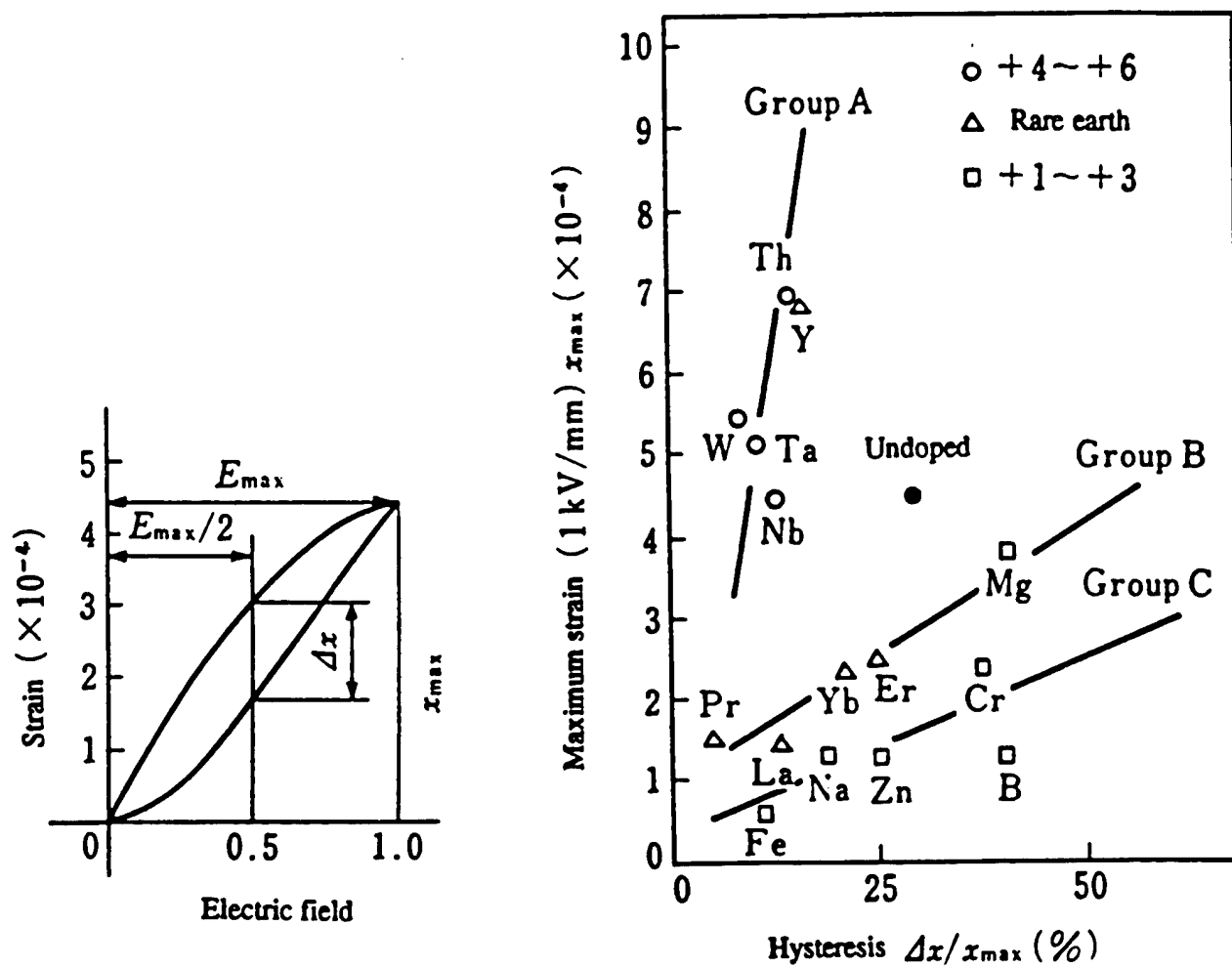


Fig 2 Uchino

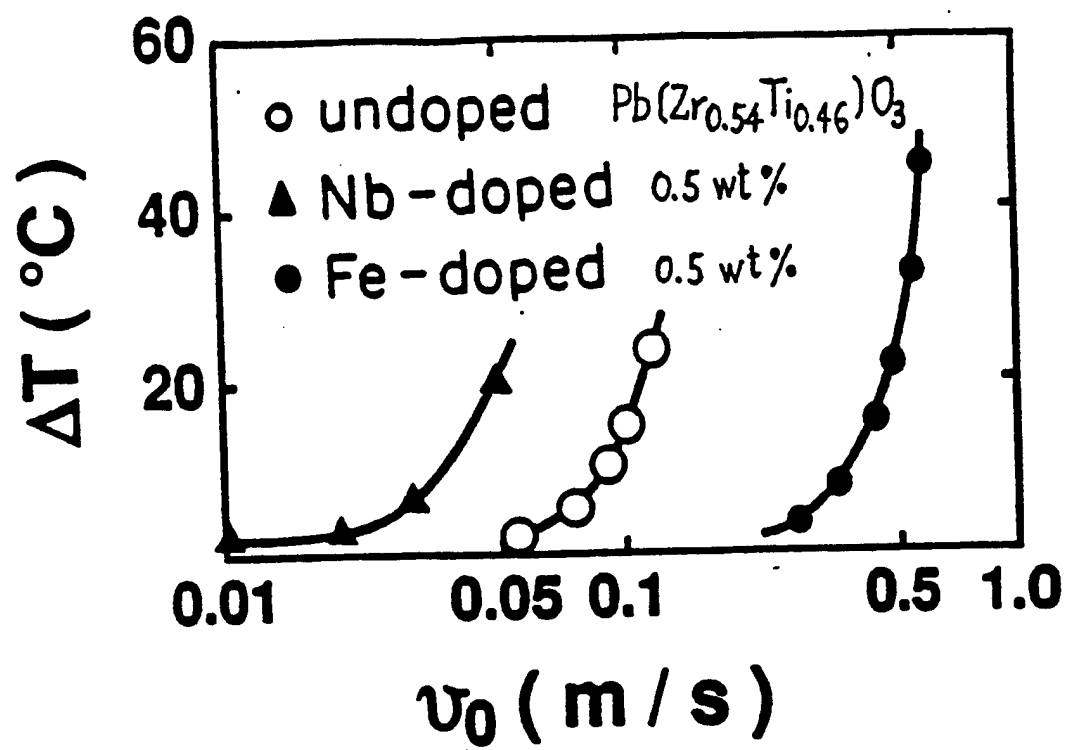


Fig 3 Uchino



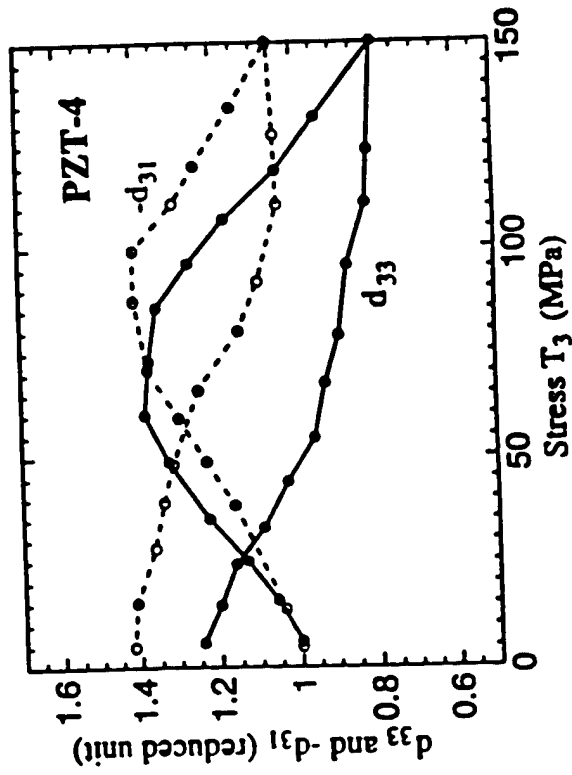
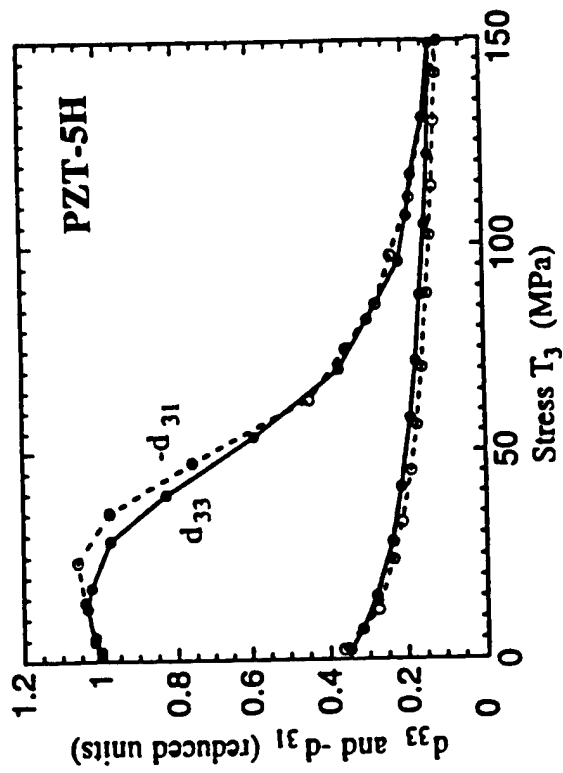
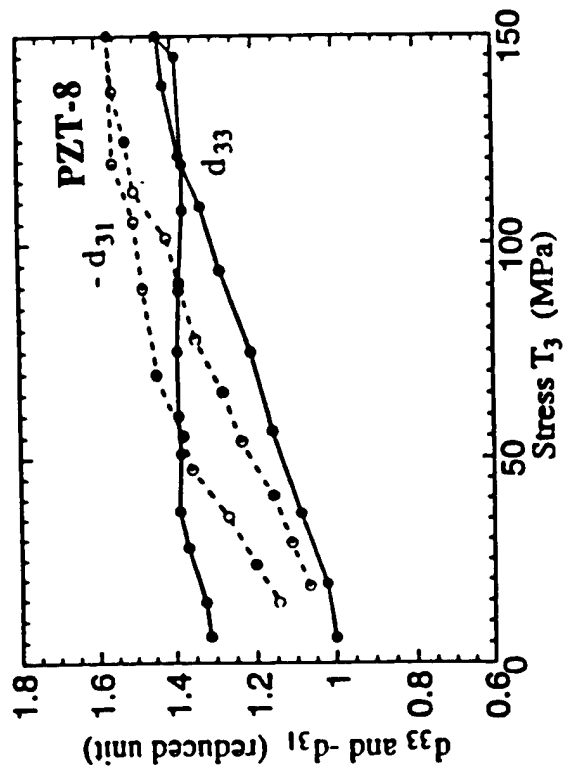
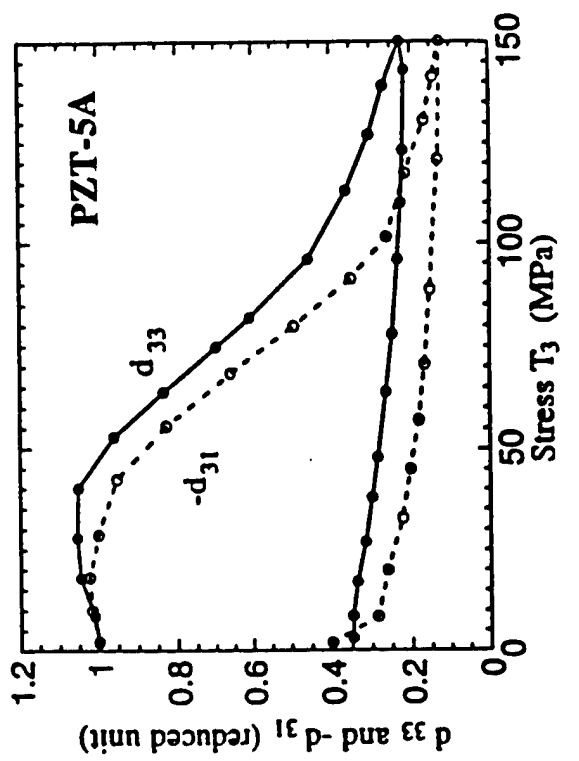


Fig 4 Uchino

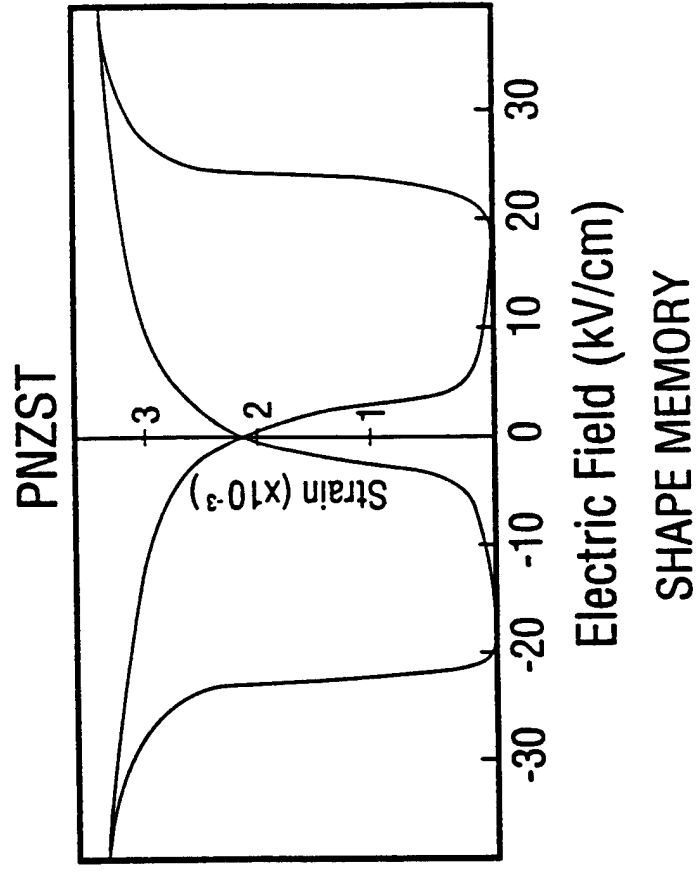
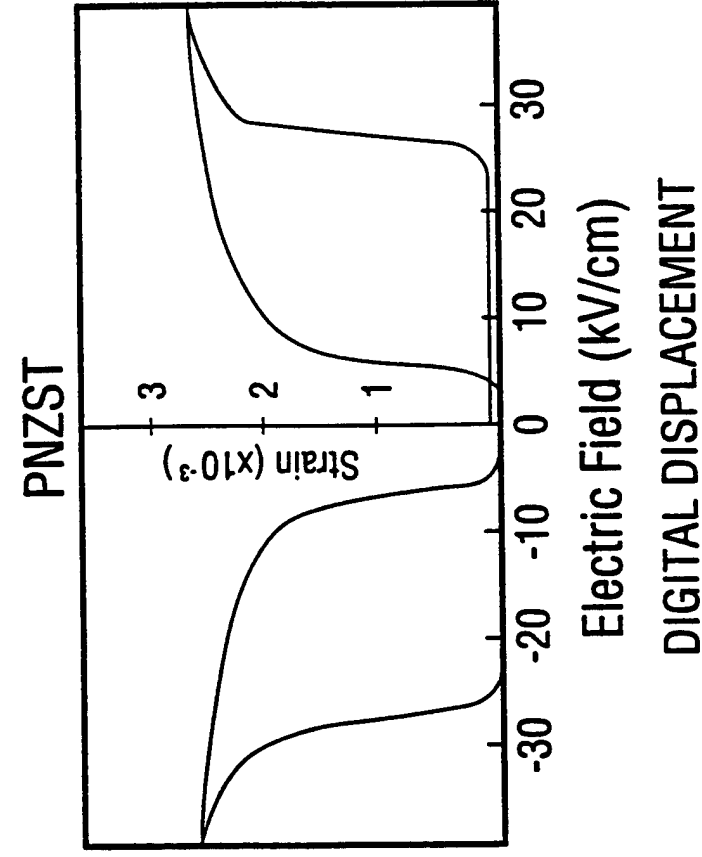


Fig 5 Uchino

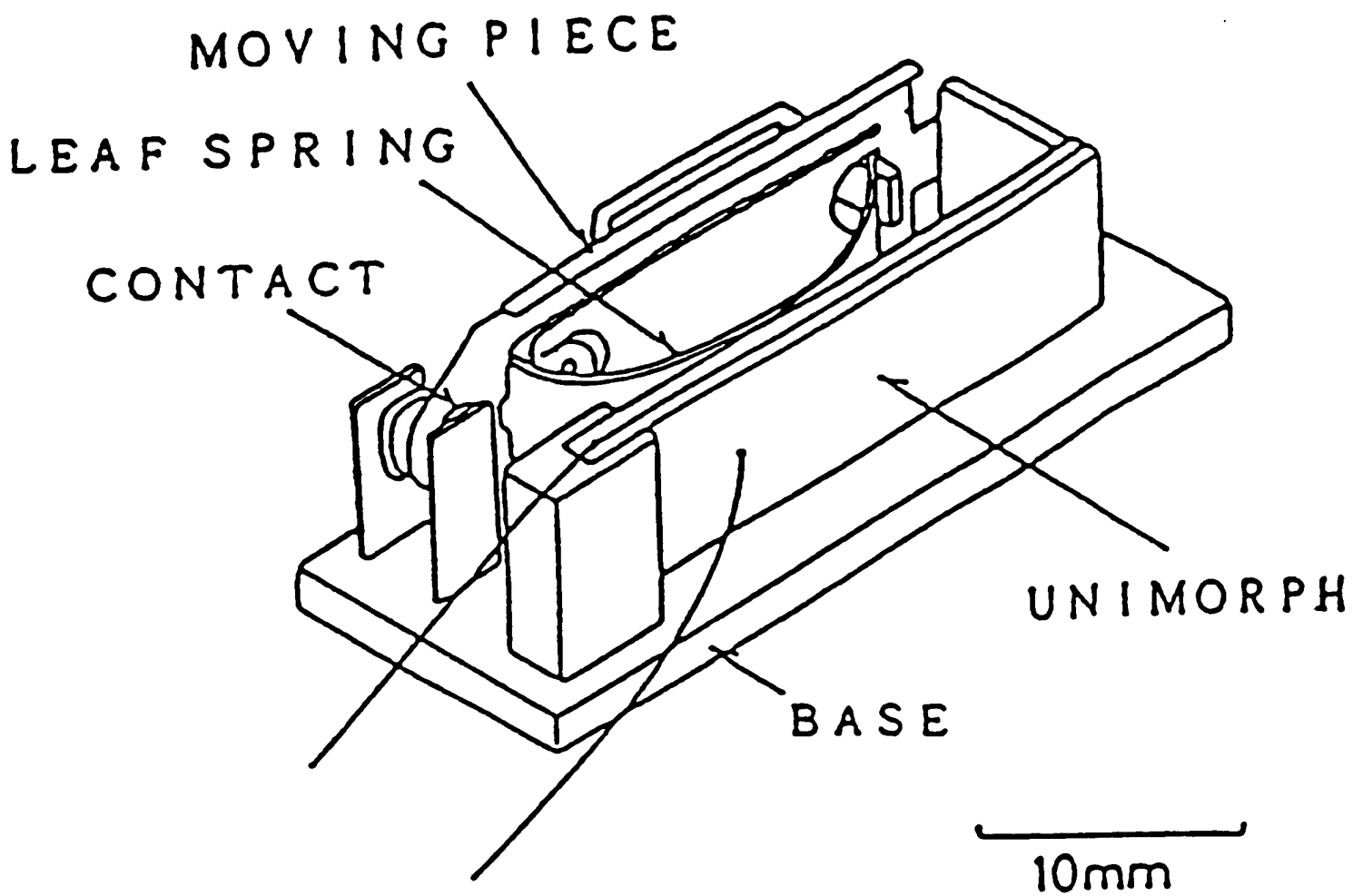
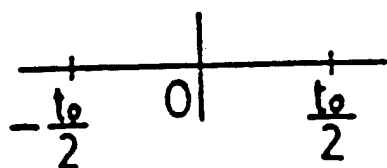
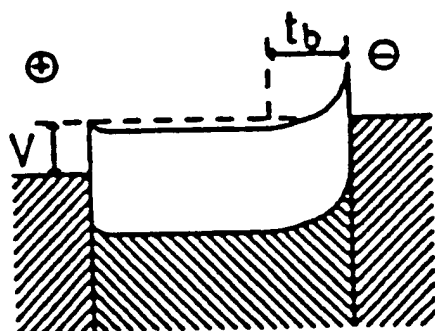
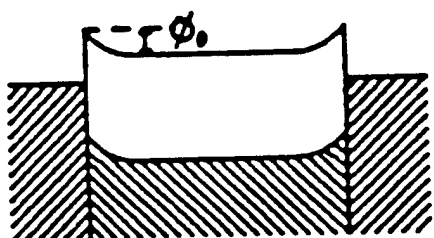
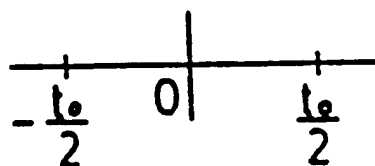
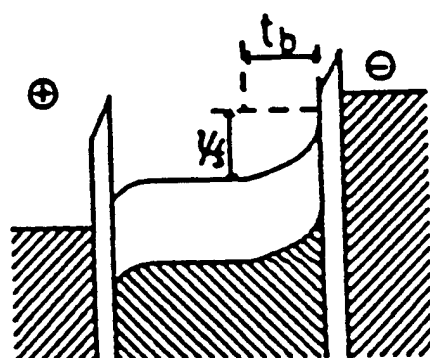
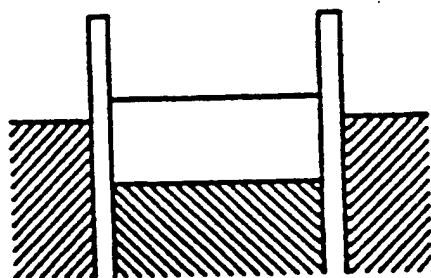


Fig 6 Uchino

(a)



(b)



(c)

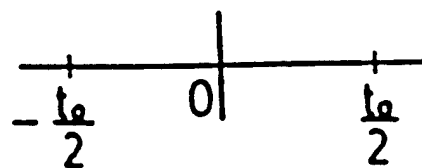
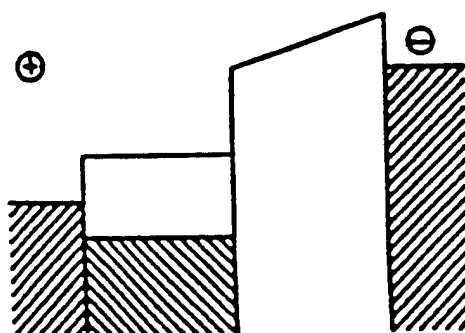
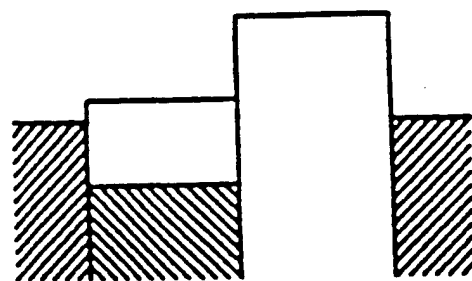


Fig 7 Uchino

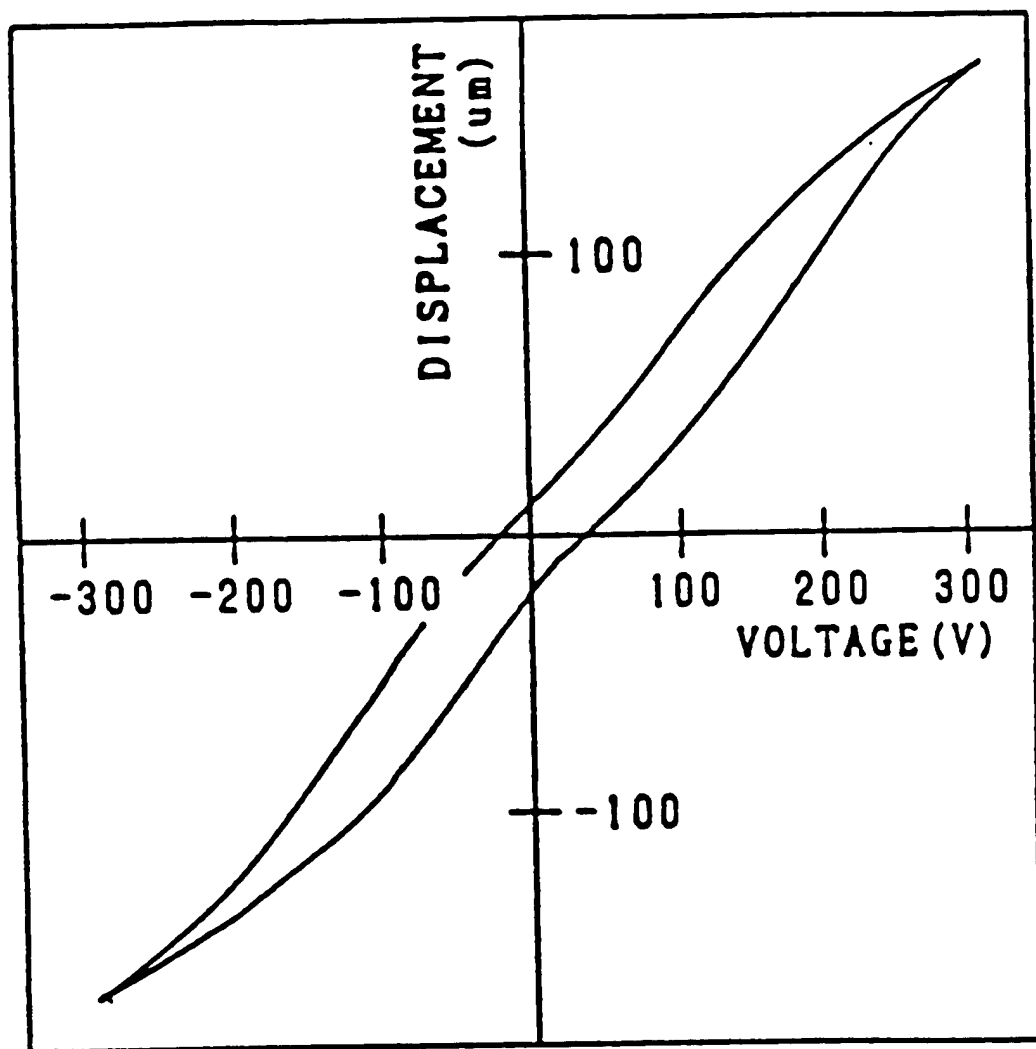


Fig 8 Uchino

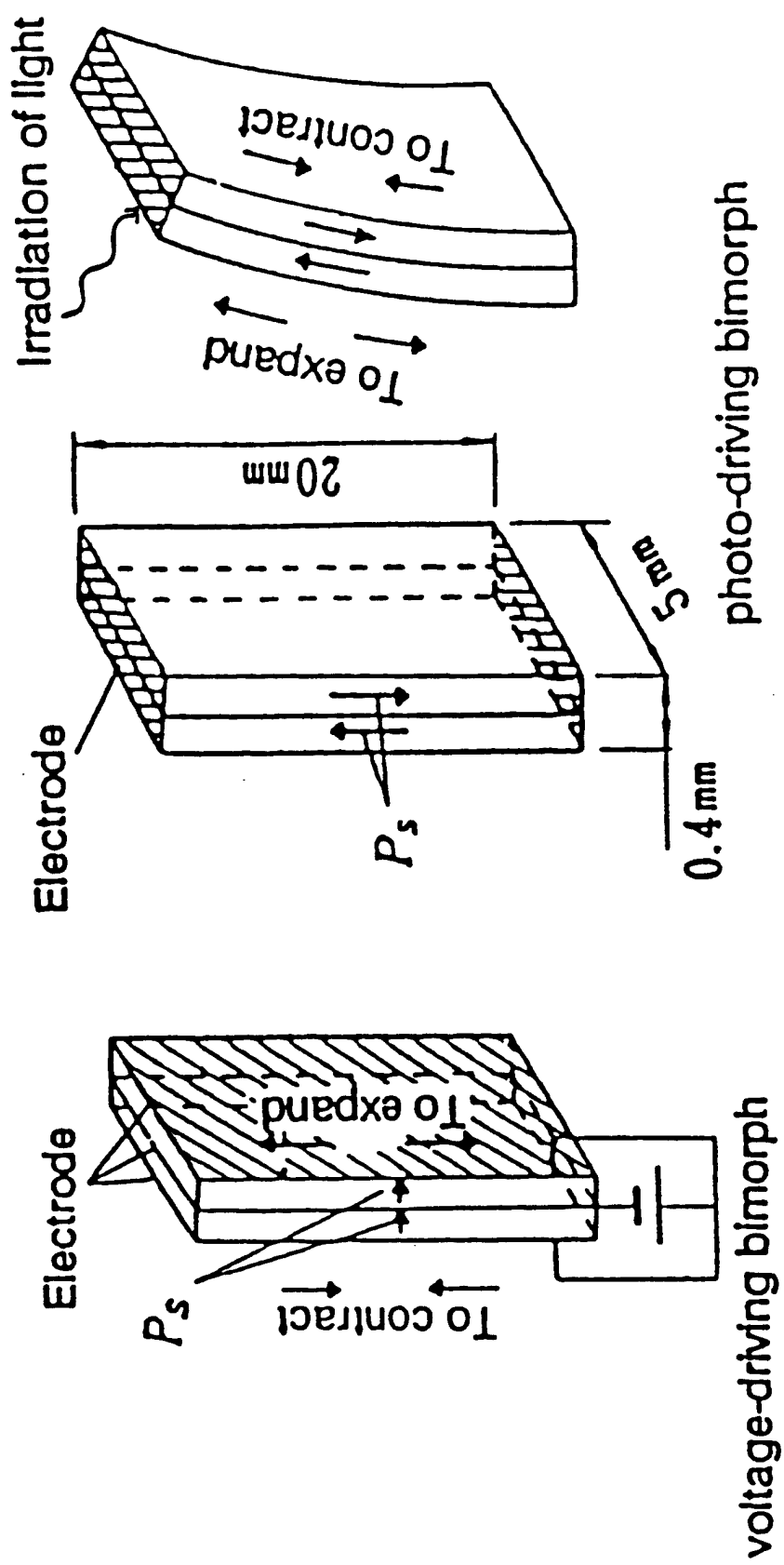


Fig 9 Uchino

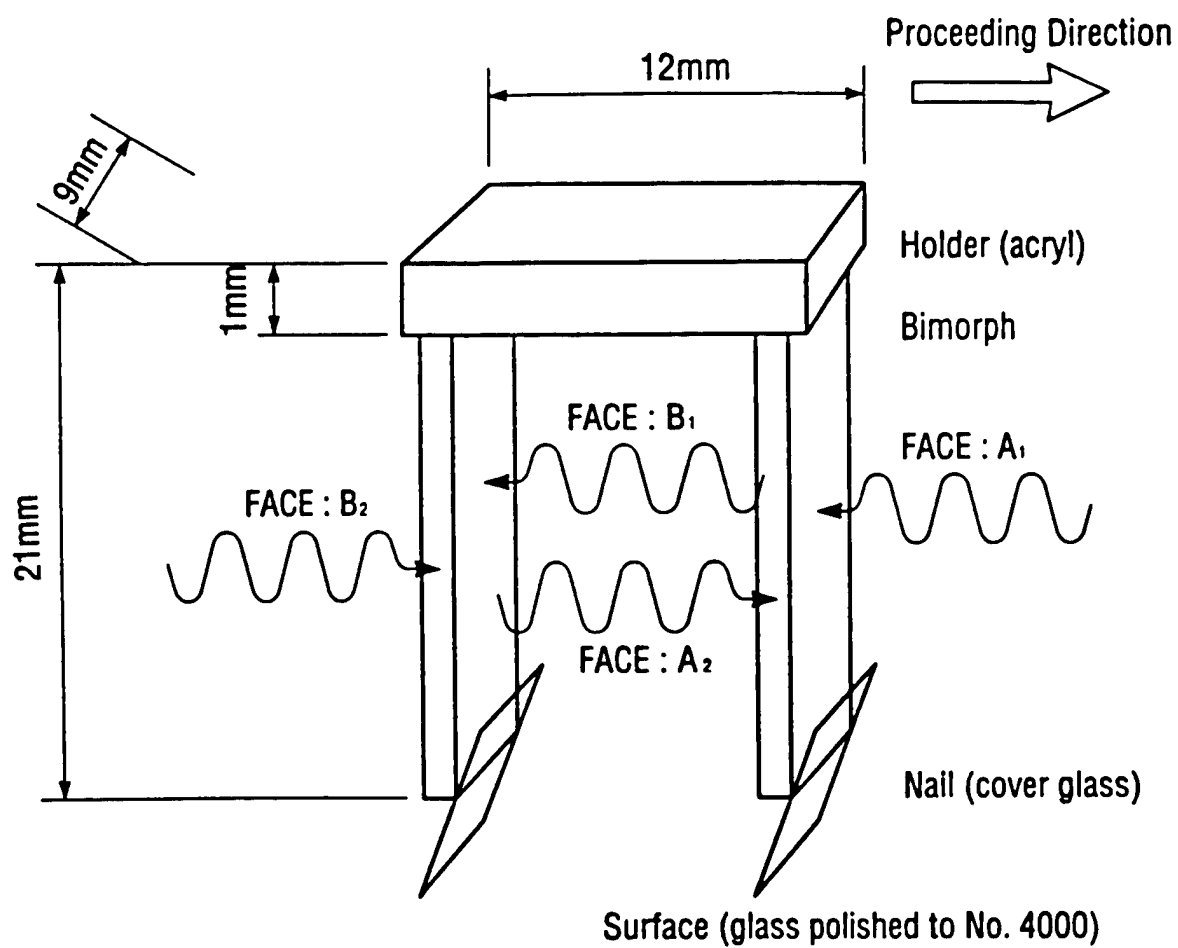
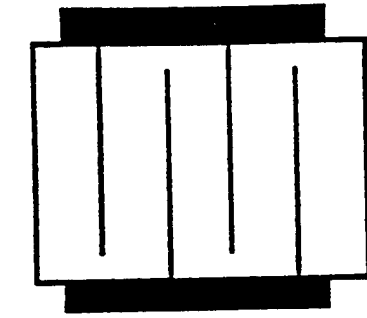
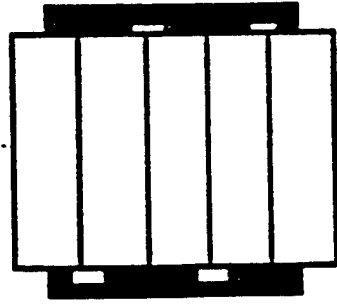


Fig 10 Uchino



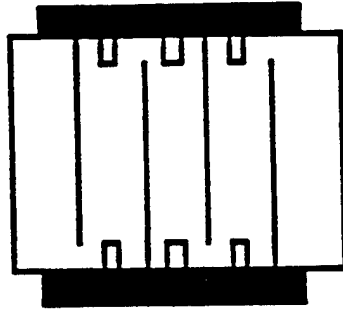
(a)

Interdigital



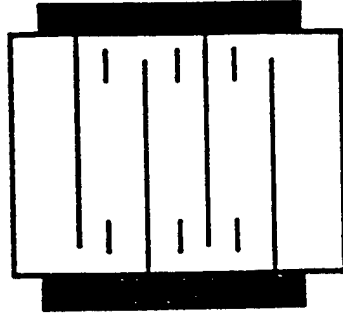
(b)

Plate-through



(c)

Interdigital  
w/slit



(d)

Interdigital  
w/float electrode

Fig 11 Uchino



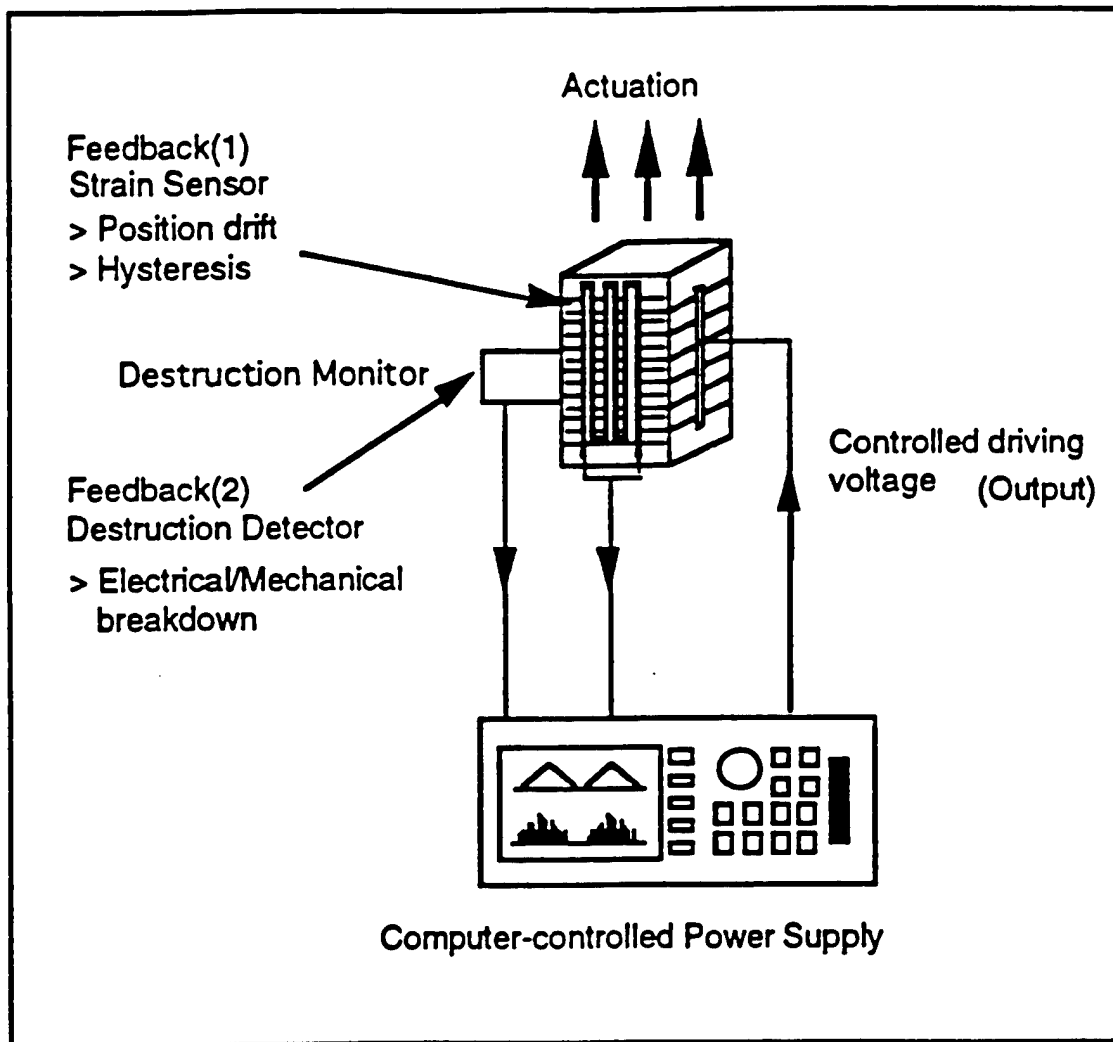


Fig 12 Uchino

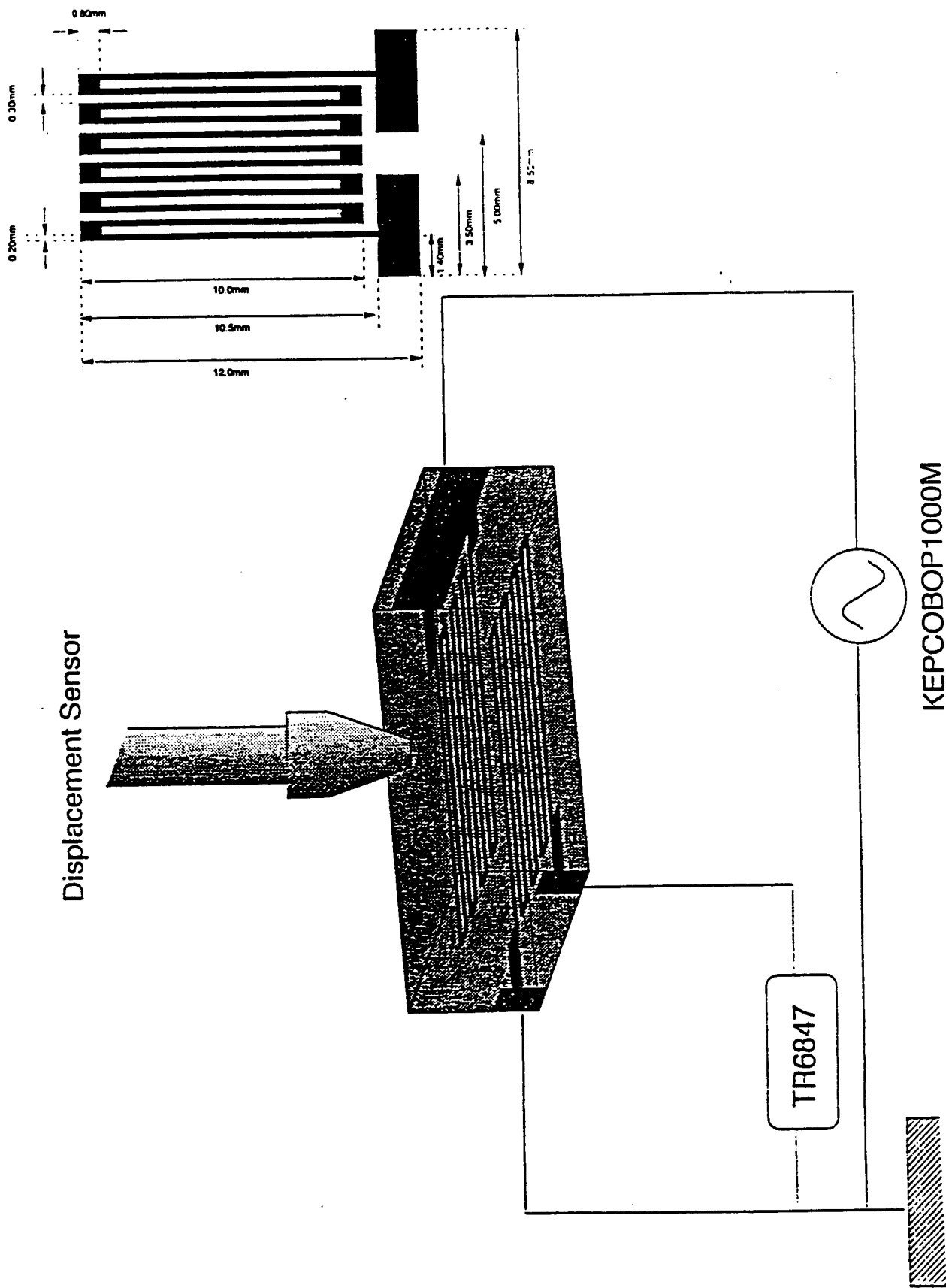


Fig 13 Uchino

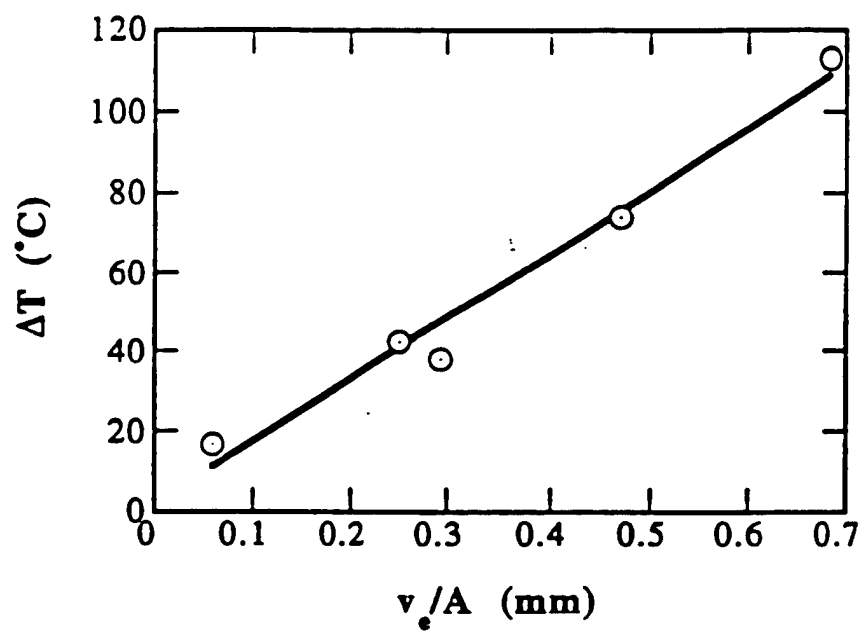


Fig 14 Uchino

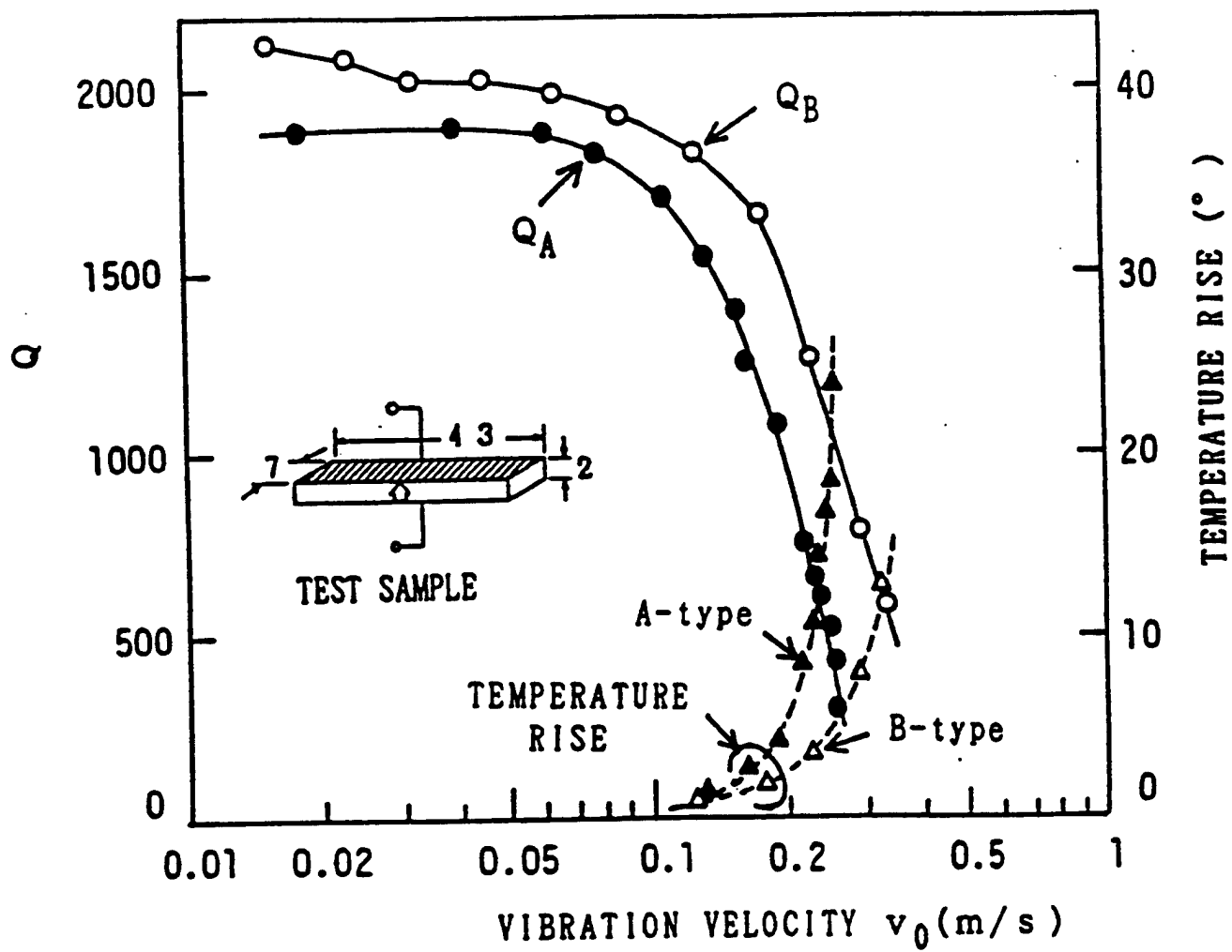


Fig 15 Uchino

# **APPENDIX 58**

## **CHAPTER 8**

### **Shape Memory Ceramics**

1. Development Trends of New Principle Actuators.
2. Shape Memory Ceramics.
3. Sample Preparation and Experiments.
4. Fundamental Properties of the Electric Field-Induced Phase Transition
  - 4.1 Variations in Lattice Parameters
  - 4.2 Temperature Dependence of the Induced Strain
  - 4.3 Composition Dependence of the Induced Strain
  - 4.4 Domain Reorientation Mechanism in Antiferroelectrics
  - 4.5 Pressure Dependence of the Field-Induced Strain
5. Comparison with Shape Memory Alloys
6. Applications of Shape Memory Ceramics
  - 6.1 Latching Relay
  - 6.2 Mechanical Clamper
7. Conclusions

Table I

Figures 1 through 17

**Kenji Uchino**  
Professor, Electrical Engineering  
Director, International Center for Actuators and Transducers  
134 Materials Research Laboratory  
The Pennsylvania State University  
University Park, PA 16802-4800

Phone: (814) 863-8035  
Fax: (814) 865-2326  
E-mail: KenjiUchino@Alpha.mrl.psu.edu

**Abbreviations:**

**AFE:** Antiferroelectric

**FE:** Ferroelectric

**PE:** Paraelectric

**BT:** Barium Titanate

**PZT:** Lead Zirconate Titanate

**PNZST:**  $\text{Pb}_{0.99}\text{Nb}_{0.02}[(\text{Zr}_{0.6}\text{Sn}_{0.4})_{1-y}\text{Ti}_y]_{0.98}\text{O}_3$

**PMN:** Lead Magnesium Niobate

## 1. Development Trends of New Principle Actuators

Recent development of new principle actuators aiming at replacing the conventional electromagnetic motors has been remarkable in the following three areas; precision positioning, vibration suppression and miniature motors. Particular attention has been given to piezoelectric/ electrostrictive ceramic actuators, shape memory devices of alloys such as Ni-Ti and Cu-Zn-Al, and magnetostrictive actuators using Terfenol D (Tb-Dy-Fe) alloys. Rigid strains induced in a piezoelectric ceramic by an external electric field have been used as ultraprecision cutting machines, "hubble" telescopes on the space shuttle and dot-matrix printer heads [Yamada, 1984; Uchino, 1986; Uchino, 1988; Uchino, 1993; and Uchino, 1997]. There has also been proposed a parabolic antenna made of shape memory alloy, which is in a compactly folded shape when first launched on an artificial satellite, and subsequently, recovers its original shape in space when exposed to the heat of the sun. Smart skins on submarines or military tanks are new targets of the solid state actuators [Uchino, 1994b].

In general, thermally-driven actuators such as shape memory alloys can show very large strains, but require large drive energy and exhibit slow response. Magnetic field-driven magnetostrictive devices have serious problems in size because of necessity of magnetic coil and shield. The subsequent Joule heat causes thermal dilatation in the system, and leakage magnetic field interferes sometimes with the operating hybrid electronic circuitry. On the contrary, electric field-driven piezoelectric and electrostrictive actuators have been most developed because of their high efficiency, quick response, compact size, no generation of heat or magnetic field, inspite of relatively small induced strains.

This article reviews shape memory properties of ceramics, focusing on antiferroelectric lead zirconate titanate ( $\text{Pb}(\text{Zr,Ti})\text{O}_3$ , PZT) based ceramics. The shape memory effect can be observed not only in special alloys but also in ceramics such as partial stabilized zirconia and ferroelectric lead zirconate titanate. A new concept of "shape memory" is also proposed in this article: the elastic strain change associated with the



electric field-induced phase transition is utilized instead of stress-induced or thermally-induced phase transitions, which enables much more smart actuator applications than the piezoelectrics or electrostrictors.

The principle of ceramic shape memory effect is described firstly in comparison with the case of alloys. Phase diagrams, domain reversal mechanisms and fundamental actuator characteristics are then discussed, followed by the practical distinctions between these new ceramics and shape memory alloys. Finally, possible unique applications are proposed including a latching relay and a mechanical clamp.

## **2. Shape Memory Ceramics**

"Shape memory" effect is observed not only in special alloys but also in ceramics or in polymers. The shape memory effect in alloys originates from a thermally-induced or stress-induced "martensitic" phase transition. After the alloy is deformed largely in the martensitic state, this apparently permanent strain is recovered to its original shape when heated to cause the reverse martensitic transition. Then, upon cooling, the shape sustains its original state (see Fig. 1(a)).

A similar effect is anticipated in ceramics with a certain phase transition, i.e. a "ferroelastic" phase transition. Reyes-Morel et al. demonstrated the shape memory effect as well as superelasticity in a CeO<sub>2</sub>-stabilized tetragonal zirconia (ZrO<sub>2</sub>) polycrystal [Reyes-Morel, Cherng and Chen, 1988]. Figure 2 is cited from their data, which shows the uniaxial compressive stress versus strain curve at room temperature, together with temperature-strain curve showing strain recovery on heating. Under uniaxial compression, the specimen deforms plastically owing to a stress-induced tetragonal to monoclinic transition in Ce-doped zirconia. Continuous deformation is interrupted by repeated load drops, providing a nearly constant upper yield stress of 0.7 GPa. Even after unloading, large residual plastic axial strain (- 0.7 %) is observed. Subsequent heating produces a gradual recovery of the residual strain due to the reverse phase transition starting at 60°C

and a burst of strain recovery at 186°C. The burst is very sharp, above which approximately 95% of the prior axial strain is recovered.

Ceramic "shape memory" has been reported also for certain ferroelectricity-related transitions, namely paraelectric-ferroelectric [Kimura, Newnham and Cross, 1981] and antiferroelectric-ferroelectric transitions [Uchino, 1985a; and Uchino, 1989]. The former thermally-induced transition revealed a shape-recovery phenomenon similar to zirconia ceramics. On the contrary, the latter is related to an electric field-induced transition, and exhibits large displacement (0.4%) with a "digital" characteristic or a shape memory function, which is in contrast to the essentially "analogue" nature of conventional piezoelectric/electrostrictive strains with 0.1% in magnitude.

Let us review ferroelectricity and antiferroelectricity here for further understanding [Uchino, 1994a]. Figure 3 shows the crystal structure changes in a typical ferroelectric barium titanate ( $\text{BaTiO}_3$ , BT). At an elevated temperature above the transition point of 130°C ("Curie temperature", denoted as  $T_C$ ), BT shows a cubic "perovskite" structure (paraelectric (PE) phase) as illustrated in Fig. 3(a). With decreasing temperature below  $T_C$ , the cations ( $\text{Ba}^{2+}$  and  $\text{Ti}^{4+}$ ) shift against the anions ( $\text{O}^{2-}$ ) as illustrated in Fig. 3(b), exhibiting spontaneous polarization as well as spontaneous strain (ferroelectric (FE) phase). Notice that the electric dipole moment in each crystal unit cell is arranged in parallel in a ferroelectric. On the other hand, there exists an antiferroelectric where the dipole is arranged in antiparallel each other so as not to produce the net polarization. Figure 4 shows two antipolar dipole arrangement models in contrast to nonpolar and polar models.

When the free energy of the antipolar state is close to the energy of the polar state, the dipole configuration is rearranged by the external electric field or stress. Figure 5 shows the applied electric field versus induced polarization curves in PE, FE and AFE materials. A linear relation and a hysteresis due to the spontaneous polarization reversal between positive and negative directions are observed in a PE and in a FE, respectively. On the contrary, an AFE exhibits an electric field-induced phase transition to a FE state

above a critical field  $E_t$ , accompanied by a hysteresis above  $E_t$ . Reducing the field down to zero, the remanent polarization is not observed, providing a so-called "double hysteresis" curve in total. Associated with this phase transition, a large strain jump is theoretically accompanied, which also appears as a double hysteresis. In a certain case, once the FE state is induced, this FE state is sustained even if the electric field is decreased to zero; this corresponds to the "shape memory" phenomenon. The mechanism for the shape memory effect in the AFE ceramics is schematically illustrated in Fig. 1(b).

### 3. Sample Preparation and Experiments

This section introduces sample preparation and experimental procedures of shape memory ceramics.

Antiferroelectric perovskite ceramics from the PZT system have been investigated in which successive phase transitions from a PE, through an AFE, to a FE state appear with decreasing temperature [Berlincourt, Krueger and Jaffe, 1964]. PZT ceramics  $\text{Pb}_{0.99}\text{Nb}_{0.02}[(\text{Zr}_{0.6}\text{Sn}_{0.4})_{1-y}\text{Ti}_y]_{0.98}\text{O}_3$  ( $0.05 < y < 0.09$ ) (abbreviated hereafter as PNZST) were prepared from reagent grade oxide raw materials,  $\text{PbO}$ ,  $\text{Nb}_2\text{O}_5$ ,  $\text{ZrO}_2$ ,  $\text{SnO}_2$  and  $\text{TiO}_2$ . Bulk samples were prepared by hot-press sintering at  $1200^\circ\text{C}$ . Unimorphs were fabricated with two thin rectangular plates (22 mm x 7 mm x 0.2 mm) bonded together. Multilayer samples (12 mm x 4.3 mm x 4.3 mm) with each layer 150  $\mu\text{m}$  in thickness were also fabricated using tape casting technique: those with platinum electrodes were sintered at a temperature of about  $1250^\circ\text{C}$ .

The field induced lattice change was determined by x-ray diffraction. The surfaces of the thin ceramic plate ( $t = 0.2$  mm) were coated with carbon evaporated electrode. X-ray diffraction patterns were recorded at the electrode surface for several different bias voltages. The displacement or strain induced by an alternating electric field (0.05 Hz) was detected with a strain gauge (Kyowa Dengyo, KFR-02-C1-11), a magneto-resistive potentiometer (Midori Precisions, LP-1U) or a differential transformer-type (Millitron, No. 1202). For the dynamic displacement in unimorphs, a noncontact-type eddy current

displacement sensor (Kaman, KD-2300) was used. The electric polarization and the permittivity were measured with a Sawyer-Tower circuit and an impedance analyzer (Hewlett-Packard 4192A), respectively.

To observe the domain structures, a CCD microscope with a magnification of  $\times 1300$  was applied on a thinly-sliced sample of large grain ( $>50\mu\text{m}$ ) PNZST ceramics with interdigital electrodes on the surface.

#### **4. Fundamental Properties of the Electric Field-Induced Phase Transition**

The antiparallel arrangement of electric dipoles in the sublattices of AFE is rearranged in parallel by an applied electric field, and the dielectric and electromechanical properties are changed remarkably associated with this phase change.

##### **4.1 Variations in Lattice Parameters**

The field-induced change in lattice parameters for a sample  $\text{Pb}_{0.99}\text{Nb}_{0.02}[(\text{Zr}_{0.6}\text{Sn}_{0.4})_{1-y}\text{Ti}_y]_{0.98}\text{O}_3$  with  $y = 0.06$  is plotted in Fig. 6(a) [Uchino and Nomura, 1983]. The forced transition from the AFE to the FE phase gives rise to the simultaneous increase of  $a$  and  $c$  in the perovskite unit cell, thereby keeping the tetragonality,  $c/a$ , nearly constant. Since  $\gamma$  makes only a negligible contribution to the volume change, the strain change at the phase transition is nearly isotropic with a magnitude of  $\Delta L/L = 8.5 \times 10^{-4}$ .

The intensity change of the x-ray reflections with the application of an electric field suggests that the spontaneous polarization in the FE state lies in the  $c$ -plane, parallel with the perovskite  $[1\ 1\ 0]$  axis, and that the sublattice polarization configuration in the AFE state is very similar to that of  $\text{PbZrO}_3$  [Fujishita and Hoshino, 1984]. Figure 6(b) illustrates the simplest two-sublattice model.

## 4.2 Temperature Dependence of the Induced Strain

The temperature dependence of the field induced strain is described for the sample with  $y = 0.06$  in conjunction with the dielectric measurements [Uchino and Nomura, 1983].

Figure 7 shows the relation between the electric field and polarization. The typical double and ferroelectric hysteresis loops are observed at room temperature and  $-76^{\circ}\text{C}$ , respectively, while a transitive shape with humps is observed at intermediate temperatures.

The transitive process can be observed more clearly in the strain curve. Figure 8 shows the transversely induced strains. The forced transition from AFE to FE at room temperature is characterized by a huge strain discontinuity. On the other hand, a typical ferroelectric butterfly-type hysteresis is observed at  $-76^{\circ}\text{C}$ , corresponding to polarization reversal. It is important to note that the strain discontinuities associated with the phase transition have the same positive expansion in both longitudinal and transverse directions with respect to the electric field (i. e. the apparent Poisson's ratio is negative!), while the piezoestriction exhibits negative and positive in the transverse and longitudinal directions, respectively.

The shape memory effect is observed on this loop at  $-4^{\circ}\text{C}$ . When a large electric field is applied to the annealed AFE sample, a massive strain  $\Delta L/L$  of about  $7 \times 10^{-4}$  is produced and maintained metastably even after the field is removed. After applying a small reverse field or thermal annealing, the original AFE shape is observed.

The reverse critical field related to the FE - AFE transition is plotted with solid lines in the phase diagram for the sample with  $y = 0.06$  (see Fig. 9). In the temperature range from  $-30^{\circ}\text{C}$  to  $10^{\circ}\text{C}$ , a hump-type hysteresis in the field versus polarization curve and an inverse hysteresis in the field-induced strain are observed: this has previously been often misinterpreted as another AFE phase different from the phase above  $10^{\circ}\text{C}$ . The annealed state below  $-30^{\circ}\text{C}$  down to  $-200^{\circ}\text{C}$  is AFE. However, once the FE state is induced, the AFE phase is never observed during a cycle of rising and falling electric field. The critical field line for the FE to AFE transition (the solid line) in the temperature range  $-30^{\circ}\text{C}$  to

10°C intersects the coercive field line for the +FE to -FE reversal (the dashed line) below -30°C.

### 4.3 Composition Dependence of the Induced Strain

Figure 10 shows the strain curves induced transversely by the external field at room temperature for samples of several different compositions [Uchino, 1985b]. The molar fraction of Ti,  $y$ , is increased from 0.06 (a) to 0.065 (c). The initial state was obtained by annealing at 150°C, which is above the Curie (or Neel) temperature for all the samples. A typical double hysteresis curve (Type I) is observed in the sample containing  $y = 0.06$ . Large jumps in the strain are observed at the forced phase transitions from the AFE to the FE phase ( $\Delta L/L = 8 \times 10^{-4}$ ). In comparison, the strain change with electric field in either the AFE or FE state is rather small: this suggests a possible application for the material as a "digital" displacement transducer, having OFF/ON displacive states. The difference in the strain between that occurring in the initial state and that appearing in a cyclic process at  $E = 0$  kV/cm is also noteworthy and will be explained in the following section.

In the sample with  $y = 0.063$ , a Ti concentration slightly higher than that just described, the field induced FE phase will not return to the AFE state even after decreasing the field to zero (Type II, Fig. 10(b)): this is called "memorizing" the FE strain state. In order to obtain the initial AFE state, a small reverse bias field is required. Figure 10(c) shows the strain curve for the sample with  $y = 0.065$ , which exhibits irreversible characteristics during an electric field cycle (Type III). The initial strain state can only be recovered by thermal annealing up to 50°C.

Data derived from these strain curves may be utilized to construct a phase diagram of the system  $\text{Pb}_{0.99}\text{Nb}_{0.02}[(\text{Zr}_{0.6}\text{Sn}_{0.4})_{1-y}\text{Ti}_y]_{0.98}\text{O}_3$  at room temperature with respect to the composition  $y$  and the applied electric field  $E$  (Fig. 11). If the Ti concentration of the horizontal axis is redefined in terms of temperature and evaluated in the opposite direction, this phase diagram is topologically the same as the phase diagram of Fig. 9. The key feature of this phase diagram is the existence of the three phases, namely the AFE, the

positively poled FE (+FE), and the negatively poled FE (-FE) phases, the boundaries of which are characterized by the two transition lines corresponding to rising and falling electric fields.

The composition regions I and IV exhibit the typical double hysteresis and ferroelectric domain reversal, respectively. The shape memory effect is observed in regions II and III. It is important to consider the magnitude of the electric field associated with the +FE  $\rightarrow$  AFE transition and the +FE  $\rightarrow$  -FE transition (notice the direction of the arrow!). Let us consider the transition process under an inverse bias field after the +FE is induced by the positive electric field. If the magnitude of the field for the +FE  $\rightarrow$  AFE transition is smaller than the coercive field for +FE  $\rightarrow$  -FE (region II,  $0.0625 < y < 0.065$ ), the AFE phase appears once under a small inverse field, then the -FE phase is induced at the AFE  $\rightarrow$  -FE transition field. In this case, the shape memory is reversible to the initial state only with the application of a reverse electrical field (Type II): this is very useful! On the other hand, if the +FE  $\rightarrow$  -FE coercive field is smaller than the +FE  $\rightarrow$  AFE field (region III,  $0.065 < y < 0.085$ ), the domain reversal to -FE appears without passing through the AFE phase. The initial state can be obtained by thermally annealing up to 50 - 70°C (Type III).

#### 4.4 Domain Reorientation Mechanism in Antiferroelectrics

Antiferroelectrics cannot be poled macroscopically. However, since they have sublattice polarizations closely coupled with the lattice distortion, it is possible to consider ferroelastic domain orientations in "anti-" ferroelectrics. This is a possible approach to understanding the difference in the strain between that occurring in the initial state and that arising in a cyclic process, as shown in Fig. 10(a).

Figure 12 shows the longitudinal and transverse strains induced in the sample  $y = 0.075$  in region III [Uchino, 1985b]. The strain induction process can be considered to consist of two stages: first, there is an isotropic volume expansion ( $O \rightarrow A, A'$ :  $\Delta L/L = 8 \times 10^{-4}$ ) due to the AFE to FE phase transition (Remember Fig. 6(a), where the perovskite

cell expands isotropically by  $\Delta L/L = 8.5 \times 10^{-4}$ ), and second, there is an anisotropic strain associated with the FE domain rotation ( $A \rightarrow B$ ,  $A' \rightarrow B'$ :  $x_3 = 9 \times 10^{-4}$ ,  $x_1 = -3 \times 10^{-4}$ ). This process is shown schematically in Fig. 13, where a probable model for the double-hysteresis sample (region I) is also illustrated. As previously pointed out, even for AFEs, domain reorientation is possible through the forced phase transition to FEs.

Domain configuration in PNZST  $y=0.063$  (Type II) was observed as a function of electric field at room temperature [Oh, Cross and Uchino, 1995]. No clear domains were observed at the initial state obtained by annealing the sample at 70°C. As increasing the electric field, clear domain walls appeared above 20 kV/cm, arranged almost perpendicularly to the electric field direction. This value of electric field is coincident with the critical field which can cause the transition from AFE to FE. Therefore, these domain walls were caused by the induced ferroelectricity. The domain walls did not diminish during removing the electric field, because the sample has the shape memory effect. The walls disappeared when slightly negative bias was applied, as expected in the Type II specimen.

#### 4.5 Pressure Dependence of the Field-Induced Strain

One of the most important criteria for an actuator is reliable and stable driving under a large applied stress, as required for its application as a positioner in precision cutting machinery. Figure 14 shows the longitudinally induced strains in a shape memory sample of PNZST  $y = 0.07$  in both the AFE and FE states at room temperature plotted as a function of uniaxial compressive stress for several electric fields [Uchino, 1989]. For comparison, similar plots for a lead magnesium niobate (PMN) based ceramic ( $\text{Pb}(\text{Mg}_{1/3}\text{Nb}_{2/3})_{0.65}\text{Ti}_{0.35}\text{O}_3$ , a well-known electrostrictive material) are also shown.

Roughly speaking, the strain versus stress curve for the AFE PNZST ceramic is shifted along the strain axis with respect to that for PMN due to the difference between the spontaneous strains in the AFE and the FE states. Consequently, the maximum generative force obtained when the ceramic is mechanically clamped so as not to generate a



displacement, is raised up to 80 MPa in comparison with the normal value for the ferroelectric, 35 MPa.

## **5. Comparison with Shape Memory Alloys**

The phenomenon associated with shape memory alloys is attributed to the stress-induced (as well as thermally-induced) phase transition referred to as "martensitic". The new strain phenomena in AFE ceramics described here are very easily understandable, if we use the terminology conventionally used for these alloys, replacing electric field  $E$  for stress  $X$ . The "digital displacement" and the ferroelectric-state memorization discussed here correspond to the "super-elasticity" and the shape memory effect in the alloys, respectively.

Outstanding merits of the ceramics over the alloys are:

- 1) quick response in msec,
- 2) good controllability by electric field to memorize and recover the shape without generating heat,
- 3) low energy consumption as low as 1/100 of the alloy, and
- 4) wide space is not required to obtain the initial shape deformation.

Numerical comparison is shown in Table I.

## **6. Applications of Shape Memory Ceramics**

The conventional piezoelectric/electrostrictive actuators have been developed with the aim of realizing "analogue displacement transducers", in which a certain magnitude of electric field corresponds to only one strain state without any hysteresis during rising and falling electric field. This is exemplified by the electrostrictive PMN based ceramics. On the contrary, the antiferroelectrics introduced in this article may be utilized in a device based on a new concept, "a digital displacement transducer", in which bistable ON/OFF strain states exist for a certain electric field. This idea may be interpreted as a stepping motor in the conventional terminology of electro-magnetic motors. The discrete movement through

a constant distance achieved by the new actuator is well suited for applications such as an optical-grid manufacturing apparatus or a swing-type charge coupled device.

The shape memory material can be applied for such devices as latching relays and mechanical clampers, where the ceramic is capable of maintaining the excited ON state even when electricity is not applied on it.

### 6.1 Latching Relay

Figure 15 shows the structure of a newly fabricated latching relay, which is composed essentially of a mechanical snap-action switch and a shape memory unimorph driving part [Furata, Oh and Uchino, 1992]. The snap-action switch is easily driven by a 50  $\mu\text{m}$  displacement, having mechanically bistable states. The unimorph is fabricated with two  $y = 0.063$  ceramic plates of 22 mm x 7 mm area and 0.2 mm thickness, bonded together with adhesive.

Figure 16 shows the dynamical response of the unimorph. It is important to note that the phase transition arises quickly enough to generate the following mechanical resonant vibration (Fig. 16(a)). When the rise time of the electric field is adjusted to 4.7 ms (Fig. 16(b)), which is the sum of the mechanical resonant period (2.2 ms) and the lag time to cause the phase transition (2.5 ms), the ringing can be suppressed completely.

The new relay is very compact in size, 1/10 of a conventional electromagnetic type, and is operated by a pulse voltage, which provides a significant energy saving. The relay is turned ON at 350V with 4 ms rise time, and turned OFF at -50V.

### 6.2 Mechanical Clamper

A mechanical clamper suitable for microscope sample holders has been constructed by combining a 20-layer shape memory stacked device ( $y = 0.0635$ ) and a hinge-lever mechanism as shown in Fig. 17 [Furata, Oh and Uchino, 1991]. Application of a 1 ms pulse voltage of 200V can generate the longitudinal displacement of 4  $\mu\text{m}$  in the 4 mm-

thick multilayer device, leading to 30  $\mu\text{m}$  tip movement of the hinge lever after displacement amplification. Stable grip was verified for more than several hours.

## **7. Conclusions**

The study of shape memory antiferroelectric materials has only just begun in the past several years. Further investigations on the improvement of the induced strain magnitude, the stability of the strain characteristics with respect to temperature change, mechanical strength and durability after repeated driving are required to produce practical and reliable materials. This category of ceramic actuators, as well as piezoelectric/electrostrictive materials, will be a vital new element in the next generation of "micro-mechatronic" or electromechanical actuator devices.

## REFERENCES

- Berlincourt, D., H.H.A. Krueger and B.Jaffe, J. Phys. & Chem. Solids, **25**, 659 (1964).
- Fujishita, H. and S.Hoshino, J. Phys. Soc. Jpn., **53**, 226 (1984).
- Furata, A., K.Y.Oh and K.Uchino, Proc.Int'l Symp.Appl.Ferroelectrics '90, 528, (1991).
- Furata, A., K.Y.Oh and K.Uchino, Sensors and Mater., **3**, (4), 205 (1992).
- Kimura, T., R.E.Newnham and L.E.Cross, Phase Transitions, **2**, 113 (1981).
- Oh, K.Y., L.E.Cross and K.Uchino, J.Adv.Performance Mater. (1996) [in press].
- Reyes-Morel, P.E., J.S.Cherng and I.W.Chen, J.Amer.Ceram.Soc., **71**, (8), 648 (1988).
- Uchino, K., L.E.Cross and R.E.Newnham, Jpn.J.Appl.Phys., **19**, (7), L425 (1980).
- Uchino, K., L.E.Cross and R.E.Newnham and S.Nomura, J.Appl.Phys., **52**, 1455 (1981).
- Uchino, K., Solid State Phys., **17** (7), 371 (1982).
- Uchino, K. and S.Nomura, Ferroelectrics, **50**, 191 (1983).
- Uchino, K., Oyo Butsuri, **54**, (6), 591 (1985a).
- Uchino, K., Jpn.J.Appl.Phys., **24** (24-2), 460 (1985b).
- Uchino, K., *Piezoelectric/Electrostrictive Actuators*, Morikita Pub. Co., Tokyo (1986).
- Uchino, K., FC Annual Report for Oversea's Readers, Fine Ceram.Soc.Jpn., 23 (1988).
- Uchino, K., Proc.MRS Int'l Mtg. on Adv.Mater., **9**, 489 (1989).
- Uchino, K., Mater.Res.Soc.Bull., **18** (4), 42 (1993).
- Uchino, K., Chap. 12 Ferroelectric Ceramics of *Structure and Properties of Ceramics*, Edit. by M. Swain, VCH, New York (1994a).
- Uchino, K., Chap. 1 Introduction, *Handbook on New Actuators for Precision Control*, Fuji Technosystem, Tokyo (1994b).
- Uchino, K., *Piezoelectric Actuators and Ultrasonic Motors*, Kluwer Academic Publishers, Massachusetts (1997).
- Yamada, H., Editor, *Essentials to Developments and Applications of New Method/ Principle Motors*, Jpn. Industrial Tech. Center, Tokyo (1984).

Table I. Comparison of the shape memory characteristics between alloys and antiferroelectric ceramics.

Properties	Antiferroelectric	Shape Memory Alloy
Driving Power	Voltage (mW ~ W)	Heat (W ~ kW)
Strain ( $\Delta L/L$ )	$10^{-3} \sim 10^{-2}$	$10^{-2} \sim 10^{-1}$
Generative Force	100 MPa	1000 MPa
Response Speed	m sec	sec ~ min
Durability	$> 10^6$ cycles	$10^4$ cycles

## FIGURE CAPTIONS

- Figure 1. Comparison of the mechanisms for the shape memory effect in alloys and in antiferroelectric ceramics.
- Figure 2. Uniaxial compressive stress vs. strain curve for Ce-doped tetragonal zirconia polycrystal at room temperature, together with temperature-strain curve showing strain recovery [after Reyes-Morel, Cherng and Chen (1988)].
- Figure 3. Crystal structures of barium titanate in the paraelectric state (a), and in the ferroelectric state (b).
- Figure 4. Two antipolar dipole arrangement models (c) in contrast to nonpolar (a) and polar (b) models.
- Figure 5. Electric field vs. induced polarization curves in paraelectric (a), ferroelectric (b) and antiferroelectric (c) materials.
- Figure 6. (a) Variation of lattice parameters with bias electric field at room temperature ( $y = 0.06$ ); (b) Two sublattice model of the polarization configuration for the AFE and FE states [after Uchino and Nomura (1983)].
- Figure 7. Polarization plotted as a function of electric field for several temperatures ( $y = 0.06$ ) [after Uchino and Nomura (1983)].
- Figure 8. Transverse elastic strain induced by the electric field at several temperatures ( $y = 0.06$ ) [after Uchino and Nomura (1983)].
- Figure 9. Phase diagram on the temperature-electric field plane for  $\text{Pb}_{0.99}\text{Nb}_{0.02}[(\text{Zr}_{0.6}\text{Sn}_{0.4})_{0.94}\text{Ti}_{0.06}]_{0.98}\text{O}_3$ .
- Figure 10. Transverse induced strains of  $\text{Pb}_{0.99}\text{Nb}_{0.02}[(\text{Zr}_{0.6}\text{Sn}_{0.4})_{1-y}\text{Ti}_y]_{0.98}\text{O}_3$  at room temperature: (a) for  $y = 0.06$ ; (b) for  $y = 0.063$ ; and (c) for  $y = 0.065$  [after Uchino (1985b)].
- Figure 11. Phase diagram of  $\text{Pb}_{0.99}\text{Nb}_{0.02}[(\text{Zr}_{0.6}\text{Sn}_{0.4})_{1-y}\text{Ti}_y]_{0.98}\text{O}_3$  at room temperature with respect to the composition  $y$  and the applied electric field  $E$ .
- Figure 12. Longitudinal and transverse induced strains of the sample  $\text{Pb}_{0.99}\text{Nb}_{0.02}[(\text{Zr}_{0.6}\text{Sn}_{0.4})_{0.925}\text{Ti}_{0.075}]_{0.98}\text{O}_3$  [after Uchino (1985b)].
- Figure 13. Schematic illustration of the antiferroelectric domain reorientation associated with the forced phase transition.
- Figure 14. Longitudinal induced strains in a shape memory sample  $\text{Pb}_{0.99}\text{Nb}_{0.02}[(\text{Zr}_{0.6}\text{Sn}_{0.4})_{0.93}\text{Ti}_{0.07}]_{0.98}\text{O}_3$  at room temperature plotted as a function of uniaxial compressive stress [after Uchino (1989)].
- Figure 15. Structure of the latching relay using shape memory ceramic.
- Figure 16. Dynamical response of the tip displacement of the shape memory unimorph with  $y = 0.063$  under various drive pulse conditions [after Furata, Oh and Uchino (1992)].
- Figure 17. Construction of the mechanical clamper using a shape memory multilayer device.

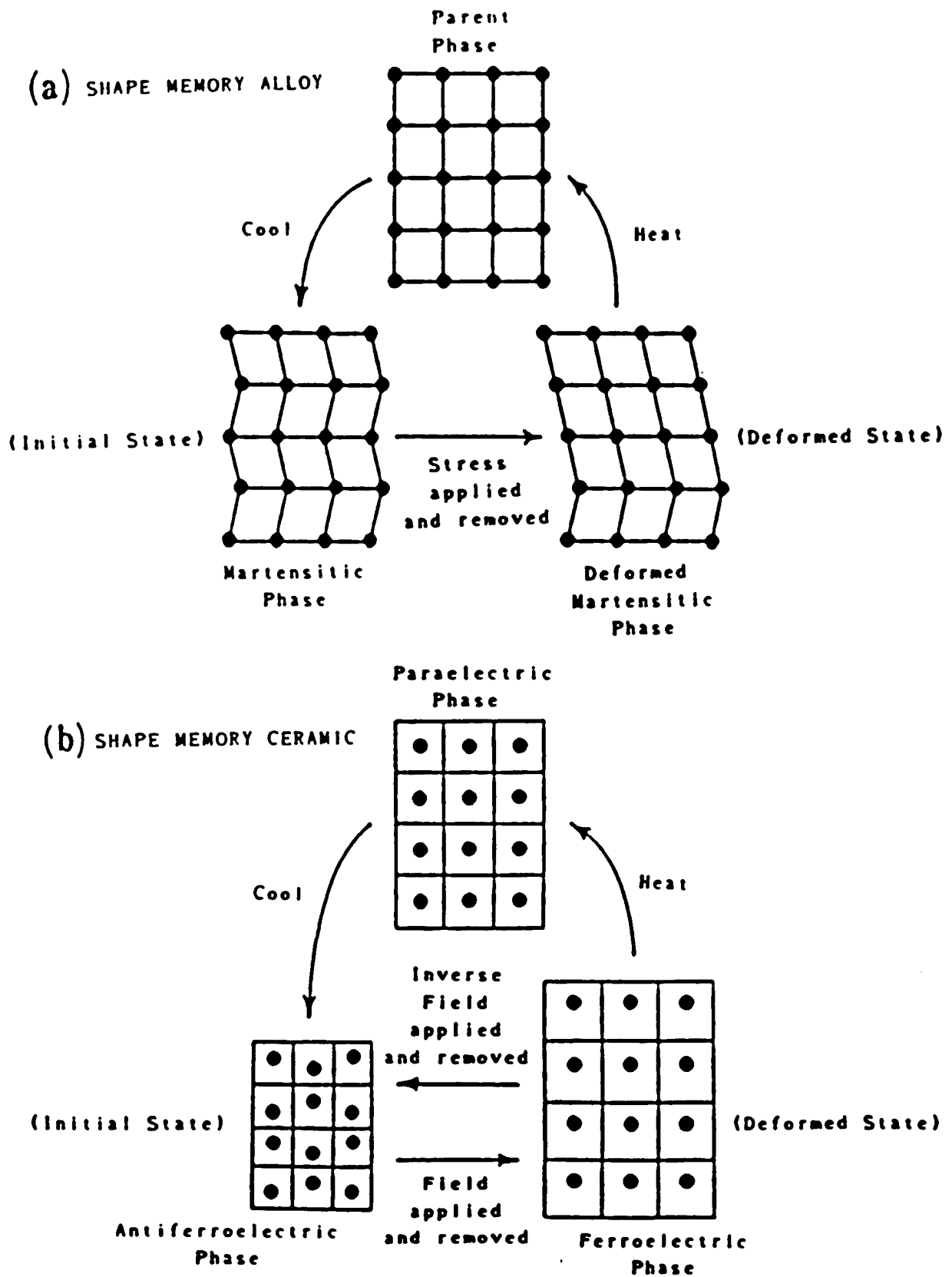


Figure 1. Comparison of the mechanisms for the shape memory effect in alloys and in antiferroelectric ceramics.

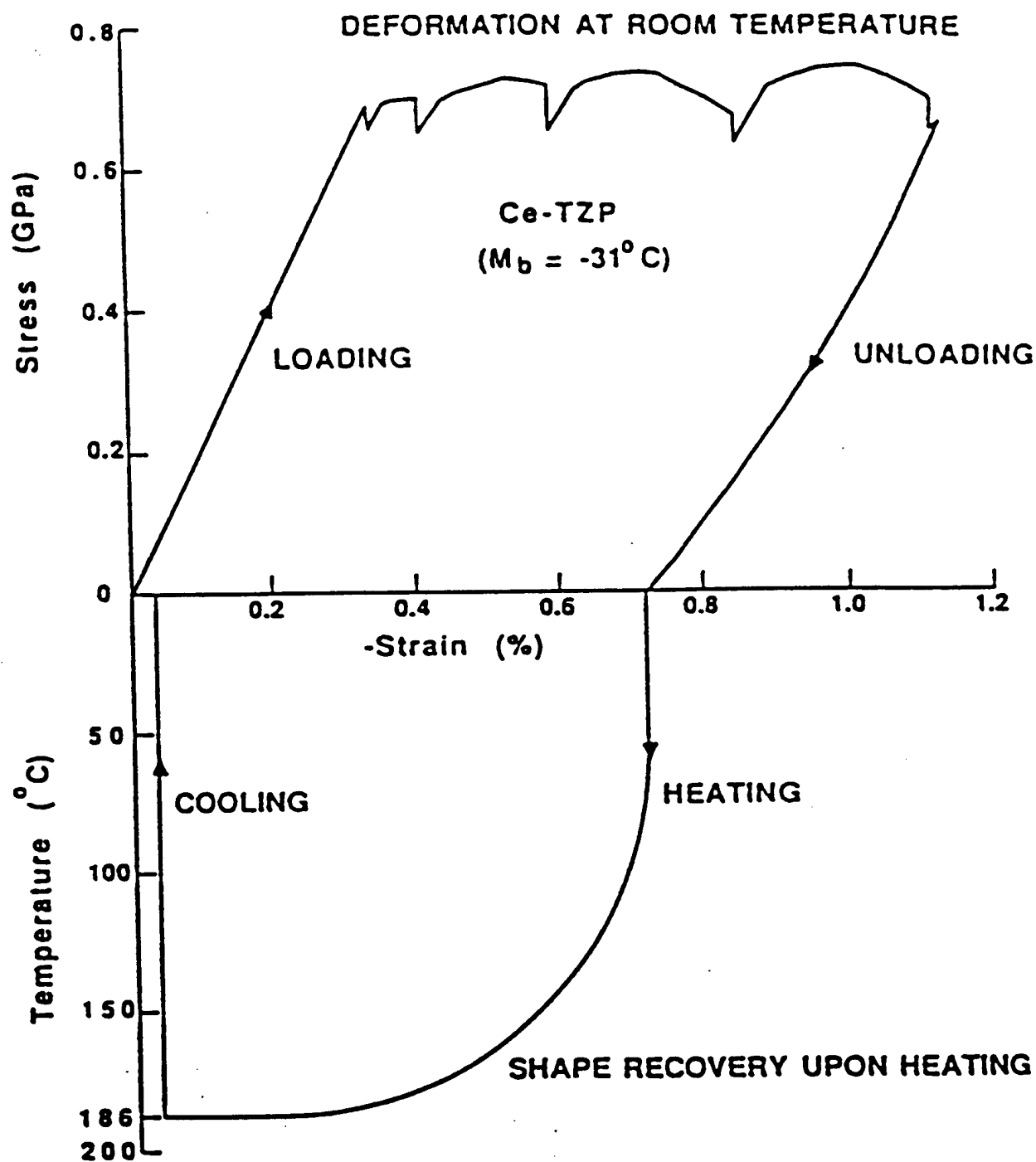


Figure 2. Uniaxial compressive stress vs. strain curve for Ce-doped tetragonal zirconia polycrystal at room temperature, together with temperature-strain curve showing strain recovery [after Reyes-Morel, Cherng and Chen (1988)].



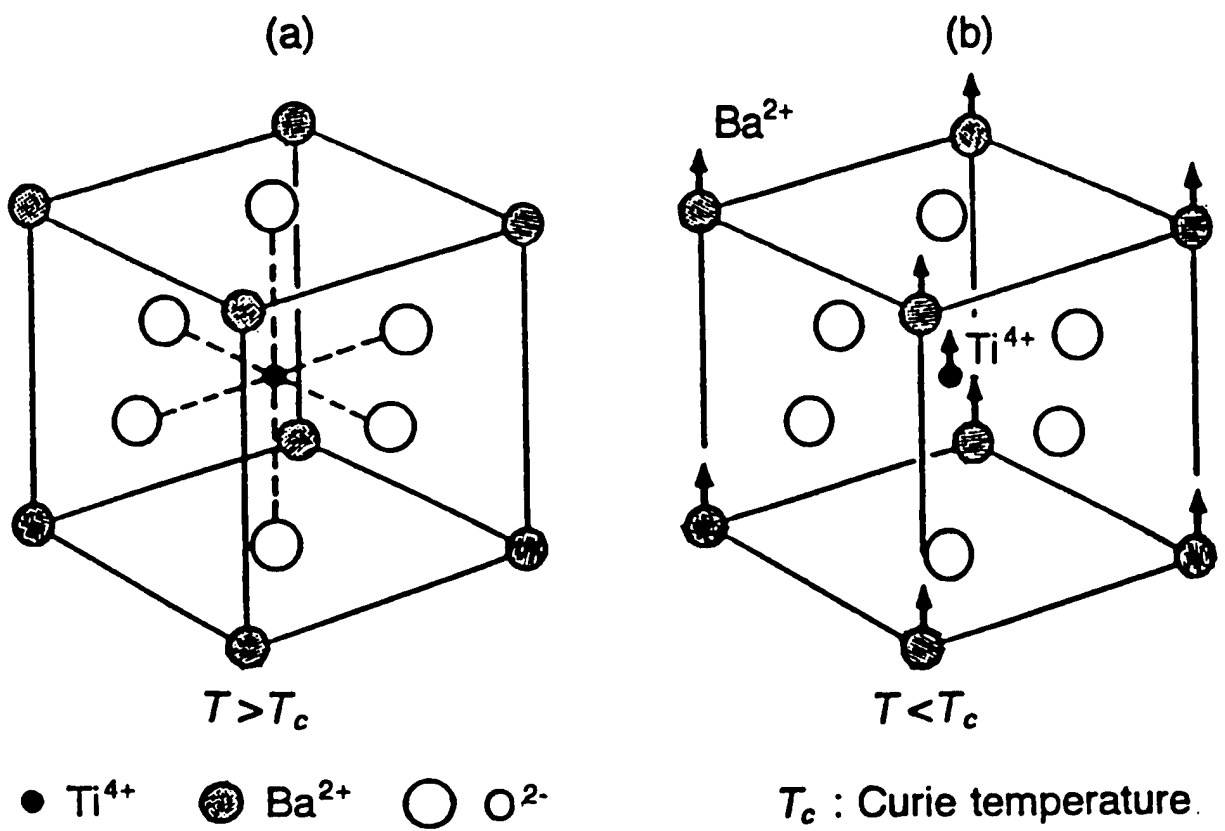
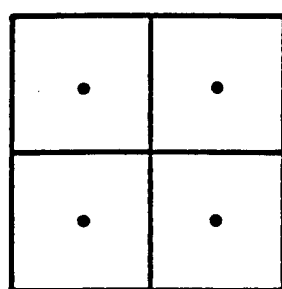
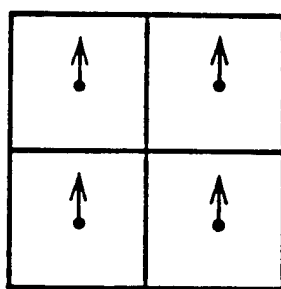


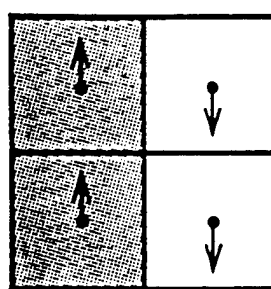
Figure 3. Crystal structures of barium titanate in the paraelectric state (a), and in the ferroelectric state (b).



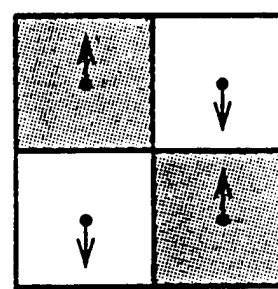
(a) **Nonpolar**



(b) **Polar**



**Stripe-type**



**Checkerboard-type**

(c) **Antipolar**

Figure 4. Two antipolar dipole arrangement models (c) in contrast to nonpolar (a) and polar (b) models.

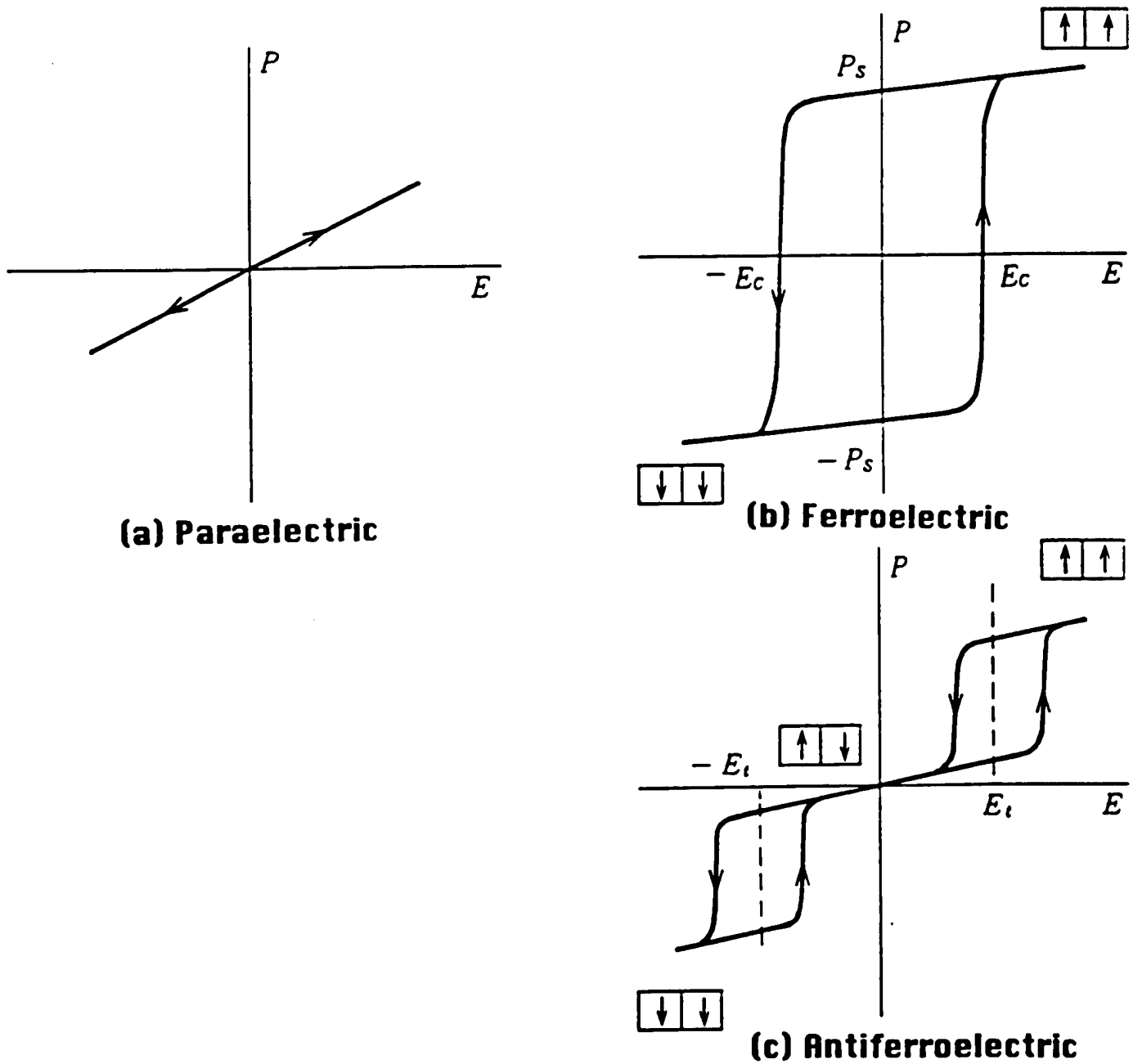


Figure 5. Electric field vs. induced polarization curves in paraelectric (a), ferroelectric (b) and antiferroelectric (c) materials.

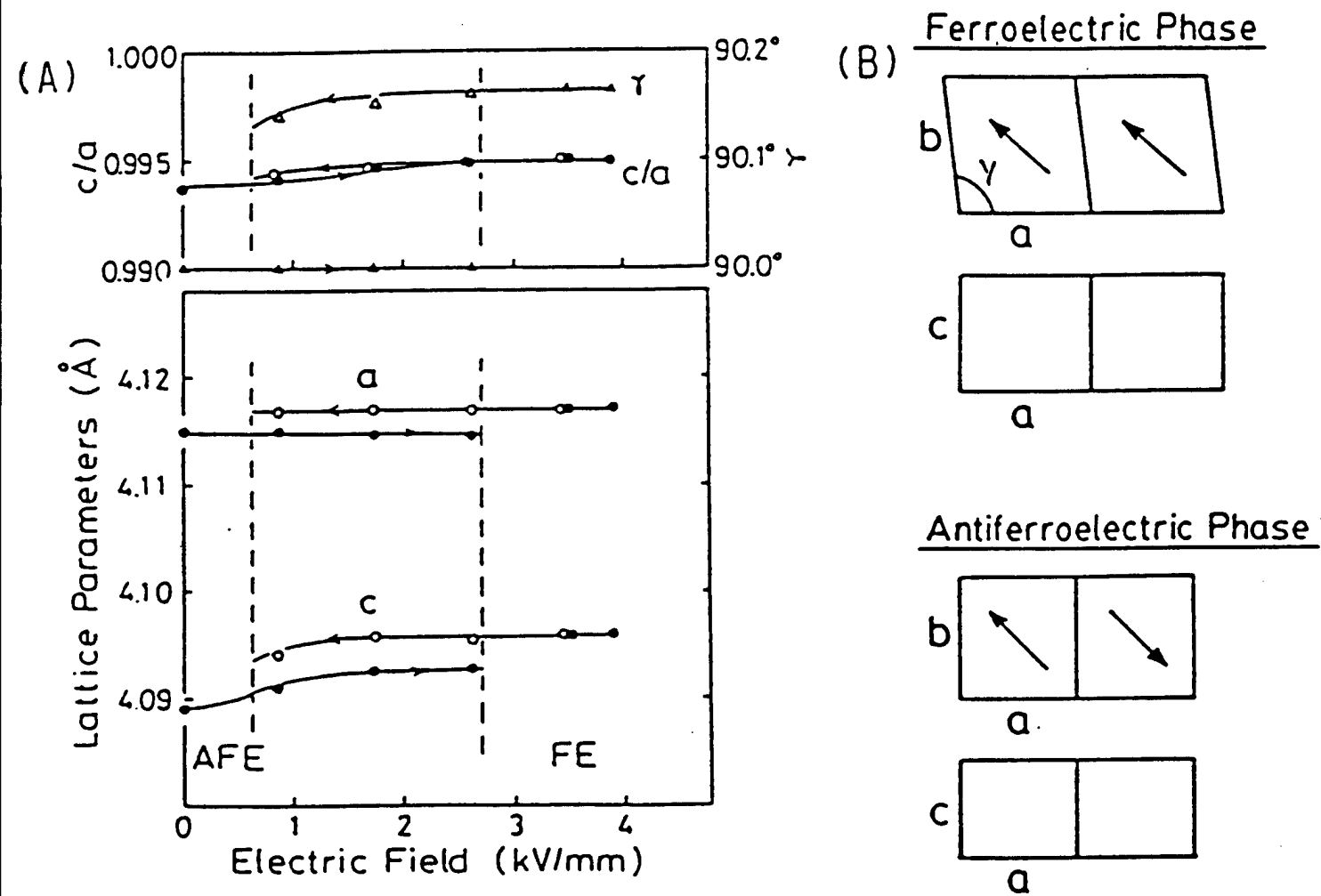


Figure 6. (a) Variation of lattice parameters with bias electric field at room temperature ( $y = 0.06$ ); (b) Two sublattice model of the polarization configuration for the AFE and FE states [after Uchino and Nomura (1983)].

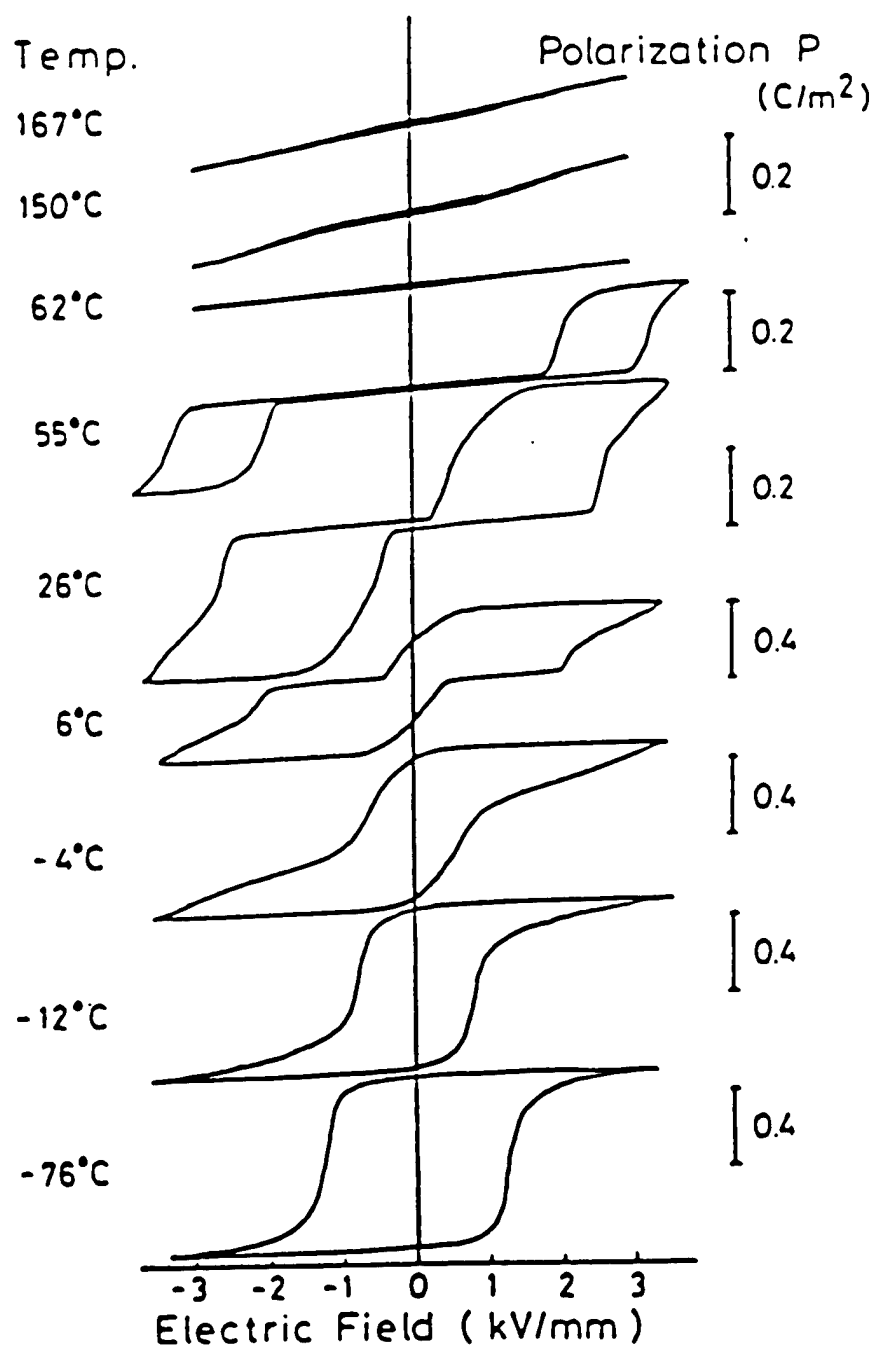


Figure 7. Polarization plotted as a function of electric field for several temperatures ( $y = 0.06$ )[after Uchino and Nomura (1983)].

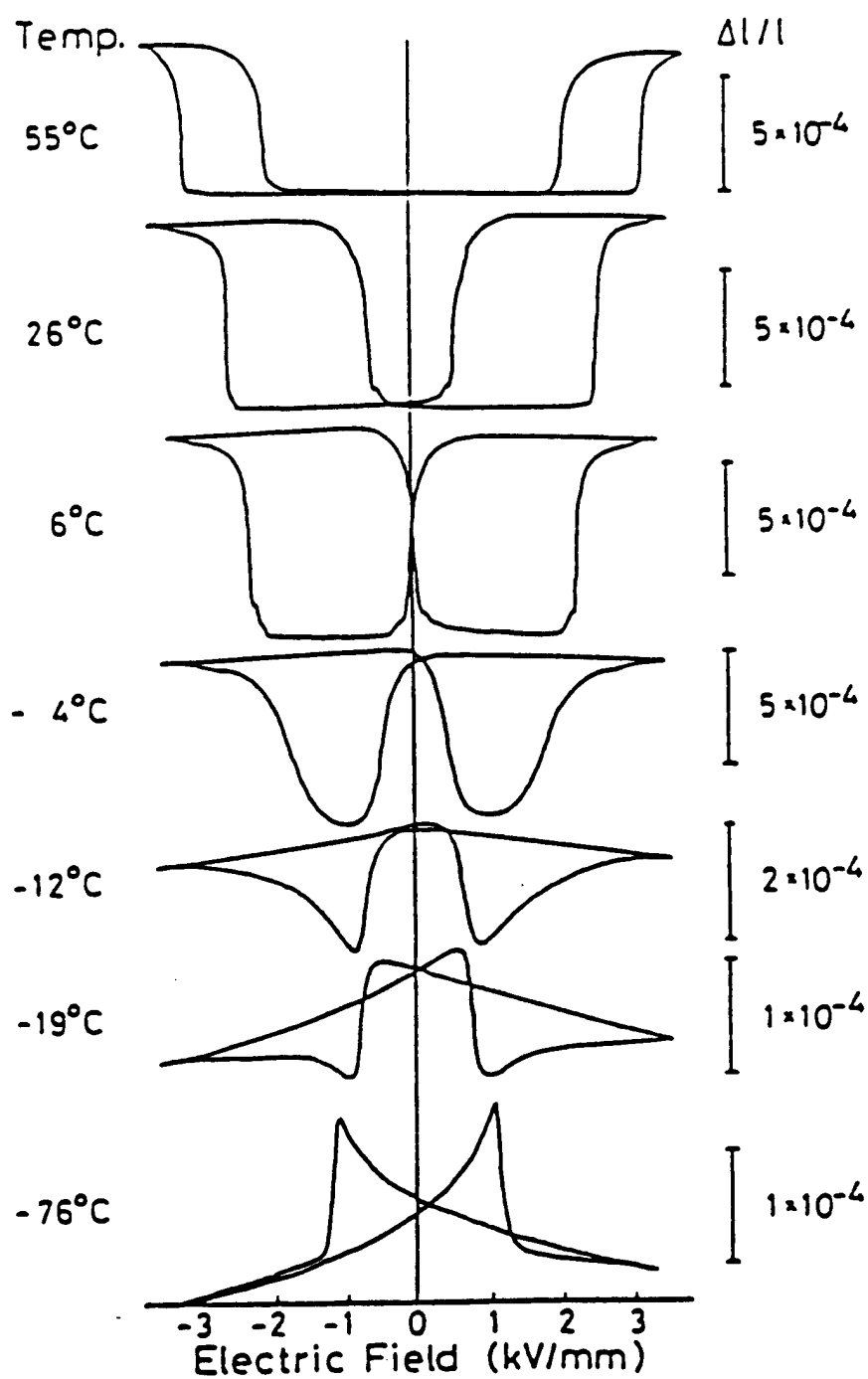


Figure 8. Transverse elastic strain induced by the electric field at several temperatures ( $y = 0.06$ ) [after Uchino and Nomura (1983)].

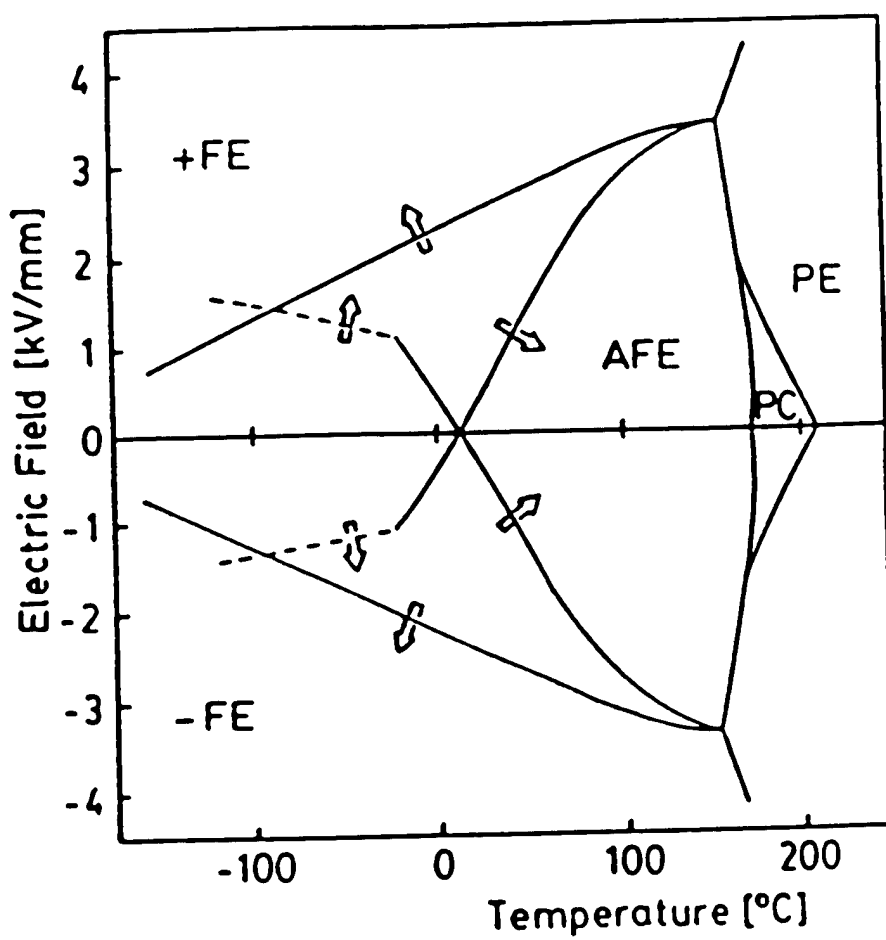


Figure 9. Phase diagram on the temperature-electric field plane for  $\text{Pb}_{0.99}\text{Nb}_{0.02}[(\text{Zr}_{0.6}\text{Sn}_{0.4})_{0.94}\text{Ti}_{0.06}]_{0.98}\text{O}_3$ .

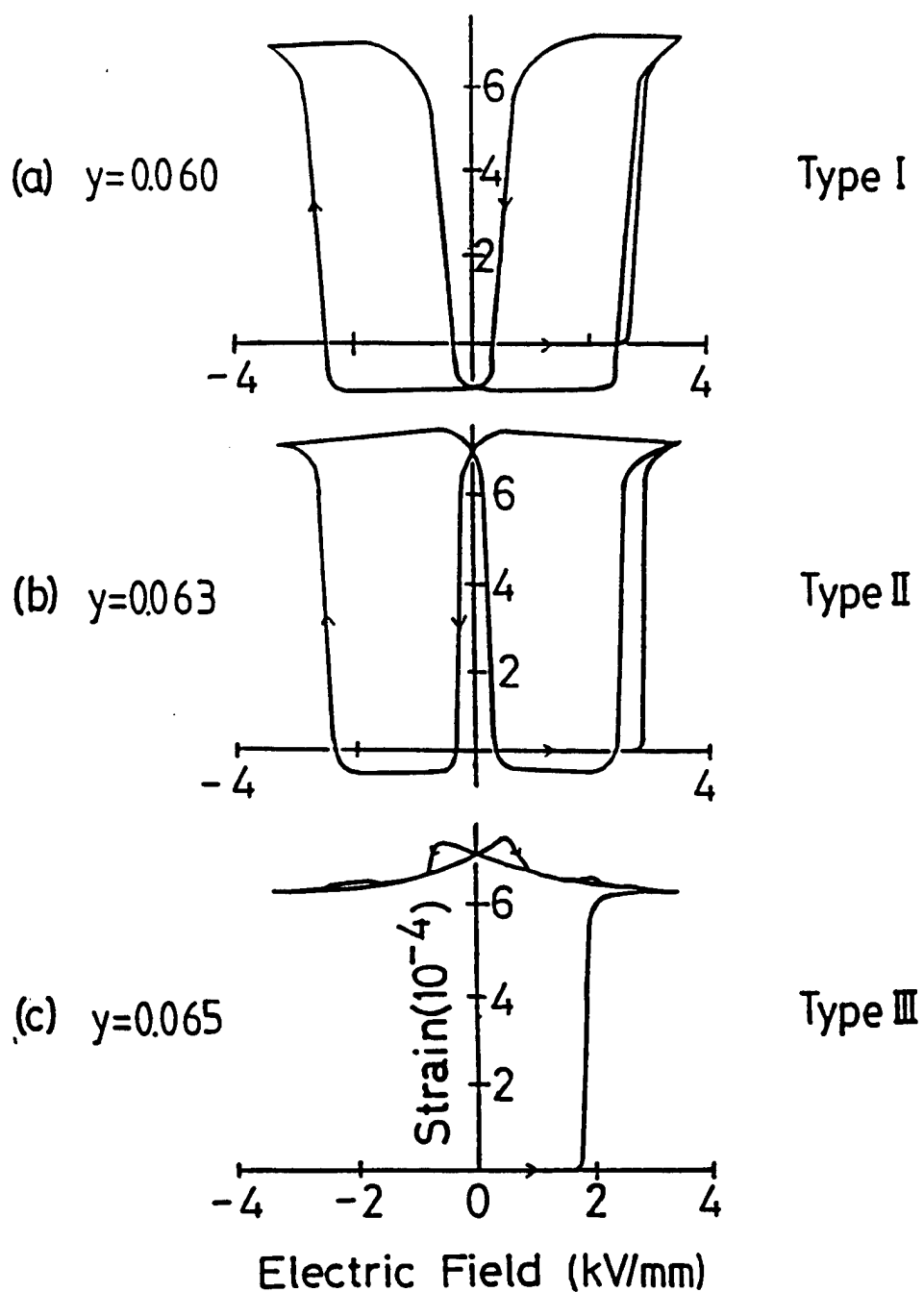


Figure 10. Transverse induced strains of  $\text{Pb}_{0.99}\text{Nb}_{0.02}[(\text{Zr}_{0.6}\text{Sn}_{0.4})_{1-y}\text{Ti}_y]_{0.98}\text{O}_3$  at room temperature: (a) for  $y = 0.06$ ; (b) for  $y = 0.063$ ; and (c) for  $y = 0.065$  [after Uchino (1985b)].



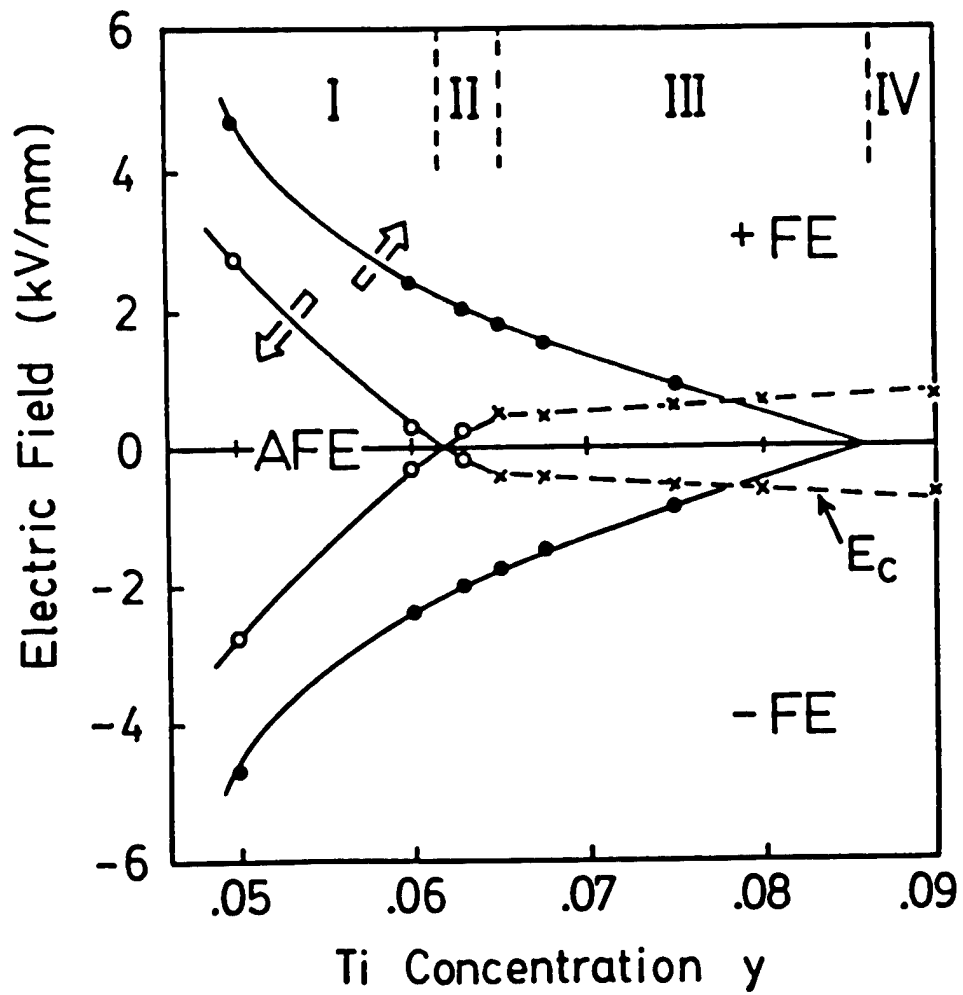


Figure 11. Phase diagram of  $\text{Pb}_{0.99}\text{Nb}_{0.02}[(\text{Zr}_{0.6}\text{Sn}_{0.4})_{1-y}\text{Ti}_y]_{0.98}\text{O}_3$  at room temperature with respect to the composition  $y$  and the applied electric field  $E$ .

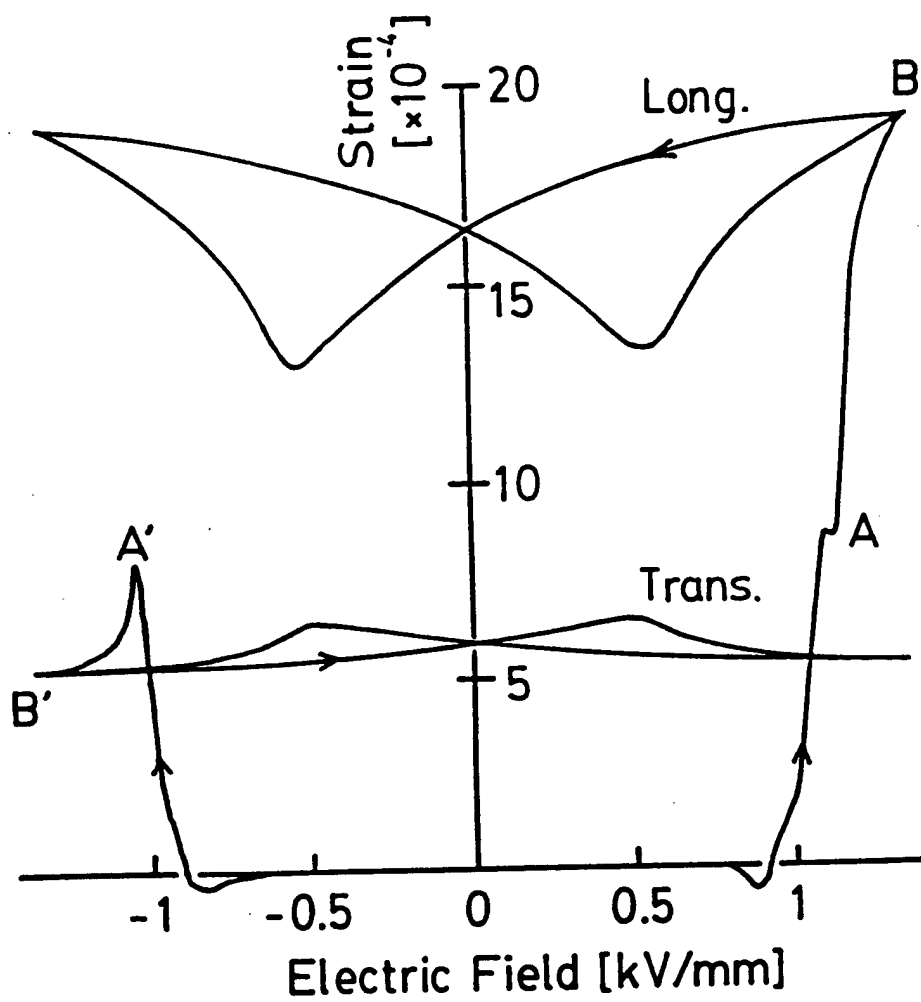


Figure 12. Longitudinal and transverse induced strains of the sample  $\text{Pb}_{0.99}\text{Nb}_{0.02}[(\text{Zr}_{0.6}\text{Sn}_{0.4})_{0.925}\text{Ti}_{0.075}]_{0.98}\text{O}_3$  [after Uchino (1985b)].

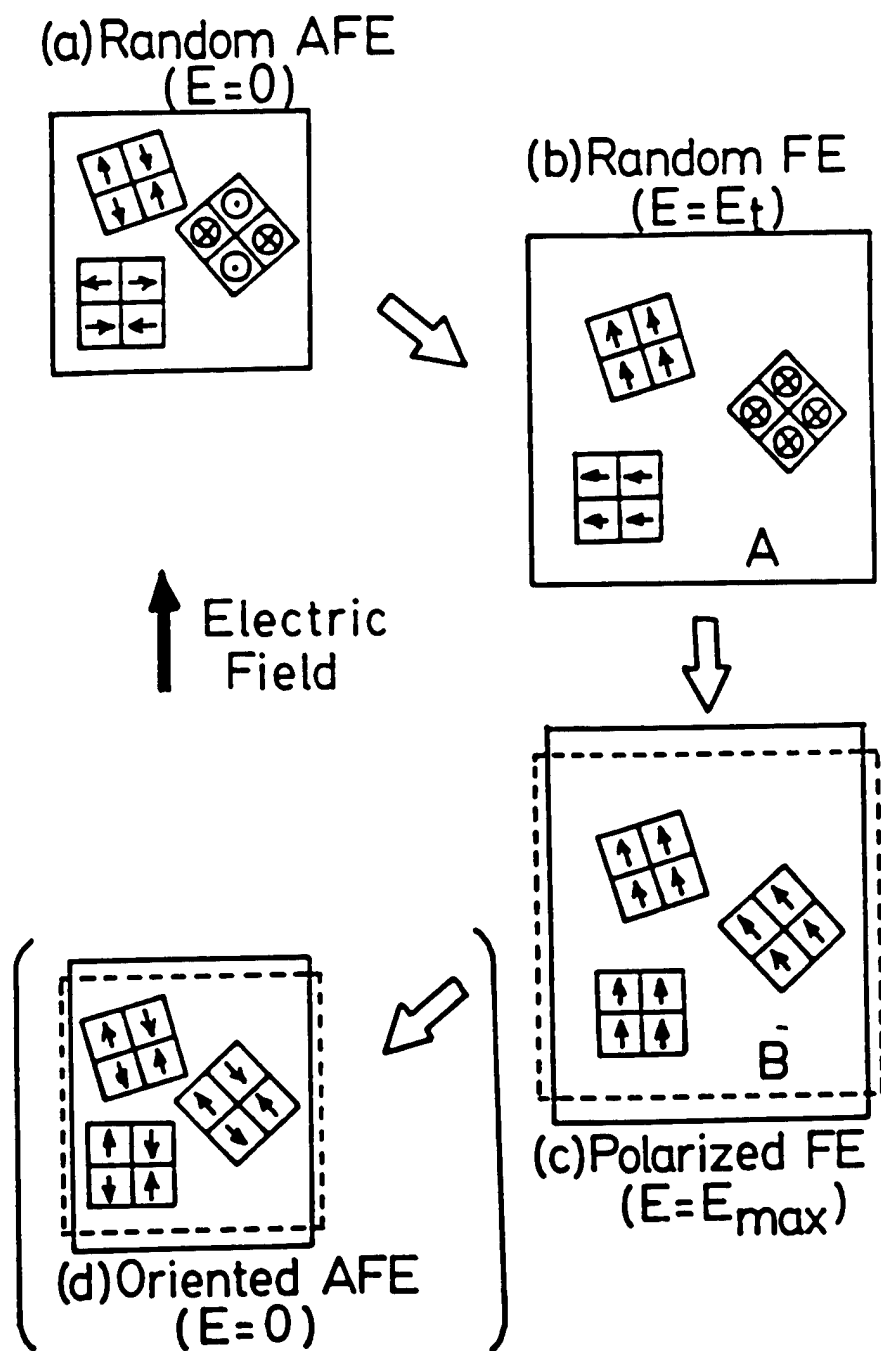


Figure 13. Schematic illustration of the antiferroelectric domain reorientation associated with the forced phase transition.

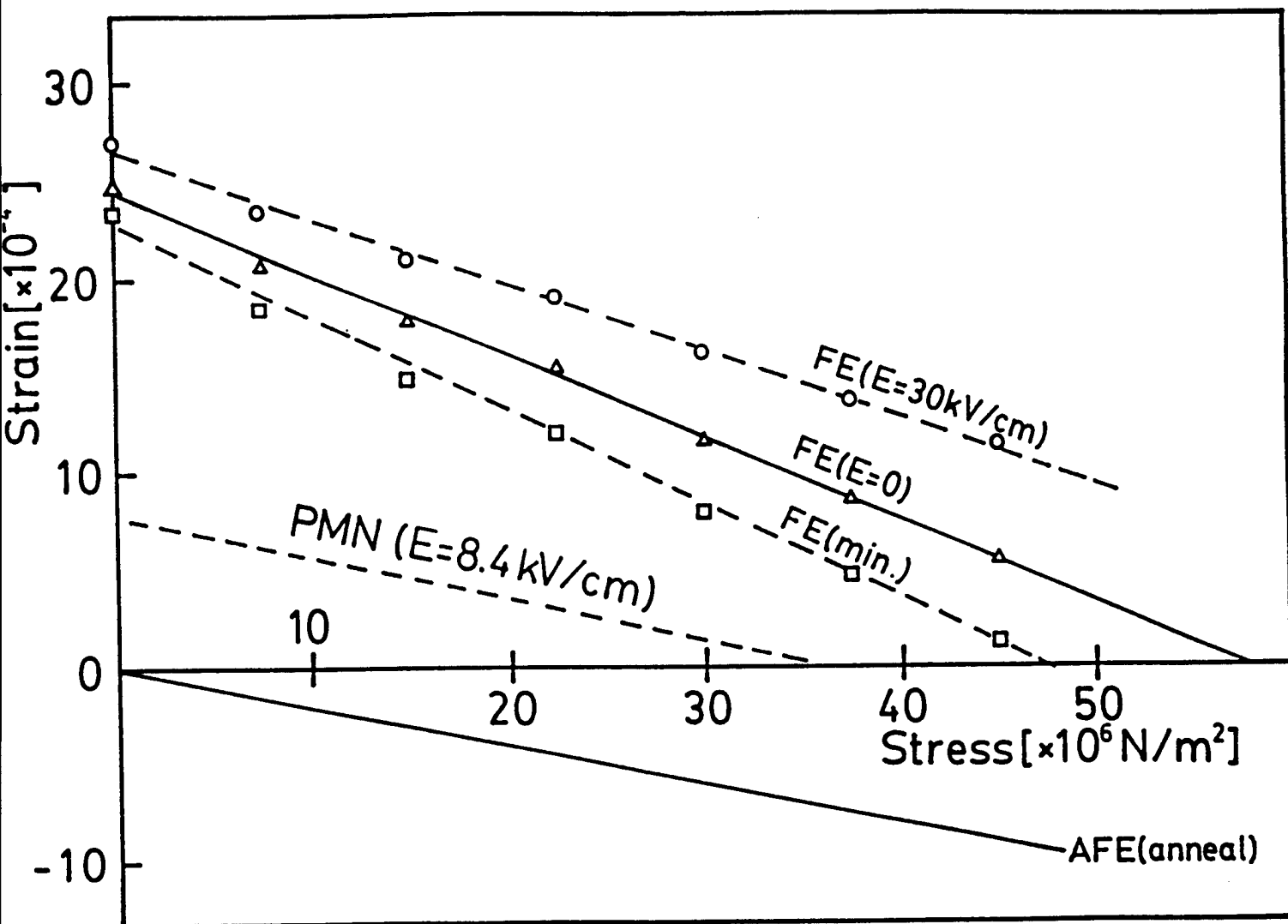


Figure 14. Longitudinal induced strains in a shape memory sample  $\text{Pb}_{0.99}\text{Nb}_{0.02}[(\text{Zr}_{0.6}\text{Sn}_{0.4})_{0.93}\text{Ti}_{0.07}]_{0.98}\text{O}_3$  at room temperature plotted as a function of uniaxial compressive stress [after Uchino (1989)].

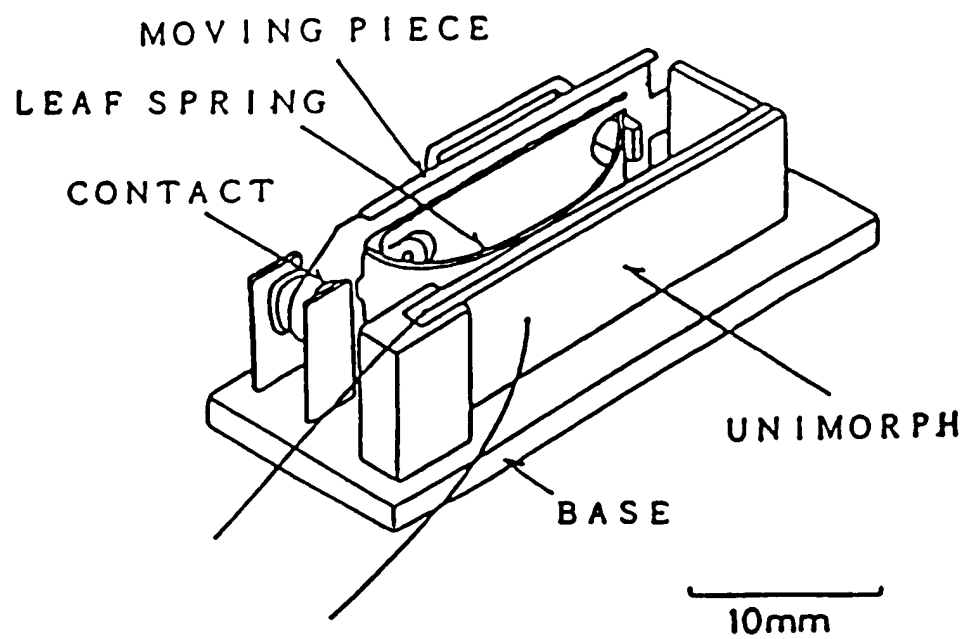


Figure 15. Structure of the latching relay using shape memory ceramic.

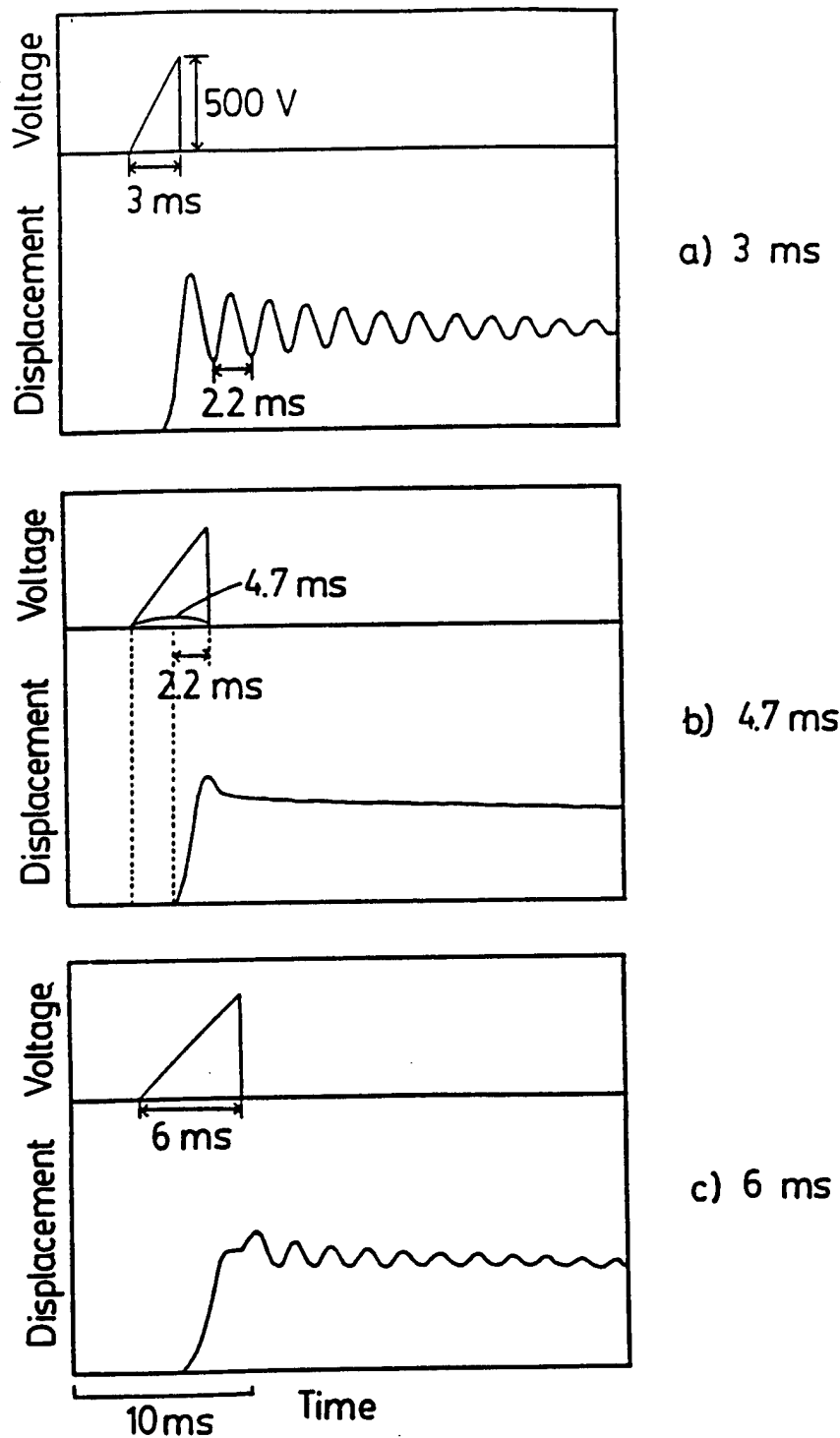


Figure 16. Dynamical response of the tip displacement of the shape memory unimorph with  $y = 0.063$  under various drive pulse conditions [after Furata, Oh and Uchino (1992)].

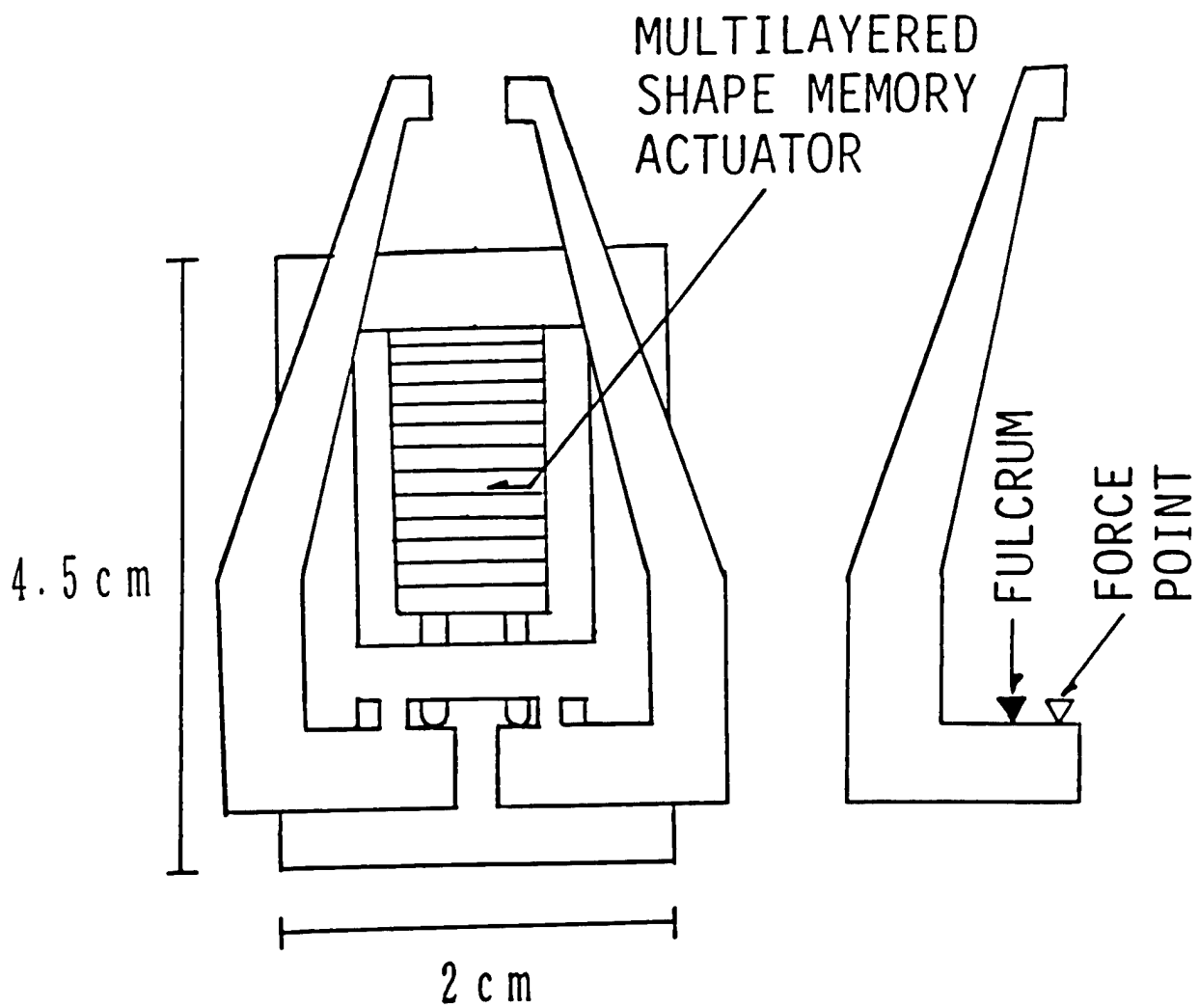


Figure 17. Construction of the mechanical clasper using a shape memory multilayer device.

# **APPENDIX 59**



## A Study of Acoustic Emission in Piezoelectric Multilayer Ceramic Actuator

Hideaki ABURATANI, Shoko YOSHIKAWA, Kenji UCHINO and J. W. C. de VRIES<sup>1</sup>

*International Center for Actuators and Transducers (ICAT), Intercollege Materials Research Laboratory,  
 The Pennsylvania State University, University Park, PA 16802, USA*

<sup>1</sup>*Ceramic Innovation Center, Philips Components B.V., Bredeweg 10 6042GG Roermond, The Netherlands*

(Received May 30, 1997; accepted for publication October 6, 1997)

Acoustic emission (AE) in multilayer ceramic actuators (MCA) has been studied. It was observed that AE signals could be concealed by sample's mechanical vibrations under usual MCA driving conditions. These vibrations were caused by an electrical coupling between the sample's piezoelectricity and the power supply's feedback. The AE was observed around the coercive field under bipolar driving. On the contrary, with unipolar driving, the AE was not present until the applied voltage reached a certain critical voltage. It was clarified that the AE generation in MCAs was strongly dependent on the maximum pre-applied stress (Kaiser effect), which corresponds to the applied voltage. The onset voltage of AE can be used to estimate the existing damages in the MCA. During the poling process, larger numbers of AE was observed in damaged MCA than that of un-damaged ones.

KEYWORDS: acoustic emission (AE), crack, delamination, multilayer ceramic actuator, piezoelectric ceramics, reliability

### 1. Introduction

Since multilayer ceramic actuators (MCAs) have high micro-displacement controllability and electromechanical coupling, they have been used in many applications, such as printer-heads and probe positioners in scanning tunneling microscopy (STM). As the application fields of the MCA expands, the higher reliability of MCAs is required. The insulation resistance,<sup>1)</sup> induced displacement<sup>2,3)</sup> and frequency response measurements<sup>4)</sup> have been employed for the fatigue/damage evaluations and to estimate the lifetime of MCAs. In the MCA with the interdigital electrode structure, a stress concentration caused by an electric field concentration at the end of internal electrodes is a major cracking source.<sup>5)</sup> The crack propagates to other electrodes and/or along the internal-electrodes (i.e., delamination).<sup>3)</sup> Hence, it is necessary to detect these types of cracking to avoid a collapse of the MCA and to determine the reliability.

The acoustic emission (AE) method, which measures acoustic emissions following an elastic energy release, is widely used for materials study as an non-destructive method.<sup>6)</sup> In our previous work, we discussed the AE generations caused by crack propagation in model-multilayer ceramic piezoelectric, electrostrictive and antiferroelectric actuators under bipolar electric field.<sup>2,3)</sup> This paper deals with the field induced AE generation in cofired piezoelectric MCAs under unipolar and bipolar field in addition to poling process. The AE in the damaged MCA is also discussed with a comparison of the AE in un-damaged ones. The possibility of using AE method to test the reliability of MCA is explored.

### 2. Experiments

The AE in MCAs with the interdigital electrode structure was investigated. It was clarified that a mechanical vibration of the piezoelectric sample was caused by an electrical coupling between a sample's piezoelectricity and a feedback from power supply.<sup>7)</sup> A change in external voltage from the power supply deforms the sample piezoelectrically and the electrical feedback started to couple with the induced electrical bias of the sample, resulting in a mechanical vibration. The frequency of this vibration was determined by both the power supply and the sample capacitance as well as sample dimen-

sions. The frequency of mechanical vibration was mostly found to be much lower than that of measured AE signals (>100 kHz). However, acoustic waves could be easily excited on the AE sensor by this vibration. These AE-like signals changed with the applied voltage due to the change in the vibration at various voltages, and was tend to be recognized as intrinsic AE signals mistakenly. It should be noted that any significant information can not be obtained from these extrinsic signals using the AE method, and this vibration level was large enough to conceal the intrinsic AE signals caused by phenomena took place in the sample. Thus, it is necessary to eliminate the sample vibration to perform the field induced AE measurement for piezoelectric materials. Since the vibration was caused by the feedback signal, increasing time constant of the voltage application system which lowers the amplitude of high frequency feedback signals was supposed to be effective to eliminate this vibration. A resistor was connected to the MCA in series to increase the time constant of the MCA-power supply voltage application system. The time constant  $\tau$  of voltage application system is given as following:

$$\tau = C_{MCA} \times (R_{\text{power supply}} + R_{\text{external}}) \quad (1)$$

where  $C_{MCA}$  is a capacitance of MCA,  $R_{\text{output impedance}}$  is output impedance of the power supply and  $R_{\text{external}}$  is the connected external resistance.

Thus the magnitude of high frequency components from the power supply were significantly reduced, resulting in a vibration level which did not affect the AE measurement.

Figure 1 shows the MCA sample specifications. The MCA is usually operated by a unipolar voltage from 0 to 60 V, which corresponds an electric field of 1.5 kV/mm, and exhibits an induced displacement of 1.6  $\mu\text{m}$ . Since a high local concentrated electric field around the ends of the internal electrodes is cannot be determined, the applied voltage rather than the electric field is preferred to be used in this paper. The samples were fabricated by a tape casting method using a soft piezoelectrics.

Figure 2 shows the AE measurement system. A 50 k $\Omega$  resistor, which introduced a time constant  $\tau \approx 18$  ms, was employed to remove the mechanical vibration. The resistance was chosen so as to introduce a time constant much shorter than the driving period (100 s=0.01 Hz), but much longer

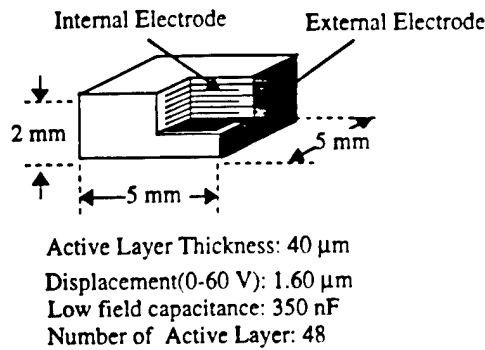


Fig. 1. The sample configuration

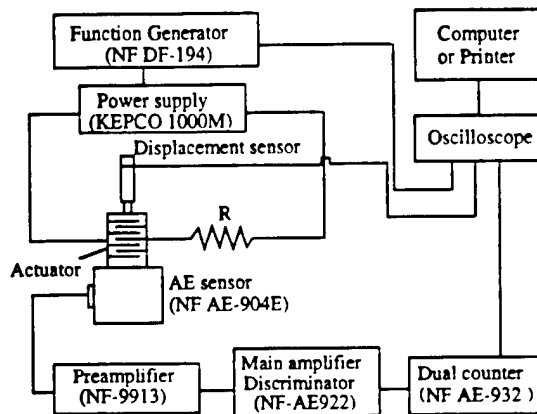


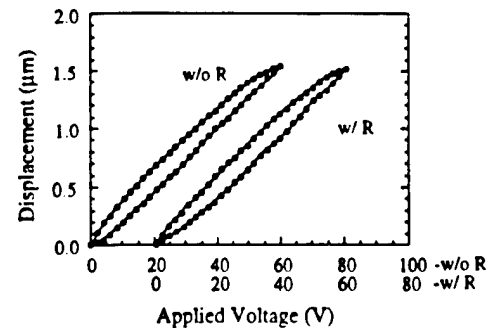
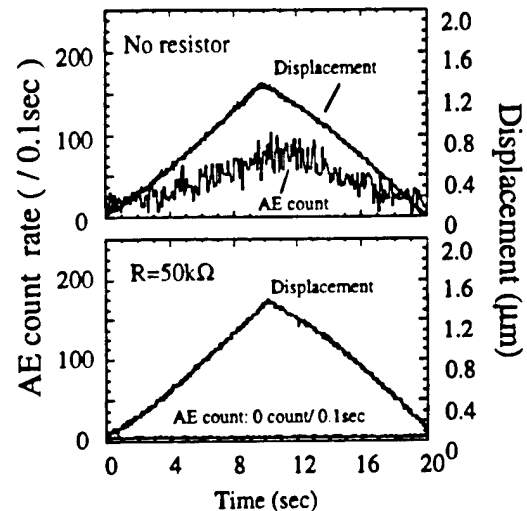
Fig. 2. The AE measurement system

than the period of the coupling vibration [ $\approx 1$  kHz ( $\approx 1$  ms)]. The total AE signal amplification was 100 dB and the signal threshold level was set to 400 mV for the AE measurements. Figure 3 shows the induced displacements of the MCA driven by a triangular wave with a peak value of 60 V at 0.01 Hz with and without the resistor, indicating that almost the same induced displacements were observed regardless of the resistor. Figure 4 shows the AE count rate with the total signal amplification of 40 dB and induced displacement as a function of time. When the resistor was not connected, a large value for the signal was counted as AE count, and the count rate increased with the applied voltage. These counted signals vanished completely when the resistor was used. It should be noted that this resistor does not cause any interference electrically with the AE monitoring circuit and intrinsic AE generations as long as the induced displacement is maintained. Thus, it is obvious that the AE count without the resistor was due to the mechanical vibration of the MCA. The results in §3 were taken with this resistor inserted in the drive circuitry.

### 3. Results and Discussions

#### 3.1 AE generation during the poling process

Figures 5(a) and 5(b) show the induced displacement of the MCA and the AE event count during the poling process. The poling voltage was applied at room temperature up to 120 V and 200 V, respectively. A very small value for the AE was observed when the MCA was poled with a peak voltage of

Fig. 3. The induced displacement with and without  $R = 50$  k $\Omega$ .Fig. 4. The AE count and the induced displacement as a function of time with and without  $R = 50$  k $\Omega$ .

120 V [Fig. 5(a)], although a large change in the displacement was observed around 40 V. Different from the previous results in lead zirconate titanate  $\text{Pb}(\text{Zr}, \text{Ti})\text{O}_3$  (PZT) single plate ceramics,<sup>7)</sup> the first deformation related AE at poling was not observed. It was assumed that AE signals in the MCA might be easily attenuated by the internal electrodes, because of the acoustic impedance mismatch. Moreover, the small surface area of the MCA attached to the AE sensor could lower the sensitivity of AE measurement. It was also supposed that even if the crack was formed during the poling process it must have stayed in the micro-crack region and slow growth speed, which was undetectable by the AE method.<sup>8)</sup> However, when a poling voltage with a peak of 150 V was applied, the AE event count rate started to increase around 140 V [Fig. 5(b)]. The AE was not observed around 40 V where induced displacement initiated and a large deformation of MCA was generated, but AE event rate increased with applied voltage, and continued even when the applied voltage was being decreased. The origins of the observed AE were supposed to be higher internal stress/strain at the higher applied voltage and consequential cracking. If this AE was only due to the stress/strain during the poling, the AE generation should have ended when the applied voltage decreased. The AE events

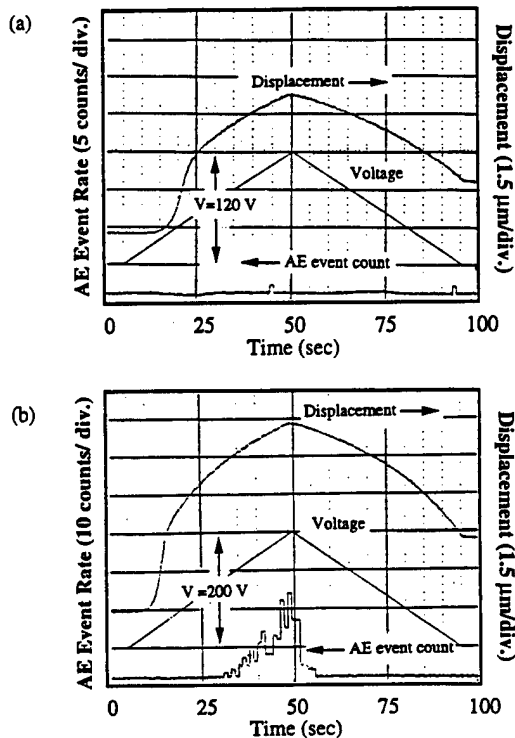


Fig. 5. The AE count and the induced displacement as a function of time during the poling process poling voltage=(a) 120 V and (b) 200 V.

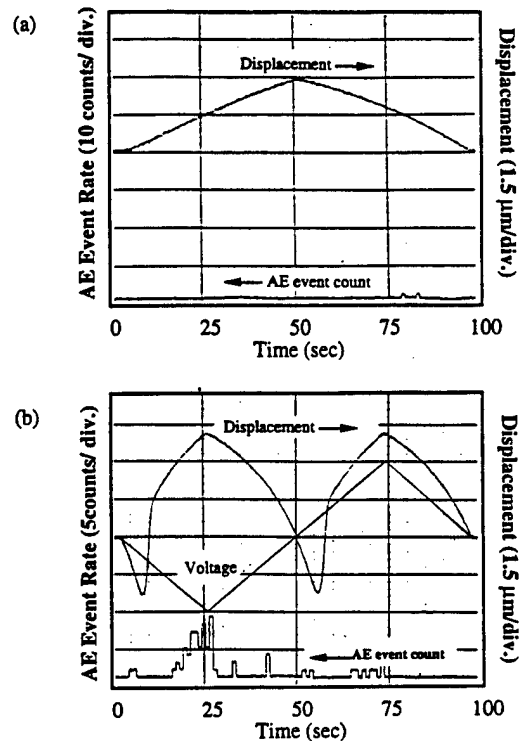


Fig. 6. The AE count and the induced displacement as a function of time under (a) unipolar drive and (b) bipolar drive.

during the applied voltage was being decreased, might indicate the damage of the MCA (i.e., crack and delamination). Therefore, the difference between the samples poled at 120 V and 200 V was probably due to the internal stress/strain and cracking in the MCA at higher poling voltage. This result indicated that possible cracking occurred in the MCA because of the electric field and stress concentrations for the applied voltage higher than 150 V. It is suggested that the critical poling voltage for the actuator, which does not cause any major cracking, can be determined using the AE measurement.

### 3.2 AE during unipolar and bipolar driving

Figures 6(a) and 6(b) show the induced displacement and the AE event count rate under unipolar and bipolar driving, respectively. Under unipolar driving, the sample was driven with the applied voltage from 0 to 120 V. The displacement switching was induced by a bipolar applied voltage  $\pm 180$  V. In order to increase the internal electric field constantly, a triangular wave at 0.01 Hz was employed. Under the unipolar driving, the AE event count rate was in a background level and no significant AE was observed [Fig. 6(a)]. However, under the bipolar driving, the AE was observed, particularly at the first application of the electric field through the displacement switching [Fig. 6(b)]. Since no repeatable signal—which was measured during the PZT single plate sample, was obtained, this AE is assumed to be caused by the cracking at the end of internal electrodes, where the electric field concentration occurs. Because the actual electric field at the end of internal electrode is higher than other parts, a small amount of AE was observed even before the coercive field (1 kV/mm=40 V) determined from the induced displacement. A large number

of the AE event was counted after the displacement switching until the maximum voltage. This AE might be also caused by the crack propagation along the internal electrodes (delamination). The volume and surface of the delaminations, with which the released elastic energy increased, were supposed to be more than those at the end of internal electrodes, resulting in much larger AE event count. A small number of the AE event, but higher than the natural background level, was observed throughout the measurement. This was probably due to friction at cracked and delaminated surfaces caused by the internal motions.

### 3.3 The Kaiser effect in the MCA

The Kaiser effect has a fundamental importance in the AE measurement.<sup>6)</sup> This effect states that once a material is stressed while the AE is being monitored, then the re-application of stress will not result in new emissions until it exceeds the initial maximum stress. This effect is not universal, but has been observed in various metals, ceramics and composites.

Figure 7 shows the AE count rate and induced displacement in an undamaged sample as a function of the applied voltage. The signal threshold level was set to 300 mV with the signal amplification of 100 dB. The sample was initially poled at 80 V. The AE counted during 120–140 V increment was plotted at the applied voltage of 140 V. During the first cycle, voltage was applied up to 120 V. AE counts of 60 were observed at 120 V. During the second cycle, AE counts of 20 were observed at 120 V, and 140 V was needed for AE to reach a 600-count. After this cycle, the voltage was reapplied up to 160 V. The AE count at 140 V decreased from 600 to

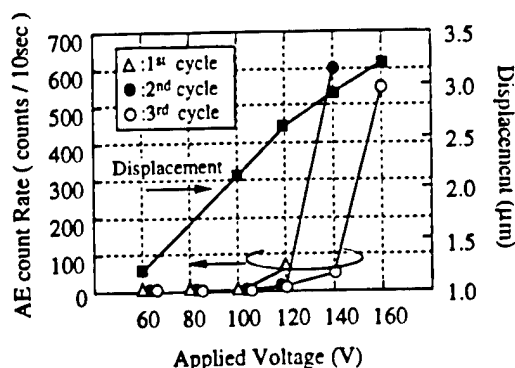


Fig. 7. The Kaiser effect in the MCA

40; although, the maximum emission rate was observed to be 560 at 160 V. However, it was supposed that major cracking took place above a voltage of 140 V in the sample. Since the MCA has stress and field concentrations at the end of the internal electrodes, it was assumed that those stress concentrated parts started to be cracked former than other parts.

Considering the stress increased with the applied voltage in the MCA, these pre-applied voltage dependence of AE generation was the Kaiser effect took place in the MCA. Although in this measurement, the detectable AE was started to be generated around a voltage level of 120 V, and the cracking was assumed to take place above 140 V. It seemed that a low AE signal level and the interdigital structure which have the stress concentrated parts made it difficult to separate the stress caused AE from the cracking AE in the MCA above 140 V.

### 3.4 The AE onset voltage in the damaged MCA

When materials are damaged, the re-applied stress, where new emissions start, becomes lower than the previous maximum stress (The Felicity effect).<sup>6)</sup> This decrease in the stress at the onset of AE can be caused by a friction between free and damaged surface. The Felicity ratio is defined as follows:

$$\text{Felicity ratio} = \sigma_{\text{stress at onset of AE}} / \sigma_{\text{previous maximum stress}} \quad (2)$$

Figure 8 shows the induced displacement and the AE event count rate for an unipolar cyclic test with a peak voltage value of 180 V. The samples were previously poled at 180 V. In the first cycle, a large number of AE event counts started to be observed from 160 V and could be caused by both stress and cracking [Fig. 8(a)]. The AE observed during the applied voltage was being decreased was probably due to the friction at the damaged and un-damaged surfaces (i.e., delamination). In the second cycle, the total AE event per cycle decreased. This was assumed to be the stress relaxation in the MCA due to cracking. A larger AE event rate than that of the first cycle was observed from 130 V to 160 V [Fig. 8(b)]. The portion of the AE event during the applied voltage which was being decreased became larger. At the 10th cycle, even the overall AE event count rate decreased, the AE onset voltage stayed around 130 V [Fig. 8(c)].

During the cyclic test, the total AE event count per cycle decreased with number of applied voltage cycle, but the AE onset voltage was found to be around 130 V. It was supposed that the damage in the MCA sample lowered the dura-

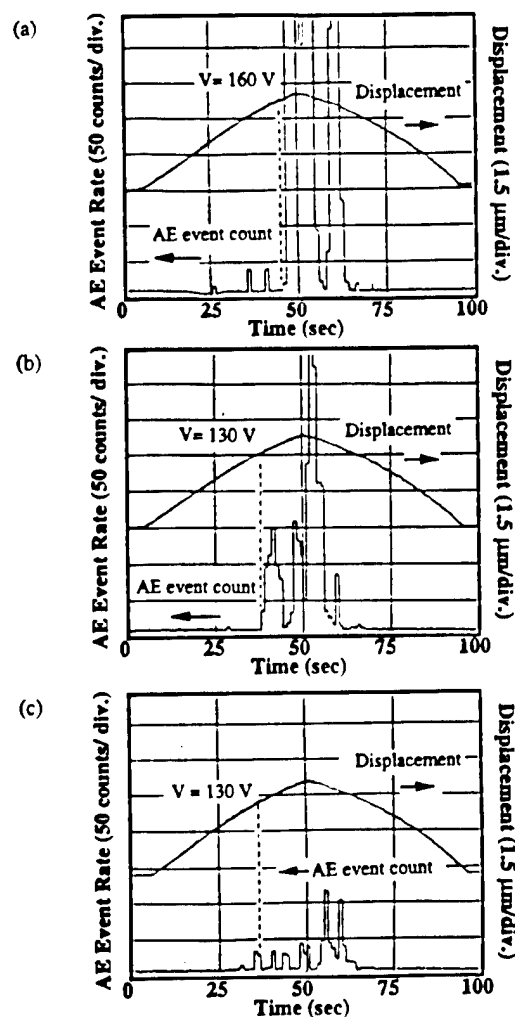


Fig. 8. The AE count and the induced displacement as a function of time: (a) 1st-cycle (b) 2nd-cycle and (c) 10th-cycle.

bility against applied voltage. This damage effect on the AE generation could indicate the Felicity effect in the MCA and the Felicity ratio was calculated to be  $130(\text{V})/180(\text{V})=0.72$ . The Felicity ratio in terms of the applied voltage can be used to evaluate the existing damages in the MCA and to determine the maximum safety driving voltage for the MCA which would not cause any major cracking.

### 3.5 AE generation in damaged MCA during the poling process

Figures 9(a) and 9(b) show the AE generation in damaged MCAs during the poling process. The samples were previously stressed by applying 30 V at 40°C with 95% RH for 3 weeks, and annealed to be de-poled above the Curie temperature. The re-poling voltage of 200 V was applied at room temperature. A large peak of AE event rate was detected around 40 V where the induced displacement started. It should be noted that this AE was not observed in the virgin samples [see Fig. 5(b)]. Since these MCA were once poled and stressed, it was assumed that the microcracks were formed in these MCA samples. Thus, the peak of AE was probably due to that the pre-introduced microcracks which gave a lower fracture

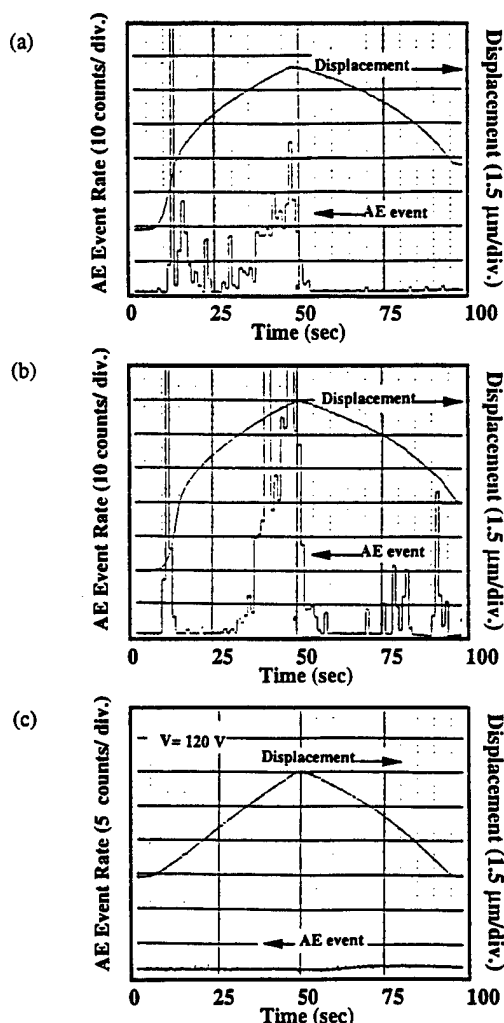


Fig. 9. The AE count and the induced displacement as a function of time from damaged sample during poling process: (a) damaged sample (1), (b) damaged sample (2), and (c) damaged sample (1) under unipolar drive with 120 V.

toughness extended rapidly when the strain and stress were introduced. The AE event rate increased with the applied voltage. The peak of AE event rate was also observed at lower voltage even while the applied voltage was being reduced in some samples [Fig. 9(b)]. This part of AE was probably due to the friction at the cracked and delaminated surfaces. After being poled, the sample was driven under the unipolar drive with a maximum voltage of 120 V. A much smaller AE event was observed [Fig. 9(c)]. This result implies that the cracking caused by the pre-introduced damage can be detected as an AE during poling; however, after MCA is poled, these cracks could not be a stable AE generation source under the unipolar driving. As mentioned in §3.4, it seemed that there was a critical voltage above which the measurable AE was generated in the damaged MCA. This was also assumed to be the stress relaxation in the MCA due to cracking. Figure 10 shows the photograph of the crack generated in the sample poled at 200 V. Since the crack was observed in the vicinity of the internal electrode end at an active layer next to the inac-

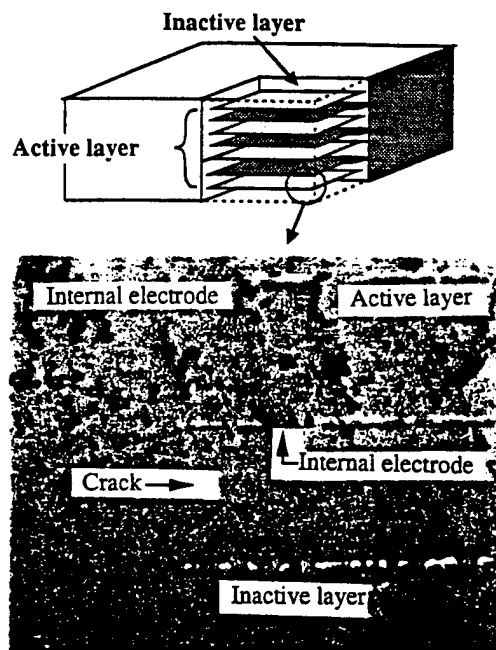


Fig. 10. The crack in the vicinity of the internal electrode end (poling voltage: 200 V).

tive one, the stress concentration caused by the inactive layer should be also considered to be the origin of the cracking. It was shown that the failures which can raise the destruction probability of the MCA could be detected during the poling process using the AE monitoring.

#### 4. Conclusions

The mechanical vibration of the MCA caused by the power supply was observed during the AE measurement. This vibration was large enough to conceal the true AE signals. By increasing the time constant  $\tau$  of the voltage application system, this vibration was eliminated completely.

A very small value for the AE was observed during the poling process, indicating no rapid cracking, when the applied voltage was lower than a certain critical voltage. Even if cracks were formed, they must have been too small to be detected as an AE. The attenuation of the AE signal by the internal electrodes and the size of MCA should be considered to determine the limitation of the AE measurement. The Kaiser effect and Felicity effect, in terms of the applied voltage, were observed in the MCA. The AE generation in the MCA was strongly dependent on the maximum pre-applied voltage. The AE onset voltage can be employed to estimate the damage. The AE measurement during the poling process could detect the cracking and the initial damage in the MCA. The field concentration at the end of internal electrode and stress concentration caused by the inactive layer should be considered to be the origin of the cracking.

It is concluded that the maximum applied voltage for the MCA, which would not cause major cracking can be determined using the AE method. The AE method can be also applied for crack propagation monitoring, damage evaluation and total design of the MCA devices.

# Acknowledgement

This work was supported by the Office of Naval Research through Contract No. N00014-92-J-1510.

- 1) K. Nagata and S. Kinoshita: *J. Jpn. Soc. Powder & Powder Metall.* **4** (1994) 975.
- 2) A. Furuta and K. Uchino: *J. Am. Ceram. Soc.* **76** (1993) 1615.

- 3) H. Aburatani, S. Harada, K. Uchino, A. Furuta and Y. Fuda: *Jpn. J. Appl. Phys.* **33** (1994) 3091.
- 4) B. Zickgraf, G. A. Schneider and F. Aldinger: *Proc. 9th IEEE Int. Symp. Application of Ferroelectrics* (1994) p. 325.
- 5) S. Takahashi, A. Ochiai, M. Yonezawa, T. Yano, T. Hamatsuki and I. Fukui: *Ferroelectrics* **50** (1983) 181.
- 6) R. Halmshaw: *Non-Destructive Testing* (Edward Arnold, London, 1991) 2nd ed., Chap 2, p. 273.
- 7) H. Aburatani and K. Uchino: *Jpn. J. Appl. Phys.* **35** (1996) L516.
- 8) A. G. Evans and M. Linzer: *J. Am. Ceram. Soc.* **56** (1973) 575.

# **APPENDIX 60**

# Acoustic Emission (AE) Measurement in Piezoelectric Ceramics

Hideaki Aburatani and Kenji Uchino  
International Center for Actuators and Transducers  
Materials Research Laboratory, The Pennsylvania State University  
University Park, PA 16802 USA

**Abstract**—A self vibration of piezoelectric ceramics caused by a power supply through a feedback system was observed during AE measurements. Significantly different results from previous reports were obtained by eliminating the self vibration of the ceramics. The AE generation in PZT was mostly caused by 180° domain reorientation.

## I. INTRODUCTION

Acoustic Emission (AE) method is a technique used to detect pulses of released elastic strain energy caused by deformation, crack growth and phase change in a solid.<sup>1)</sup> The AE method has been used to study phase transitions and ferroelectric domains; however, recent research has revealed a significant problem in most of the previous AE studies.<sup>2)</sup> A self-vibration of the sample was generated by the combination of the power supply through a feedback and the piezoelectric sample, and this concealed the true AE signal.

This paper deals with the AE measurement on the piezoelectric PZT ceramics along with a comparison of an antiferroelectric PNZST ceramics, and discusses the contribution of domain structure to the AE generation in piezoelectric ceramics.

## II. EXPERIMENTAL

Fig. 1 shows the measurement system. The field-induced AE and displacement were observed simultaneously. The AE signal was detected by an AE sensor (NF Corporation AE-904E) with its resonant frequency of 450 kHz. The AE signal was amplified by 40 dB through a preamplifier (NF, AE-922) and by 50 dB with a main amplifier (NF, AE-9913). The amplified signal was counted after passing through a high-pass filter (100 kHz) and a discriminator with lower and higher threshold levels of 300 mV and 600 mV, respectively. Disc specimens of piezoelectric PZT-5A and antiferroelectric:

$\text{Pb}_{0.99}\text{Nb}_{0.02}[(\text{Zr}_{0.55}\text{Sn}_{0.45})_{0.935}\text{Ti}_{0.065}]\text{O}_3$ , 12.7 mm in diameter and 0.3 mm in thickness, were employed for this study. Gold electrodes were sputtered on both surfaces. The AE sensor was attached to the sample through copper-foil and silicone grease. A modification to the AE measurement system was the introduction of an external resistor (R) in series and a capacitor (C) in parallel to the power supply in order to eliminate the high frequency component completely.

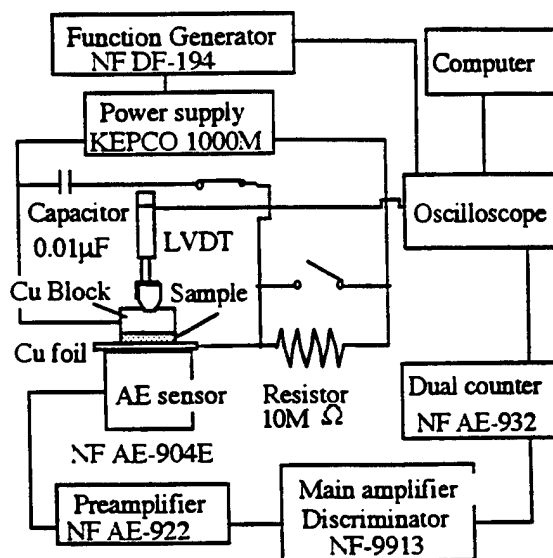


Fig. 1. AE measurement system

## III. RESULTS AND DISCUSSION

### A. Piezoelectric PZT

Fig. 2 shows the AE ringdown count in PZT during a poling process. A large number of the continuous AE count was observed even at 0 V/mm after poling without R and C, which corresponds to the conventional measuring setup. This count at 0 V/mm was caused by a high frequency component of voltage/current from the power supply through a feedback circuit, resulting in a vibration of the piezoelectric sample. In order to eliminate this vibration, both a resistor (R) of 10 MΩ and a capacitor (C) of 0.01 μF were connected to the sample to increase the time constant (RC) of the system (i.e., to suppress the high frequency component (Fig. 1)). The AE count at 0 V/mm vanished when R and C were connected to the sample, and completely different AE generation was observed in PZT. The AE was generated from the beginning of the induced displacement until the maximum applied field. This corresponds to the domain reorientation at the poling. On the contrary, no AE was observed when the applied field decreased, indicating a Kaiser effect in PZT.



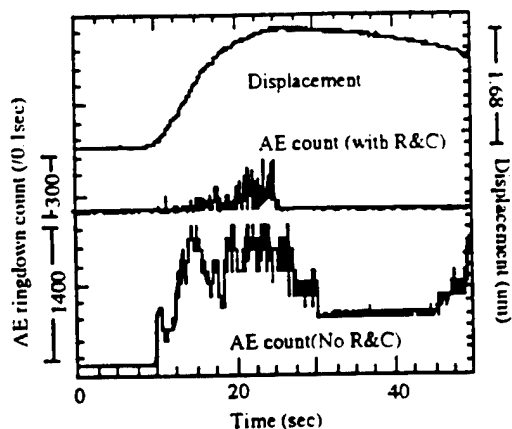


Fig. 2. AE ringdown count in PZT during a poling process

Fig. 3 shows the change in the induced displacement when R and C were connected. A large time constant in the whole system (0.1 sec) caused some distortion in the induced displacement curve; however, the displacement magnitude was maintained.

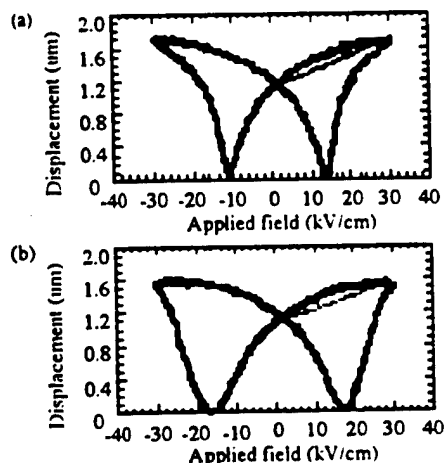


Fig. 3. Induced displacement of the PZT: (a) without R or C and (b) with R and C

Fig. 4 shows the AE count and the induced displacement as a function of time under a bipolar and an unipolar drive using the conventional setup (without R and C). The AE was continuously observed under bipolar drive, except for the displacement switching points. The AE was also detected under the unipolar field. These results indicate that the non-180° domain reorientation is a major AE generation source in ferroelectric PZT. Yet, in the system with R and C, the AE was observed only after the induced displacement switches under the bipolar drive, whereas no AE was observed under an unipolar drive (Fig. 5). Considering that the non-180° domain reorientation contributes mainly to the unipolar hysteresis and that both the 180°-domain and non-180° domain reorientations contribute to the bipolar switching, the results imply that the 180°-domain reorientation primarily generates the AE and that the

non-180° domain reorientation does not significantly affect the AE generation within PZT ceramics. It is probably due to the Kaiser effect that no AE was observed under the unipolar field after poling. If the AE generation in the conventional setup was really caused by the domain motion, the same AE generation should be observed in the modified setup as long as the induced displacement was maintained. Yet, the AE was observed only after polarization switching with a bipolar drive.

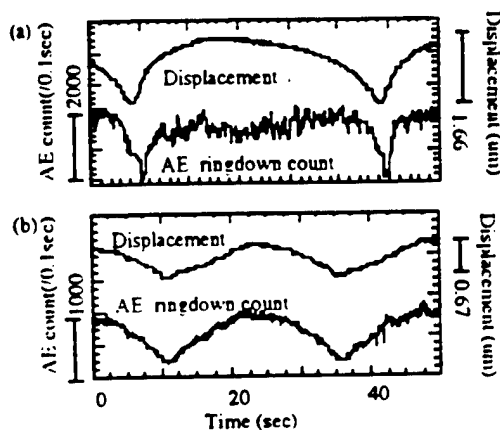


Fig. 4. AE count and induced displacement using the conventional setup: (a) under bipolar drive, (b) under unipolar drive at 85 dB

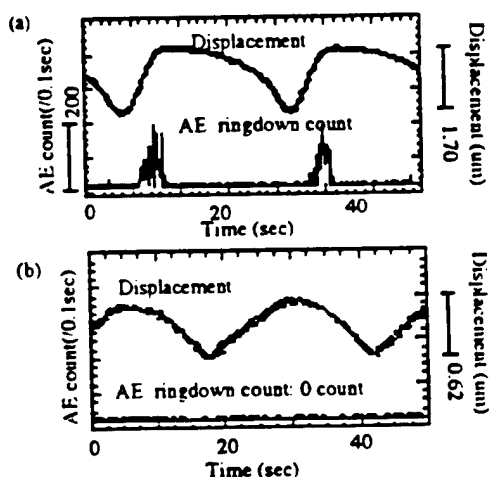


Fig. 5. AE count and induced displacement using the R&C: (a) under bipolar drive, (b) under unipolar drive

Thus, the AE generation in the conventional setup was not caused by the domain motion, but it was due to the sample vibration.

### B. Antiferroelectric PNZST

Fig. 6 shows the induced displacement of the antiferroelectric PNZST with and without R and C. No significant change in the induced displacement was observed even though R and C were connected to the system.

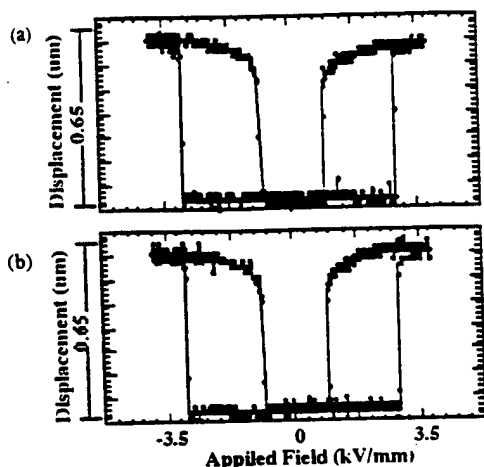


Fig. 6. The induced displacement of the antiferroelectric PNZST (a) without R and C (b) with R and C

Fig. 7 (a) shows the AE generation and the induced displacement in the antiferroelectric PNZST as a function of time under a bipolar drive using the conventional setup (without R and C). The AE was initially observed after the ferroelectric to antiferroelectric transition, and was continuously counted under the field induced ferroelectric phase. Yet, in the measurement system with R and C, the AE was observed only from after the antiferroelectric to ferroelectric phase transition and up to the maximum applied field (Fig. 7 (b)). This result indicated that the  $180^\circ$ -domain reorientation through the phase transition might be the primary AE generation source in the antiferroelectric PNZST: the vibration of the sample that was caused by the field-induced piezoelectricity combined with the feedback circuit was confirmed again. On the other hand, almost no AE generation was observed through the ferroelectric to antiferroelectric phase transition. This is probably due to the difference in the energy transfer from antiferroelectric to ferroelectric and ferroelectric to antiferroelectric state as well as domain structure change in those transitions.

#### IV. CONCLUSION

In the AE measurement of ferroelectric/ piezoelectric and antiferroelectric ceramics, the sample vibrations were observed. These vibrations were caused by the combination of the piezoelectricity and high frequency component from the power supply through the feedback. The magnitude of the vibration was large enough to conceal the true AE signals. Vibrations can be eliminated by increasing the time constant of the whole system.

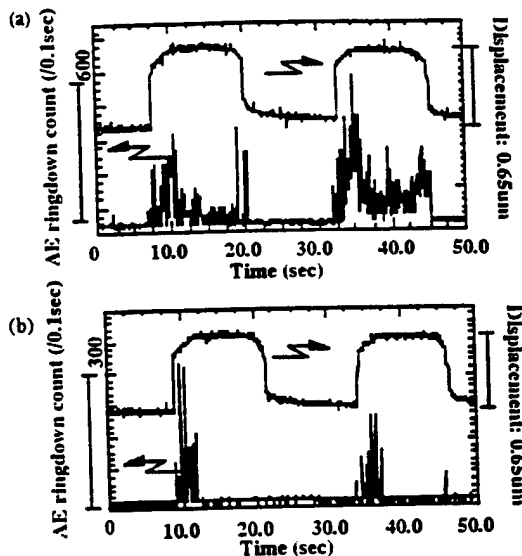


Fig. 7. (a) AE generation and the induced displacement in the antiferroelectric PNZST as a function of time under a bipolar drive using the conventional setup without R and C (b) with R and C

The AE was observed only through the field induced displacement switching in the ferroelectric/piezoelectric ceramics PZT. It is suggested that the  $180^\circ$ -domain reorientation contributes more to the AE generation than the non- $180^\circ$  domain reorientation in PZT ceramics. No AE was observed under the unipolar field due to the Kaiser effect in PZT after the poling process.

It was confirmed that the  $180^\circ$ -domain reorientation through the antiferroelectric to ferroelectric phase transition is the primary AE generation source in the antiferroelectric PNZST, while no AE was observed through the ferroelectric to antiferroelectric phase transition. This is probably due to the difference in the energy transfer of phase change as well as domain structure.

#### ACKNOWLEDGMENT

This work was supported by the Office of Naval Research through Contract No. N00014-92-J-1510.

#### REFERENCES

- [1] R. Halmshaw: *Non-Destructive Testing*, 2nd ed., Edward Arnold, London, 1991, pp. 273-286.
- [2] H. Aburatani and K. Uchino, "Acoustic emission (AE) measurement technique in piezoelectric ceramics," *Jpn. J. Appl. Phys.* 35 (1996) L516-518.

# **APPENDIX 61**

## THE APPLICATION OF ACOUSTIC EMISSION (AE) METHOD FOR FERROELECTRIC DEVICES AND MATERIALS

Hideaki Aburatani and Kenji Uchino  
International Center for Actuators and Transducers (ICAT)  
Materials Research Laboratory, The Pennsylvania State University  
University Park, PA 16802 USA

Field induced acoustic emissions (AE) in the ferroelectric PZT ceramics have been studied. The field induced AE was not observed after the poling was completed. The domain related Kaiser effect in terms of the applied field was observed. However, in damaged sample the Kaiser effect would not take place anymore (Felicity Effect). It has been demonstrated that the AE method can be used for the determination of the damage of material and safe driving electric field.

### I. INTRODUCTION

The contributions of domain structures for the field induced strain in the ferroelectrics have been studied by AE method. By eliminating the extrinsic AE signal caused by an electromechanical coupling between sample's piezoelectricity and feedback from power supply, it was confirmed that the field induced AE originated at the initiation of induced displacement and ended when the applied field was decreased during poling [1]. The AE was not observed after domain reorientation was completed at a given electric field except under bipolar field. Since new AE generation required larger electric fields than that applied during poling, the Kaiser effect[2] in terms of applied electric field was observed in the ferroelectric ceramics[1]. The damage of ferroelectric material at high electric field levels during the poling was also examined by AE method [3, 4]. However, intrinsic AE signals generated by domain reorientation as well as cracking and extrinsic AE signals caused by a coupling of piezoelectricity and feedback from power supply and bonding layer between sample and waveguide were not separated. AE generation in the damaged ceramics after poling has not been studied yet.

In stress induced AE, the Kaiser effect is not observed when any AE source can grow under a given condition (i.e. failure). The felicity effect is a breakdown of the Kaiser effect and is important for evaluating material damage[2]. In the stress induced AE, this effect

can be defined as a decrease of AE onset stress in the Kaiser effect. The decrease in the AE onset stress is caused by time-dependent effect controlled deformation (e.g. creep) in the material such as fiber-reinforced plastic composite (FRP) and a friction between free and damaged surfaces of crack. Therefore, the breakdown of the Kaiser effect is also expected in the damaged ferroelectrics ceramics under lower electric fields than poling electric field.

The paper deals with the AE generation in the damaged ferroelectric ceramics. The degree of damage of the thermally shocked single plate PZT ceramics was evaluated through the felicity effect with respect to electrically damaged and non-damaged sample. The feasibility of using the non-destructive AE method for the evaluation of damage in ferroelectric ceramics is demonstrated.

### II. EXPERIMENTAL PROCEDURE

The PZT 5A ceramics with silver electrodes fired on both surfaces were employed for this study. Thus, the damage on the interface between electrode and ceramics was also measured as a damage of sample. The size of sample was 12.7 mm in diameter and 0.4 mm in thickness. Thermal shock was employed to introduce the damage in this study. The samples were placed in an oil bath at 200 °C for 30 seconds, then in an oil bath at room temperature for 30 seconds under short circuit condition. This process was repeated for 10 cycles.

The induced displacement, frequency response and AE measurement were employed to evaluate the damage of sample in this study. Figure 1 shows the AE and induced displacement measurement system. The total amplification of AE signal and signal threshold were 90 dB and 400 mV, respectively. The natural background level was about 10 dB lower than the threshold level. Thus, the measured AE results did not contain any noise from the environment. The AE generations at various electric fields were also measured to observe the electric field dependence.

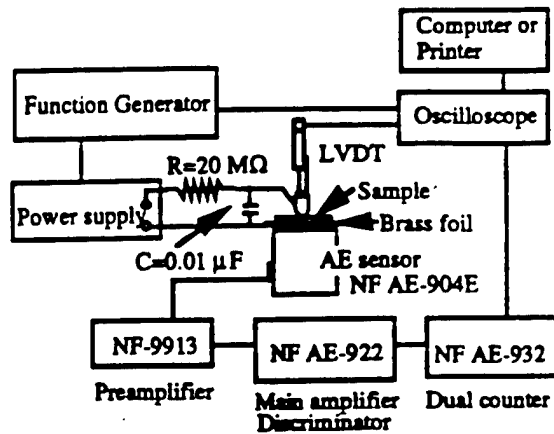


Figure 1. The AE and induced displacement measurement system.

### III. RESULTS AND DISCUSSIONS

#### A. Induced Displacement Measurement

The field induced displacement at the center of the disk in both non-shocked and thermally shocked PZT ceramics as a function of the applied field is shown in Figure 2. The applied field had a triangular wave form with a peak value of 37.5 kV/cm at a frequency of 0.01 Hz. The damage effects could be measured as a decrease in the displacement, since they might decrease the effective electric field in the sample and clamp the displacement. The results were obtained after 10 cycles of the electric field application.

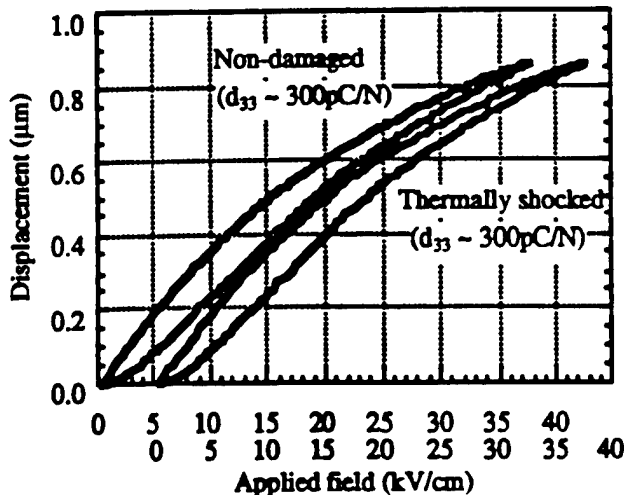


Figure 2. Induced displacement of non-shocked and thermally shocked PZT ceramics as a function of applied field.

There was no apparent difference in the induced displacement between non-shocked and thermally shocked samples. The obtained piezoelectric constants  $d_{33}$  were

almost identical. It seemed that even if the damage such as microcrack existed in the sample, it was too small to affect the displacement. The induced displacement also depends on the measuring point. To measure the effect of cracks, it is necessary to place the displacement sensor over or in the vicinity of the crack. From this measurement, only a local induced displacement property was obtained. It was not feasible to distinguish between the thermally shocked and non-shocked samples by this displacement measurement.

#### B. Frequency Response Measurement

When the piezoelectric sample is damaged, the properties of sample as a piezoelectric vibrator degrades and changes in the frequency response such as coupling factor and mechanical quality factor are expected[5]. The frequency response of both thermally shocked and non-shocked samples are plotted in Figures 3 (a) and (b).

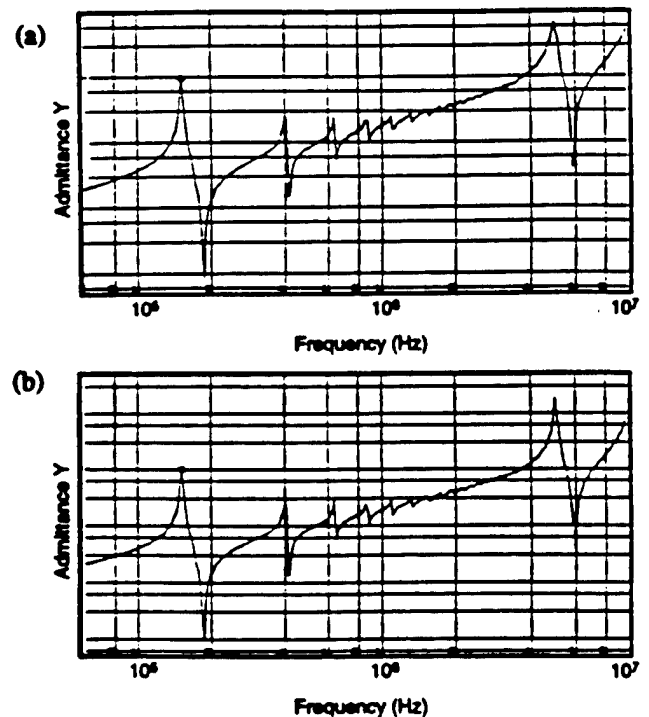


Figure 3. Admittance change as a function of frequency (a) non-shocked sample, and (b) thermally shocked sample.

Both the samples showed clear resonance and anti-resonance peaks. No spurious peaks were observed. The frequency at resonance and antiresonance were almost identical for all samples. The electromechanical coupling factor for the radial mode  $K_r$  and the mechanical quality factor  $Q_m$  of the non-shocked and thermally shocked samples were listed in table 1. The coupling factor  $K_r$  of 0.65 was obtained for both thermally shocked and

non-shocked samples. The mechanical quality factor  $Q_m$  of the thermally shocked sample was observed to be slightly lower than that of non-shocked sample.

Table 1. The coupling factor  $K_p$  and mechanical quality factor  $Q_m$  of non-shocked and thermally shocked PZT.

	$K_p$	$Q_m$
Non-shocked	0.65	78
Thermally shocked	0.65	75

### C. AE Measurements

The normalized total AE event count per cycle as a function of the number of field application cycle is shown in Figure 4. The AE event rate per cycle decreased markedly after poling with the electric field of 25 kV/cm. No AE was observed after the domain reorientation was completed. When an electric field of 37.5 kV/cm was applied to the non-shocked sample poled at 25 kV/cm, the AE event count simply decreased with the number of field application cycle. The observed AE event count after 10 cycles was higher than that of the sample exposed to an electric field of  $E=25$  kV/cm. It seemed that the domain reorientation was not completed due to high internal stresses present at higher field, resulting in more AE generations.

In a thermally shocked sample, the AE event count per cycle decreased until the 4th cycle, and started to fluctuate. This fluctuation in the AE count were observed in all of the thermally shocked sample. It was supposed that AE events in the thermally shocked samples originated from two sources: domain reorientation and damage caused by thermal shock. The domain reorientation related AE simply decreased with number of field application cycle. However, the AE caused by the damage (i.e., microcrack) was present throughout due to the internal motion and started to dominate in measurement after the level of the domain related AE tapered off.

The AE event rate and induced displacement of the non-shocked sample as a function of time are shown in Figure 5 (a). The AE generations of the non-shocked sample falls into two categories. A small number for the AE events was observed at first (Type I). The AE event rate then reached a maximum at the maximum field (Type II). The AE onset field and the AE event count rate at the maximum field are shown in Figure 5 (b). The AE event count rate at the maximum field decreased with number of field application cycle. However, the AE onset field did not change. The AE at the maximum field (Type II) was identified as the domain reorientation related AE, because of decrease in

AE count with the number driving cycles. If the AE observed at lower field (Type I) was related to the domain reorientation, it should decrease similarly with the number of cycle. Therefore, the AE observed at lower field (Type I) was due to electrically induced damage, since it did not change with the number of field application cycle. It was also supposed that the AE event count near 0 kV/cm was due to the electrically induced damage.

For the thermally shocked sample, AE was observed at lower field than that of the non-shocked sample as shown in Figure 6 (a). The samples became "noisy" in terms of the AE generation. This AE was most probably caused by the friction at the crack surfaces. The AE generation was observed even when the applied electric field was decreased to 25 kV/cm (Figure 6 (b)). After the displacement was induced, the AE events were also observed even when the applied field reached 0 kV/cm. This was probably due to the time dependent motion (stress relaxation near cracks) in the material. Since this AE was not observed in non-shocked samples exposed to an electric field of 25 kV/cm after poling, these AE events were obviously caused by the thermally induced damage.

The damage related AE event count was much less than that associated with domain reorientation. This can be understood as follows. During the poling the entire sample contributed to the AE generation. However, the damage related AE originated from the individual cracking regions and friction at the crack surfaces. Therefore, the damaged volume was much less than volume generating AE during poling, resulting in a small number of AE events. It was shown that the thermally induced damage and electrically induced damage in the sample were observed from the AE measurements.

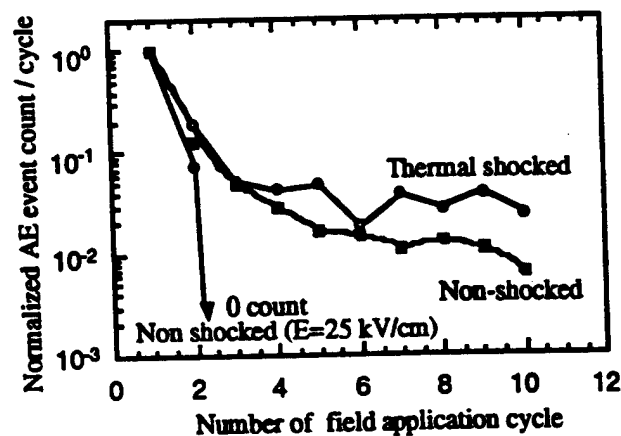


Figure 4. Normalized total AE event count per cycle as a function of the number of field application cycle.

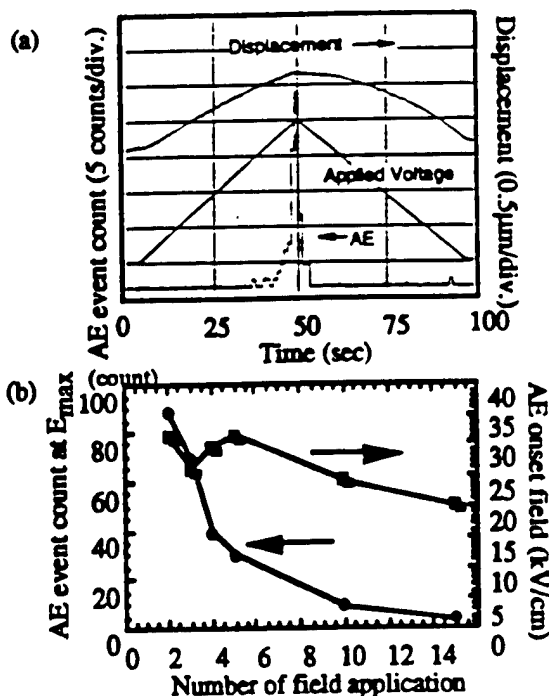


Figure 5. (a) AE event count rate and induced displacement of non-shocked sample as a function of time, and (b) AE onset field and AE event count at the maximum field of non-shocked sample as a function of the number of field application cycle.

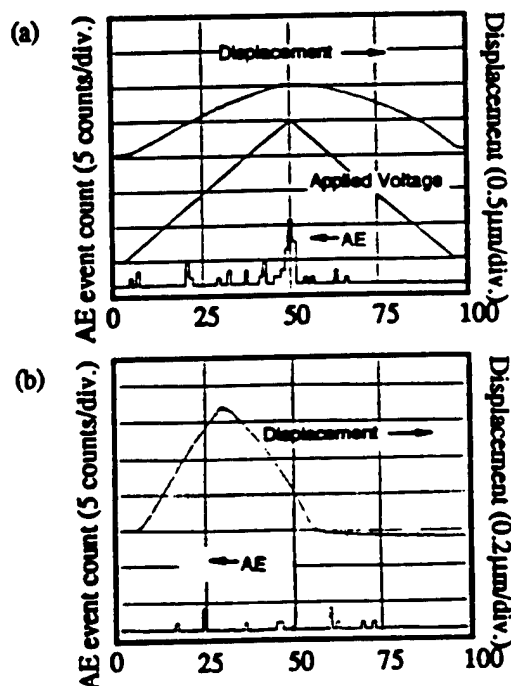


Figure 6. AE event count rate and induced displacement of thermally shocked sample as a function of time (a)  $E=37.5$  kV/cm, and (b)  $E=25$  kV/cm.

#### IV. Summary

The induced displacement, frequency response measurement and AE method were used for the damage evaluation of ferroelectric PZT ceramics under unipolar field. The thermally shocked and non-shocked sample exposed to an electric field of 37.5 kV/cm. Non-shocked samples were also examined at an electric field of 25 kV/cm. A small change in the mechanical quality factor  $Q_m$  was observed in the damaged sample. However, neither the induced displacement nor frequency response measurements obviously indicated damage in the samples.

On the contrary, the damage of the sample was clearly observed using the AE method in terms of breakdown of the Kaiser effect (felicity effect) and an AE generation at low electric field. The AE was observed even around 0 kV/cm in the thermally shocked sample. The friction generated through induced displacement and its relaxation at crack surface might be the source of AE. Moreover, it seemed that the electric field of 37.5 kV/cm was large enough to induce a damage even in the non-shocked samples. Damage related AE was also observed the non-shocked sample at this electric field level.

By measuring the AE, the damage in the samples was clarified. Damage occurring when a thermally shocked sample was at an electric field of 37.5 kV/cm was more than damage occurring when a non-shocked sample was subjected to an electric field of 37.5 kV alone. This in turn was more than the damage occurring at an electric field of 25 kV/cm.

These experiments show that the AE method can be extended to determine safe poling and driving field for piezoelectric ceramics and devices. This technique can be also used for evaluating the condition of the samples.

#### ACKNOWLEDGMENT

This work was supported by the Office of Naval Research through Contract No. N00014-92-J-1510.

#### REFERENCES

- [1] H. Aburatani and K. Uchino, "Acoustic Emission (AE) Measurement in piezoelectric ceramics," Proc. 10th IEEE Int. Symp. Appl. Ferroelectrics, pp. 871 (1996)
- [2] R. Halmshaw: *Non-Destructive Testing*, 2nd ed., (Edward Arnold, London, 1991) Chap 2 p.273
- [3] E. C. Subbarao, V. Srikanth, W. Cao and L. E. Cross "Domain Switching and Microcracking During Poling of Lead Zirconate Titanate Ceramics," *Ferroelectrics*, 145, pp. 271 (1993)
- [4] D. G. Choi and S. K. Choi, "Dynamic behavior of domains during poling by acoustic emission measurements in La-modified PbTiO<sub>3</sub> ferroelectric ceramics", *J. Mat. Sci.*, 32, 421 (1997)
- [5] T. Sakai, M. Ishikiriya and R. Shimazaki, "Durability of Piezoelectric Ceramics for Actuator," *Jpn. J. Appl. Phys.*, 31 (9B), pp. 3051 (1992)

# **APPENDIX 62**



# Reliability of Ceramic Actuators

Kenji Uchino

International Center for Actuators and Transducers  
Materials Research Laboratory, The Pennsylvania State University  
University Park, PA 16802 USA

**Abstract**—Reliability of ceramic actuators is dependent on complex factors, which are divided into three major categories: reliability of the ceramic material, reliability of the device design and drive technique. The reliability issues are reviewed from whole points of view, with a particular focus on multilayer structures.

## I. INTRODUCTION

The application field of ceramic actuators has become remarkably wide [1,2]. There still remain, however, problems in durability and reliability that need to be addressed before these devices can become general-purpose commercialized products. Investigations are primarily focused on the areas of ceramic preparation, device design and drive technique to improve the reliability.

## II. MATERIALS IMPROVEMENTS

The reproducibility of the strain characteristics depends strongly on grain size, porosity and impurity content. Increasing the grain size enhances the magnitude of the field-induced strain, but degrades the fracture toughness and increases the hysteresis [3]. The grain size should be optimized for each application. Hence, fine powders made from wet chemical processes such as coprecipitation and sol-gel will be required.

Porosity does not affect the strain behavior significantly. Figure 1 shows the tip deflection of a unimorph made from  $\text{Pb}(\text{Mg}_{1/3}\text{Nb}_{2/3})\text{O}_3$  based material plotted as a function of sample porosity [4]. The deflection did not show a difference below 8 % of porosity.

The impurity, donor- or acceptor-type, provides remarkable changes in strain. Figure 2 shows dopant effect on the field induced strain in  $(\text{Pb}_{0.73}\text{Ba}_{0.27})(\text{Zr}_{0.75}\text{Ti}_{0.25})\text{O}_3$  [5]. Since donor doping provides "soft" characteristics, the sample exhibits larger strains and less hysteresis when driven under a high electric field (1 kV/mm). On the contrary, the acceptor doping provides "hard" characteristics, leading to a very small hysteretic loss and a large

mechanical quality factor when driven under a small AC electric field (i. e. ultrasonic motor applications!).

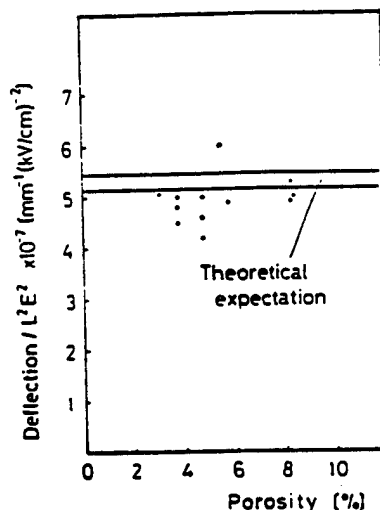


Fig.1. Tip deflection of a PMN unimorph plotted as a function of the sample porosity.

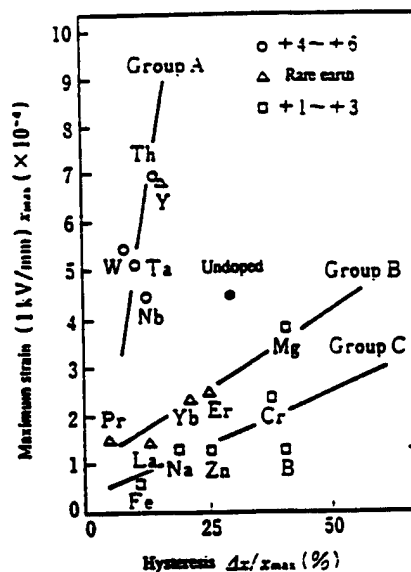


Fig.2. Dopant effect on the field induced strain in  $(\text{Pb}_{0.73}\text{Ba}_{0.27})(\text{Zr}_{0.75}\text{Ti}_{0.25})\text{O}_3$ .

Figure 3 shows the temperature rise versus vibration velocity for undoped, Nb-doped and Fe-doped  $\text{Pb}(\text{Zr,Ti})\text{O}_3$  samples. The suppression of heat generation is remarkable in the Fe-doped (acceptor-doped) ceramic [6].

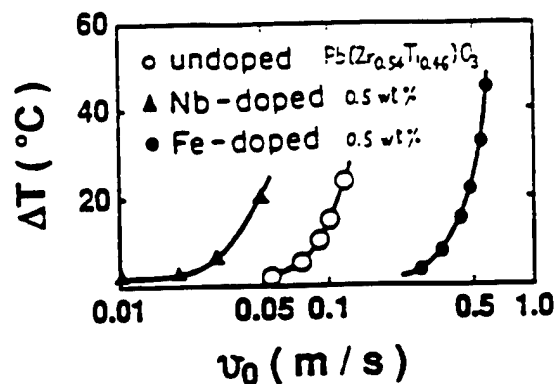


Fig.3. Temperature rise vs. effective vibration velocity for PZT samples doped with Nb or Fe.

The temperature dependence of the strain characteristics must be stabilized using either composite or solid solution techniques [7]. The recent new trends are found in developing high temperature actuators for engine surroundings and cryogenic actuators for laboratory equipment and space structures.

Ceramic actuators are recommended to be used under bias compressive stress. Figure 4 shows compressive uniaxial stress dependence of the weak-field piezoelectric constants  $d$  in various PZT. Note the significant enhancement in the  $d$  values for hard piezoelectric ceramics [8]. Systematic studies on stress dependence of induced strains are eagerly awaited, including the composition dependence of mechanical strength.

Although the aging effect is very important, not many investigations have been done so far. The aging effect arises from two factors: depoling and destruction. Creep and zero-point drift of the displacement are caused by the depoling of the ceramic. Another serious degradation of the strain is produced by a very high electric field under an elevated temperature, humidity and mechanical stress. Change in lifetime of a multilayer piezoelectric actuator with temperature and DC bias voltage has been reported by Nagata [9]. The lifetime under DC bias voltage obeys an empirical rule:

$$t_{DC} = A E^{-n} \exp(W_{DC}/kT) \quad (1)$$

where  $W_{DC}$  is an activation energy ranging from 0.99 - 1.04 eV.

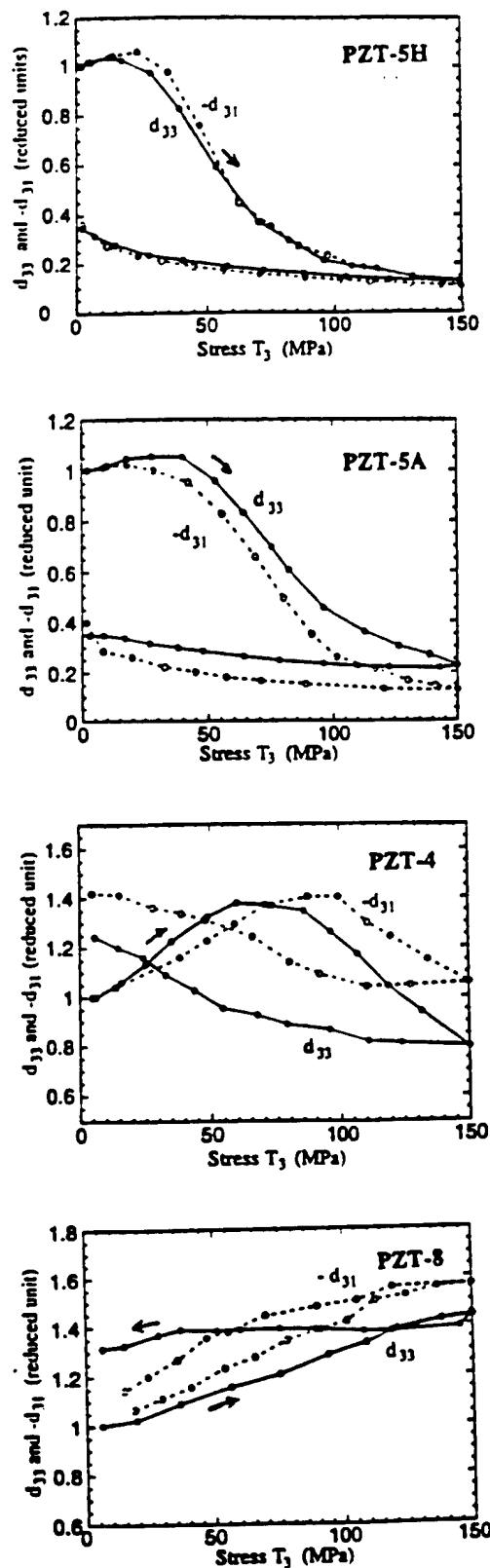


Fig.4. Compressive uniaxial stress dependence of the weak-field piezoelectric constant  $d$  in PZT (from top to bottom, "soft" to "hard").

### III. RELIABILITY OF DEVICES

Popular silver electrodes have a serious problem of migration under a high electric field and high humidity. This problem can be overcome with usage of a silver-palladium alloy (or more expensive Pt). To achieve inexpensive ceramic actuators, we need to introduce Cu or Ni electrodes, which requires a sintering temperature as low as 900°C. Low temperature sinterable actuator ceramics will be the next target to research.

Delamination of the electrode layer is another problem in multilayer types as well as bimorphs. To enhance adhesion, composite electrode materials with metal and ceramic powder colloid, ceramic electrodes, and electrode configurations with via holes are recommended for use [10]. To suppress the internal stress concentration which initiates the crack in the actuator device, several electrode configurations have been proposed, as shown in Fig.5: plate-through type, slit-insert type, and float-electrode-insert type [11]. The reason why the lifetime is extended with decreasing layer thickness has not yet been clarified.

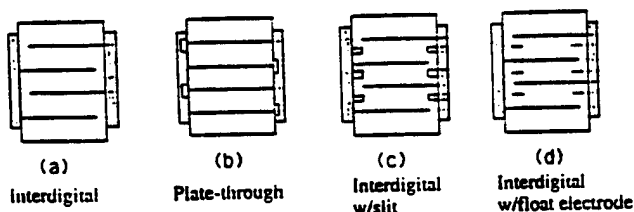


Fig.5. Various electrode configurations for multilayer ceramic actuators.

Lifetime prediction or health monitoring systems have been proposed using failure detection techniques [12]. Figure 6 shows such an "intelligent" actuator system with AE monitoring. The actuator is controlled by two feedback mechanisms: position feedback, which can compensate the position drift and the hysteresis, and breakdown detection feedback which can stop the actuator system safely without causing any serious damages to the work, e.g. in a lathe machine. Acoustic emission measurement of a piezo-actuator under a cyclic electric field is a good predictor for lifetime. AE was detected largely when a crack propagates in the ceramic actuator at the maximum speed. During a normal drive of a 100-layer piezoelectric actuator, the number of AE was counted and a drastic increase by three orders of magnitude was detected just before complete destruction. Note that part of the piezo-device can be utilized as an AE sensor.

A recent new electrode configuration with a strain gauge type (Fig.7) is another intriguing alternative for the health monitoring. By measuring the resistance of the strain gauge shaped electrode embedded in a ceramic actuator, we can monitor both electric-field induced strain and the symptom of cracks in the ceramic.

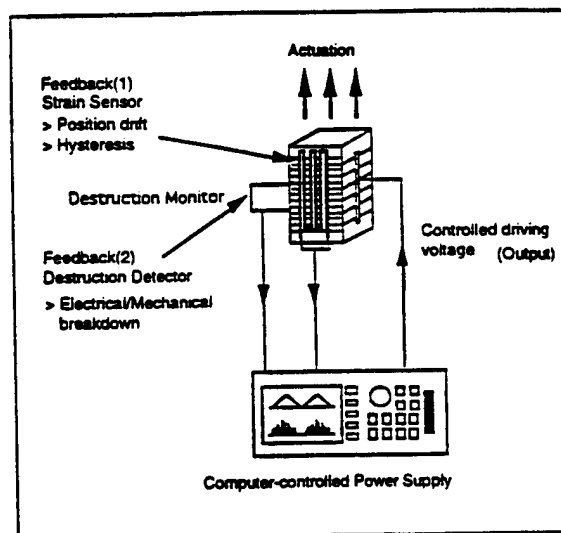


Fig.6. Intelligent actuator system with both position feedback and breakdown detection feedback mechanisms.

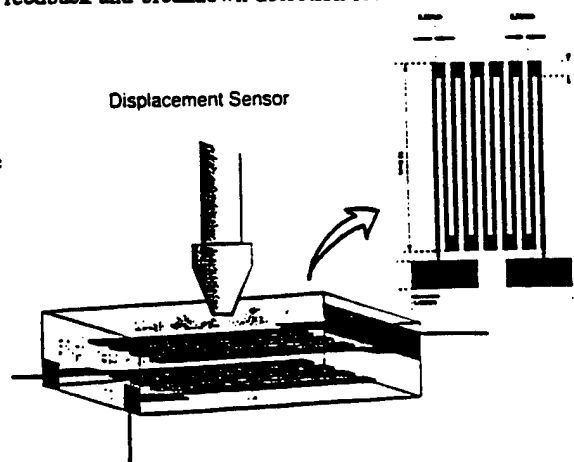


Fig.7. Multilayer ceramic actuator with a strain-gauge type electrode.

### IV. DRIVE TECHNIQUES

Pulse drive of the piezoelectric / electrostrictive actuator generates very large tensile stress in the device, sometimes large enough to initiate cracks. In such cases, compressive bias stress should be employed on the device through clamping mechanisms such as a helical spring and a plate spring.

Temperature rise is occasionally observed particularly when the actuator is driven cyclically, i.e. in pulse drive or ultrasonic motor applications.

Temperature rise is due to the imbalance between heat generation basically caused by dielectric hysteresis loss and the heat dissipation determined by the device size (surface area!) [13]. Figure 8 shows a linear relation between temperature rise and the  $v_e/A$  value, where  $v_e$  is the effective volume and  $A$  the surface area of a multilayer actuator, when driven at a fixed magnitude and frequency of the electric field. We need to select a suitable drive power or a driving duty ratio so as not to produce a temperature rise of more than 20°C.

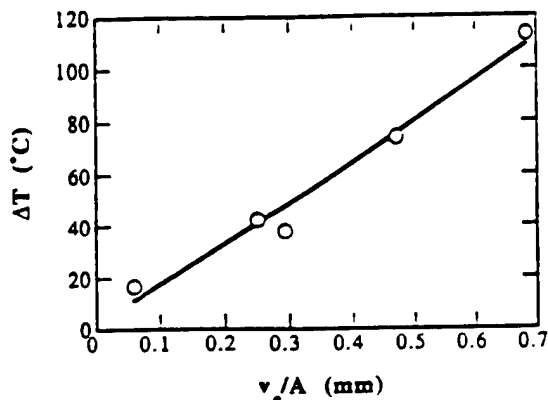


Fig.8. Temperature rise versus  $v_e/A$  for various size multilayer ceramic actuators (applied field: 3 kV/mm at 300Hz).

Regarding ultrasonic motors, the usage of the antiresonance mode has been proposed [14]. Quality factor  $Q$  and temperature rise have been investigated on a PZT ceramic rectangular bar, and the results for the fundamental resonance (A-type) and antiresonance (B-type) modes are illustrated in Fig.9 as a function of vibration velocity. It is recognized that  $Q_B$  is higher than  $Q_A$  over the whole vibration velocity range. In other words, the antiresonance mode can provide the same mechanical vibration level without generating heat.

All the previous ultrasonic motors have utilized the mechanical resonance mode at the so-called "resonance" frequency. However, the mechanical resonant mode at the "antiresonance" frequency reveals higher  $Q$  and efficiency than the "resonance" state. Moreover, the usage of "antiresonance," whose admittance is very low, requires low current and high voltage for driving, in contrast to high current and low voltage for the "resonance." This means that a conventional inexpensive power supply may be utilized for driving the ultrasonic motor.

## V. CONCLUSION

There are many possibilities to improve the durability and reliability of ceramic actuators. Future wide commercialization will be rather promising.

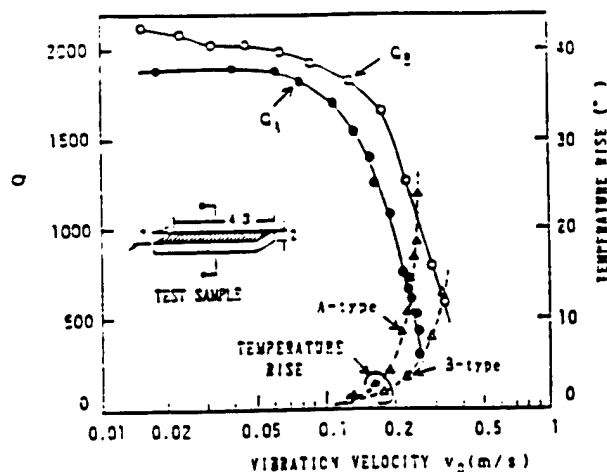


Fig.9. Vibration velocity dependence of the quality factor and temperature rise for both A- and B-type resonances of a PZT resonator.

## REFERENCES

- [1] K.Uchino, *Ceramic Actuators and Ultrasonic Motors*, Kluwer Academic Pub., 1996.
- [2] K.Uchino, "Ceramic Actuators: Principles and Applications," *MRS Bull.*, vol.18, p.42, 1993.
- [3] K.Uchino and T.Takasu, "Evaluation Method of Piezoelectric Ceramics from a Viewpoint of Grain Size," *Inspec.*, vol.10, p.29, 1986.
- [4] K.Abe, K.Uchino and S.Nomura, "The Electrostrictive Unimorph for Displacement Control," *Jpn. J. Appl. Phys.*, vol.21, p.L408, 1982.
- [5] A.Hagimura and K.Uchino, "Impurity Doping Effect on Electrostrictive Properties of  $(\text{Pb,Ba})(\text{Zr,Ti})\text{O}_3$ ," *Ferroelectrics*, vol.93, p.373, 1989.
- [6] S.Takahashi and S.Hirose, *Jpn. J. Appl. Phys.*, vol.32, Pt.1, p.2422, 1993.
- [7] K.Uchino, J.Kuwata, S.Nomura, L.E.Cross and R.E. Newham, "Interrelation of Electrostriction with Phase Transition Diffuseness," *Jpn. J. Appl. Phys.*, vol.20, Suppl.20-4, p.171, 1981.
- [8] Q.M.Zhang, J.Zhao, K.Uchino and J.Zheng, "Change of the Weak Field Properties of  $\text{Pb}(\text{Zr,Ti})\text{O}_3$  Piezoceramics with Compressive Uniaxial Stresses," *J. Mater. Res.* (submitted).
- [9] K.Nagata, "Lifetime of Multilayer Actuators," *Proc. 49th Solid State Actuator Study Committee, JTTAS, Tokyo*, 1995.
- [10] K.Abe, K.Uchino and S.Nomura, "Barium Titanate-Based Actuator with Ceramic Internal Electrodes," *Ferroelectrics*, vol.68, p.215, 1986.
- [11] H.Aburatani, K.Uchino, A.Furuta and Y.Fuda, "Destruction Mechanism and Destruction Detection Technique for Multilayer Ceramic Actuators," *Proc. 9th Int'l Symp. Appl. Ferroelectrics*, p.750, 1995.
- [12] K.Uchino and H.Aburatani, "Destruction Detection Techniques for Safety Piezoelectric Actuator Systems," *Proc. 2nd Int'l Conf. Intelligent Mater.*, p.1248, 1994.
- [13] J.Zheng, S.Takahashi, S.Yoshikawa, K.Uchino and J.W.C. de Vries, "Heat Generation in Multilayer Piezoelectric Actuators," *J. Amer. Ceram. Soc.* (in press).
- [14] S.Hirose, M.Aoyagi, Y.Tomikawa, S.Takahashi and K. Uchino, "High-Power Characteristics at Anti-resonance Frequency of Piezoelectric Transducers," *Proc. Ultrasonic Int'l.*, p.1, 1995.

# **Photostrictive Actuators**

# **APPENDIX 63**

script on Jan.12'98

# Mechanism of the bulk photovoltaic effect in ferroelectrics

Kazuhiko Tonooka <sup>a</sup>, Patcharin Poosanaas <sup>b</sup>, and Kenji Uchino <sup>b</sup>

<sup>a</sup> Hokkaido National Industrial Research Institute, Sapporo 062, Japan

<sup>b</sup> Materials Research Laboratory, The Pennsylvania State University, PA 16802

## ABSTRACT

The high-voltage bulk photovoltaic effect in ferroelectrics was theoretically and experimentally studied focusing on the nonlinear dielectric response. The steady current in the absence of applied voltage, called "photocurrent", is considered as a result of photocarriers and the asymmetric electromotive force induced by near-ultraviolet radiation. A model accounting for the generation of electric field acting as an effective *dc* field for the photocarriers was explained in terms of the photoinduced nonlinear polarization and the Lorentz field in dielectrics. Experimental results on electric photoconductivity, photocurrent and photovoltage of a PLZT ceramic were analyzed by using exponential functions based on the model. An adjustable parameter was introduced in relation to the incoherence of the illuminating light as an electromagnetic wave. It was found that the exponential functions by the present model can give better fitting to the experimental data than that by a linear function previously used.

**Keywords:** photovoltaic effect, ferroelectrics, optical nonlinearity, photocurrent, photovoltage, PLZT

## 1. INTRODUCTION

The bulk photovoltaic effect observed in ferroelectrics such as doped  $\text{LiNbO}_3$  crystals and PLZT ceramics are of considerable interest due to their high output voltage of the order of 1 kV/mm. Several devices utilizing the optically induced voltage of these ferroelectrics have been proposed.<sup>1-3)</sup> The photovoltaic effect in ferroelectrics is characterized by a generation of steady voltage under a short-wavelength illumination in the absence of applied field. Although there are many reports on the experimental results of the photovoltaic effect, the origin of the steady voltage and the steady current generated by the illumination is still unclear. The photovoltage in ferroelectrics is too high to be originated from difference in Fermi level of the materials and it is not likely to be a cumulate effect due to many *p-n* junctions in series. Photocurrents in  $\text{BaTiO}_3$  crystals were attributed to the internal fields due to space charge at the surfaces.<sup>4)</sup> A directional movement of photo-induced carrier in an asymmetric potential upon excitation was proposed for the origin of the photocurrent on Fe-doped  $\text{LiNbO}_3$  crystal.<sup>5)</sup> Generations of photo-induced carriers screening the internal field within the bulk of individual grains were proposed for the mechanism of the photovoltaic effect in poled ceramics.<sup>6)</sup> Many possible models have been presented for the mechanism of photovoltaic effect, however, no model gives any adequate explanation for it.

The generation of photocurrent in the absence of applied fields is considered due to the presence of photocarriers and an effective *dc* field induced by illumination. In this study, possibilities of generating effective *dc* field have been examined with respect to the nonlinear properties of the dielectrics. It was found that the nonlinear optical effect is a possible origin of the bulk photovoltaic effect in ferroelectrics having noncentric symmetry. Theoretical expressions for electric conductivity and current due to the photovoltaic effect were derived based on the

optical nonlinearity of the second order and on the Lorentz field, which gives an effective electric field caused by the polarizations in dielectrics. A good agreement was observed between experimental results on photovoltaic PLZT and the theoretical expectations.

## 2. OVERVIEW OF EXPERIMENTAL RESULTS

The current-voltage characteristics of photovoltaic ferroelectrics are usually measured on a rectangular slab with electrodes on opposing edges as shown in Fig.1. The sample was first poled by a static saturation field ( $\approx 2 \text{ kV/mm}$ ) at  $120^\circ \text{C}$ . The current to the external circuit depended on the applied poling voltage and the illumination intensity. An external voltage was applied so as to give a bias voltage. Figure 2 shows a typical current-voltage curve of a photovoltaic PLZT ceramic under a UV illumination by an ultra-high pressure mercury lamp. The details concerning the sample preparations were described elsewhere.<sup>7,8)</sup> Optical focusing lenses, a UV band-pass filter and an IR-cut filter were inserted between the lamp and the sample. The illumination intensity was at about  $4 \text{ mW/cm}^2$ . The light gave rise to a weak photovoltaic current simultaneously with the pyroelectric current. It was possible to distinguish between the two components of the total current produced by the light because of their different features. Upon exposure to UV irradiation, a pyroelectric current was initially observed, then a steady current was achieved. A linear dependence of the current on the applied voltage was observed for every intensity of illumination. The biased linear response in the current-voltage plot is a typical character of the photovoltaic effect produced by the illumination. This linear dependence suggested that an ohmic response and a photoinduced current were involved. The photoinduced current could remain constant for over the range  $-100 \text{ V}$  to  $+100 \text{ V}$  of the applied voltage, since it was small enough against the poling voltage ( $\approx 10 \text{ kV}$ ). Consequently, the current to the external circuit will be determined from the balance of the photoinduced current and the internal conduction current which depends on the applied voltage between electrodes. For an unpoled sample, the current was in the order of  $10^{-12} \text{ A}$ . The current depends also on remanent polarization, temperature, illumination wavelength, peaking at the vicinity of the band gap energy. The current is proportional to the sample width. The photocurrent is usually expressed in terms of the current per unit width, since only a very slight dependence on the thickness of the sample and on the electrode gap was observed. The photovoltage is usually defined as the open-circuit voltage determined from the linear extrapolation of the current-voltage relation as shown in Fig.2. The photovoltage is proportional to the electrode gap in the direction of polarization. A linear dependence of the photovoltage on the remanent polarization was reported in ferroelectric ceramics.<sup>9)</sup> Photocurrents and photovoltages are attributed to the presence of internal electric fields induced by short-wavelength illumination. The magnitudes of the short-circuit photocurrent and open-circuit photovoltage vary in different materials. The typical values for PLZT ceramics are  $1.5 \text{ nA/cm}$  and  $1.5 \text{ kV/cm}$  in solid solution ( $\text{Pb}_{0.97} \text{La}_{0.03} \text{Zr}_{0.52} \text{Ti}_{0.48} \text{O}_3$ ) [PLZT(3/52/48)] under  $4 \text{ mW/cm}^2$  illumination.

Consideration of the motion of the space charge in internal fields and polarizations of ferroelectrics is necessary to investigate the mechanism of the photovoltaic effects. The total polarization is usually separated into three parts: electronic, ionic, and dipolar contributions. The dielectric response at optical frequencies is determined by the electronic polarizability. The ionic and dipolar contributions are dominant at lower frequencies including *dc* electric field. Under the influence of a uniform polarization, the free charges move to the surface regions where the polarizations begin or end. According to a theorem of electrostatics, the macroscopic electric field caused by a uniform polarization  $P$  is equal to the electric field in vacuum of a fictitious surface charge density,



$$\sigma_s = n \cdot P, \dots\dots\dots (1)$$

where  $n$  is the unit vector normal to the surface. The net potential across the bulk is the sum of the potential due to the polarization and free charges. The free charges localized in the surface regions terminate the polarization. The electric field produced by the free charges at the surfaces is therefore directed oppositely to that by the polarization. Thus the free charges shield the internal electric field produced by the polarization. This shielding by free charges is related to the Debye screening effect. The Debye screening length is given by

$$\ell_D = \sqrt{\frac{\epsilon k T}{n_c q^2}}, \dots\dots\dots (2)$$

where  $\epsilon$  is the permittivity of the material,  $k$  Boltzmann constant,  $T$  temperature,  $n_c$  the carrier density, and  $q$  the charge of the carrier. A value of  $\ell_D \approx 10^{-7}$  m was estimated for a typical value of the photovoltaic effect in dielectrics under  $0.1 \text{ mW/cm}^2$  illumination.<sup>6)</sup> This distance is small enough to screen the electric field due to the spontaneous polarization within a typical  $10^{-5}$  m grain. Thus the static polarization of the bulk is screened by space charges when it is illuminated. If the carriers freed by the light become trapped so as to set up the space-charge field opposing the field due to the polarization, the photocurrent decays to zero in time. Therefore no contribution of static polarization in steady current generation is expected for the photovoltaic effect in poled ferroelectrics.

The main features of the photovoltaic effect in ferroelectrics are summarized as follows:

- 1) This effect is observed in a crystal or ceramic having noncentric symmetry.
- 2) A steady voltage and/or current is generated under uniform illumination.
- 3) The magnitude in the induced voltage is much greater than the band gap energy of the crystal.

The crystal asymmetry was expected to be the basic condition for the ferroelectrics to have photovoltaic effects. From a phenomenological point of view, presence of free carriers and a  $dc$  field inside the bulk is necessary to cause a steady current. Experimental data of electric conductivity indicates that free carriers are produced in ferroelectrics by short-wavelength excitation. Thus the generation of the electric field was our main concern. Many effects including pyroelectricity, piezoelectricity and optical nonlinearity were theoretically examined in relation to the asymmetric microstructure and the possibility of generating effective  $dc$  field under the UV illumination. It was found that an asymmetric polarization caused by the illumination can result in an effective  $dc$  field. Consequently, the optical nonlinearity of the second order was considered to be the most probable reason among these effects for the origin of the bulk photovoltaic effect.

## 2. MODELING

The photovoltaic properties are attributed to the photocarriers and internal electric fields caused by short-wavelength illumination. The optical nonlinearity of the second order was proposed as an origin generating photo-induced  $dc$  field. We begin with the following expression for the polarization of dielectrics, considering the non-linear effect up to the second order.

$$P = \epsilon_0 (\chi_1 E_{op} + \chi_2 E_{op}^2), \dots\dots\dots (3)$$

where  $\epsilon_0$  is the permittivity of vacuum,  $\chi_1$  the linear susceptibility,  $\chi_2$  the nonlinear susceptibility of the second order,  $E_{op}$  the electric field at an optical frequency. For ferroelectric ceramics, the nonlinearity is expected to appear as a result of the poling. The effect of the bias voltage to dielectric properties was considered to be negligible against

the poling voltage. Then the susceptibilities  $\chi_1$  and  $\chi_2$  were assumed to be constant as a first approximation. It is possible to treat the problem in a one dimensional configuration, because the photocurrents and the photovoltages were measured along the polar axis, as shown in Fig.1. Actually, no photocurrent was observed normal to the polar axis. In this study, we treated the illuminating light as an electromagnetic wave which gave an electric field for charges in dielectrics. When an alternating electric field with the amplitude  $E_{op}$  at an optical frequency  $\omega_{op}$  is applied to a dielectric material having nonlinear response, the polarization can be written as

$$P = \epsilon_0 \{ \chi_1 E_{op} \cos(\omega_{op} t) + \chi_2 E_{op}^2 \cos^2(\omega_{op} t) \} \quad , \dots \dots \dots (4)$$

where  $t$  is the time. In a linear material, which corresponds to the case of  $\chi_2=0$ , the induced polarization will be proportional to the applied electric field at any moment, resulting in a polarization oscillating at  $\omega_{op}$  as shown in Fig.3(a). Figure 3(b) shows the relation between the induced polarization and the given field in a nonlinear material. As a result of the nonlinear dielectric response, an asymmetric polarization wave is produced. The positive peak is greater than the negative one in this case. Thus the induced polarization contains both the fundamental wave and the higher order components. A Fourier analysis of the second-harmonic wave shows that it contains not only the second-harmonic component but also a non-zero average. This average term of the induced polarization can result in a dc electric field for carriers.

In dielectrics the value of the local electric field is different from the value of the macroscopic electric field. An additional field due to the polarization charges appears in polarized dielectrics. For simplicity, we approximated the local field in dielectrics by using the Lorentz relation calculated for the cubic symmetry,

$$E_{local} = E + \frac{P}{3\epsilon_0} \quad , \dots \dots \dots (5)$$

where  $E$  is the macroscopic electric field. When an alternating electric field at a optical frequency is applied, the local field in a dielectric material having second-order nonlinearity will be given by

$$E_{local} = E_{op} \cos(\omega_{op} t) + \frac{1}{3} \{ \chi_1 E_{op} \cos(\omega_{op} t) + \chi_2 E_{op}^2 \cos^2(\omega_{op} t) \} \quad , \dots \dots \dots (6)$$

Consequently one can obtain the average of the local electric field,

$$\overline{E_{local}} = \frac{1}{6} \chi_2 E_{op}^2 \quad , \dots \dots \dots (7)$$

It should be noted that the nonlinear polarization is produced by the nature of light as an electromagnetic wave and that equation (7) is derived for nonlinear dielectrics under a coherent propagation of a light wave at a single frequency. Moreover, this condition of coherent illumination may not be satisfied in a usual experiment where a mercury lamp is used as a light source. The nonlinear effect will be affected by the degree of coherence. Therefore we used the following expression for the effective *dc* field induced by incoherent light, considering the depression of nonlinear effect due to the incoherence,

$$\overline{E_{local}} = c_1 \chi_2 (E_{op}^2)^\gamma \quad , \dots \dots \dots (8)$$

where  $c_1$  is a constant,  $\gamma$  a parameter expressing the depression effect. After changing the variable  $E_{op}$  to its intensity  $I_{op}$ , one can obtain the expression for the average (*dc*) field induced by incoherent light,

$$E_{dc} = \overline{E_{local}} = c_2 \chi_2 I_{op}^\gamma \quad , \dots \dots \dots (9)$$

where  $c_2$  is a constant. This field is considered to be an effective  $dc$  field for photoinduced carriers (*i.e.* voltage source model).

Next consider the generation of photocarriers and their motions under the effective field. The concentration of carrier excited by optical irradiation will be governed by the rate equation,

$$\frac{d n_c}{d t} = g - R n_c^2 - \frac{n_c}{\tau_c} , \dots\dots\dots (10)$$

where  $n_c$  is the carrier density,  $g$  the generation rate of the carrier,  $R$  the recombination rate of the carrier, and  $\tau_c$  the intrinsic lifetime of the carrier. It is easy to find a solution for a steady-state. When the excitation is strong enough, the carrier density reaches

$$n_c = \sqrt{\frac{g}{R}} , \dots\dots\dots (11)$$

because the recombination process becomes dominant. The generation rate  $g$  is proportional to the light intensity  $I_{op}$ , thus the carrier density can be written as

$$n_c = c_3 \sqrt{\frac{I_{op}}{R}} , \dots\dots\dots (12)$$

where  $c_3$  is a constant. Introducing the carrier mobility  $\mu$ , the electric conductivity due to the photoinduced carriers is given by

$$\sigma_{op} = q n_c \mu , \dots\dots\dots (13)$$

where  $q$  is the charge of the photocarrier. Consequently the photoconductivity is obtained as a function of light intensity,

$$\sigma_{op} = c_3 q \mu \sqrt{\frac{I_{op}}{R}} , \dots\dots\dots (14)$$

The photocurrent will be the product of the photoconductivity and the photoinduced  $dc$  field, namely

$$J_p = \sigma_{op} E_{dc} , \dots\dots\dots (15)$$

Substituting equations (9) and (14) to (15), the expression for the photocurrent was obtained as

$$J_p = c_4 q \mu \chi_2 \sqrt{\frac{I}{R}} I_{op}^{1/2} , \dots\dots\dots (16)$$

where  $c_4$  is a constant. Equations (14) and (16) were derived theoretically for photovoltaic responses of ferroelectrics based on the optical nonlinearity.

### 3. ANALYSIS OF EXPERIMENTAL RESULTS

Experimental results on the photovoltaic response of non-doped PLZT were analyzed in terms of the nonlinear model proposed in the previous section. Figure 4 shows the photovoltaic current-voltage curves of a PLZT(3/52/48) sample illuminated with various UV intensities by a mercury lamp. A linear dependence of the induced current on the applied voltage was observed. Judging from this biased ohmic response, the photoinduced current seemed to be independent of the applied voltage in this range, whereas the internal conductive current depends on the

voltage between electrodes. The electric conductivity  $\sigma_{op}$  was calculated from the slope of the current-voltage curve and plotted in Fig.5. The dark conductivity was neglected in this discussion, because it was two order of magnitude smaller. The plot is in a logarithmic scale to find the probable exponent for the dependence on the light intensity  $I_{op}$ . The present model was examined by comparing the  $\sigma_{op}$ - $I_p$  response with the prediction based on eq.(14). The exponent for the photoconductivity on the dependence of light intensity was estimated to be 0.54, which was in a good agreement with the theoretical expectation derived by the recombination process of the carriers. Figure 6 shows the experimental results of (short-circuit) photocurrent  $J_p$  compared with the best fit line based on eq.(16) as a function of illumination intensity. Photocurrents were plotted in terms of the current per unit width. The parameter  $\gamma$  of eq.(16) was estimated to be 0.46 by the exponential fit to the experimental data, indicating that the effective  $dc$  field was proportional to  $(I_{op})^{0.46}$ . The parameter  $\gamma$  should be between 0 and 1, according to the treatments deriving eq.(16). A depression in  $\gamma$  value may be resulted from the incoherence of the illumination light by a mercury lamp. Figure 7 shows the experimental results of (open-circuit) photovoltage  $V_p$  and the best fit line by an exponential fit similar to eq.(16). It seemed that the photovoltage was proportional to the square root of the light intensity.

A further analysis of experimental data was made in relation to the depression effect due to the illumination incoherence. The coherence can be classified into spatial and temporal ones. Since a partial coherence of illuminating light will be achieved in a very small area, an increase in  $\gamma$  value was expected for a thinner photovoltaic material. The photocurrent for a thin PLZT sample with the thickness of 140  $\mu m$  was measured as a function of light intensity. Figure 8 shows the experimental results of photocurrent and the fitted line based on eq.(16). The exponential fit to the experimental data gave  $\gamma = 0.8$  as the best fit value. Comparing with the previous result  $\gamma = 0.46$  obtained for a thicker sample, an increase in the parameter  $\gamma$  was observed for a thinner photovoltaic sample. Thus the present model was supported by the experimental data of photoconductivity and photocurrent.

#### 4. CONCLUSIONS

The bulk photovoltaic effect in ferroelectrics was examined with respect to the properties resulted from the optical nonlinearity. The generations of photoexcited carriers and the effective  $dc$  field by the nonlinearity under the UV illumination were found to be a probable mechanism for the photocurrent and the photovoltage. This effective  $dc$  field was calculated based on the nonlinear polarization and on the Lorentz field in dielectrics. Theoretical expressions for the photoconductivity and the photocurrent were derived as functions of light intensity, carrier mobility, carrier recombination rate and the nonlinear susceptibility of the material. The experimental results of photovoltaic current-voltage data for PLZT ceramics were analyzed in terms of the electric conductivity and the effective field induced by light. The square root law expected for the photoconductivity in the dependence on the illumination intensity was supported by the experimental results for PLZT ceramics, suggesting that the carrier recombination is dominant in the relaxation processes of photocarriers. A parameter  $\gamma$  was introduced to explain the depression of the nonlinear effect due to the incoherence of illuminating condition. For a thick photovoltaic PLZT, the parameter  $\gamma$  was estimated to be 0.46, which implies that the magnitude of the effective  $dc$  field is proportional to the square root of the illumination intensity. For a thinner sample, another value of  $\gamma = 0.8$  was obtained as a best fit value. This increase in  $\gamma$  value for a thinner sample was considered to be due to the reduction of spatial incoherence of the illumination. An enhancement in the photovoltaic properties may be achieved for a very thin sample or by a coherent illumination. It was first shown that the experimental data, namely the photoconductivity, the photocurrent and the photovoltage as a function of the light intensity, were better fitted by the exponential functions proposed in this report than that by linear

functions previously used. A plasma effect may also be involved in the motion of the charge carrying the photovoltaic effect in ferroelectrics under a strong illumination. Linear functions could explain the response for a particular condition. However, the nonlinear treatment will be required to obtain better fits to experimental results for over a wider range of experimental conditions. Measurements of the carrier density and the electric field caused by the incident light seem to be necessary in order to understand the microscopic mechanism of the photovoltaic effect. The current to the external circuit is determined by the balance of the photocurrent and the internal conduction current. An extension of the model is under way to find the expression for photovoltage and current-voltage characteristics in photovoltaic ferroelectrics.

## 5. REFERENCES

1. A.M.Glass D. von der Linde, D.H. Auston and T.J. Negran, "Excited state polarization, bulk photovoltaic effect and the photorefractive effect in electrically polarized media", *J.Elec. Mat.*, 4, pp.915-943, 1975.
2. M.Tanimura and K.Uchino, "Effect of impurity doping on photostriction in ferroelectric ceramics", *Sensors and Materials*, 1, pp.47-56, 1988.
3. K.Uchino, "Micro walking machines using piezoelectric actuators", *J.Rob.Mech.*, 1, pp.124-127, 1989.
4. A.G.Chynoweth, "Surface space-charge layers in barium titanate", *Phys. Rev.* 102, pp.705-714, 1956.
5. A.M.Glass, D. von der Linde and T.J. Negran, "High-voltage bulk photovoltaic effect and the photorefractive process in  $\text{LiNbO}_3$ ", *J. Appl.Phys.Lett.*, 25, pp.233-235, 1974.
6. Philip S.Brody and Frank Crowne, "Mechanism of the high voltage photovoltaic effect in ceramic ferroelectrics", *J.Elec. Mat.*, 4, pp.995-971, 1975.
7. P. Poosanaas, A.Dogan, A.V.Prasadarao, S.Komarneni, and K.Uchino, "Photostriction of sol-gel processed PLZT ceramics", *Journal of Electroceramics*, 1, pp.101-105, 1997.
8. P. Poosanaas, A. Dogan, A. V. Prasadaraao, S. Komarneni, and K.Uchino, "Effect of ceramic processing methods on photostrictive ceramics", submitted to *Journal of Advanced Performance Materials*, 1997.
9. Philip S.Brody, "High voltage photovoltaic effect in barium titanate and lead titanate-lead zirconate ceramics", *J. Solid State Chem.*, 12, pp.193-200, 1975.

Further author information ..... to be placed in the footnote

K.T.(correspondence): Email: tonooka@hniri.go.jp; Telephone: +81-11-857-8954; Fax: +81-11-857-8900  
 P.P.: Email: pxp138@psu.edu; Telephone: 814-865-2434; Fax: 814-865-2326  
 K.U.: Email: kxu1@psu.edu; Telephone: 814-863-8035; Fax: 814-865-2326

## Figure captions

Fig.1. Experimental setup for photovoltaic measurements. An external voltage was applied to give a bias voltage to the sample.

Fig.2. Typical current-voltage curve of photovoltaic effect in PLZT under a UV illumination. The photovoltage defined as the open-circuit voltage was determined from the linear extrapolation of the current-voltage relation.

Fig.3. Linear and nonlinear relations between induced polarizations and electric field; (a) in a linear dielectric and (b) in a crystal lacking inversion symmetry.

Fig.4. Current-voltage characteristics of photovoltaic PLZT at room temperature illuminated with various intensities by a mercury lamp.

Fig.5. Photoconductivity as a function of illumination intensity. Logarithmic scales were used to find the best fit exponent. Experimental results gave a good agreement with the recombination model of photocarriers.

Fig.6. Photocurrent as a function of illumination intensity. The linear dependence found in the experimental results suggested that the photoinduced *dc* field was proportional to the square root of the illumination intensity. The parameter  $\gamma$  was estimated to be 0.46 by the curve fitting based on eq.(16).

Fig.7. Photovoltage as a function of illumination intensity. Curve fitting by an exponential function similar to eq.(16) gave a good fit to experimental data.

Fig.8. Photocurrent measured for a thin PLZT. Curve fitting to the experimental data was made by using eq.(16), giving  $\gamma = 0.8$  as the best fit value. Comparing this value with that in Fig.6, an increase in  $\gamma$  for a thinner sample was observed.

Fig.1 Experimental setup for photovoltaic measurements.

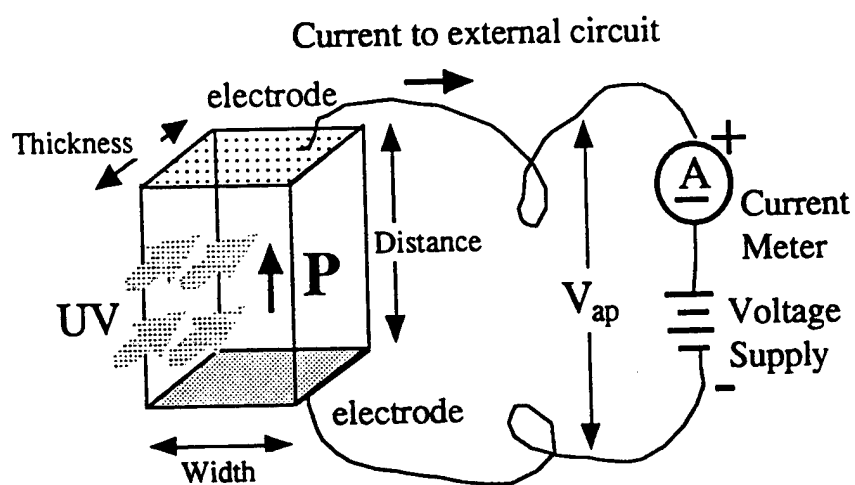


Fig.1. Tonooka

Fig. 2. Tonooka

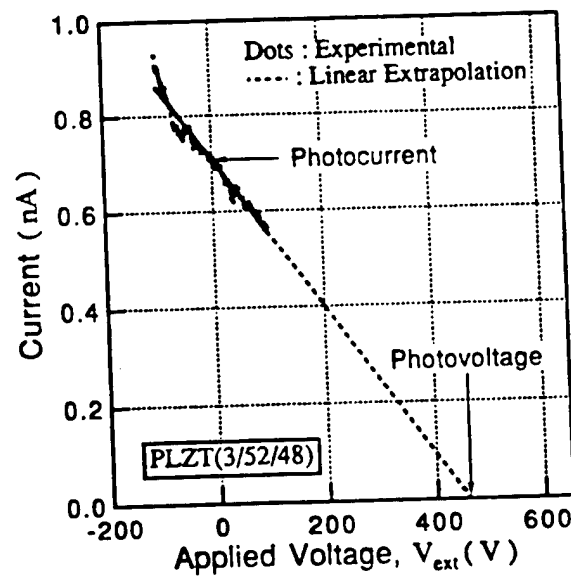


Fig. 2. Typical current-voltage curve of photovoltaic effect.



Fig.3 Tonooka

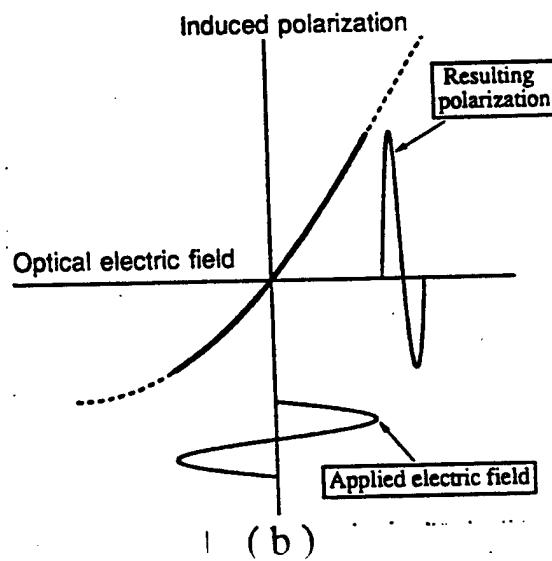
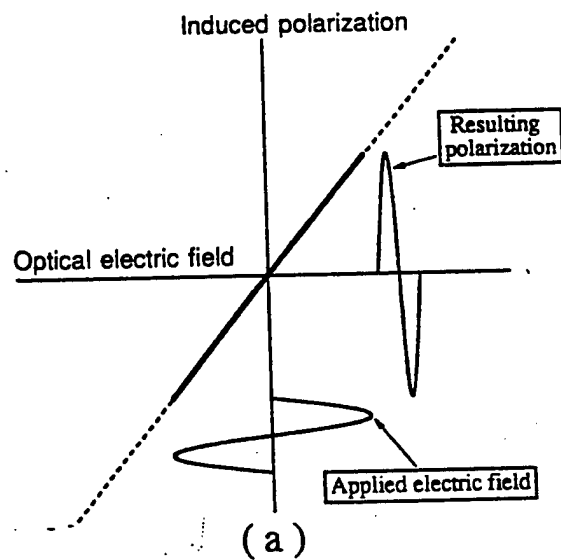


Fig.3.

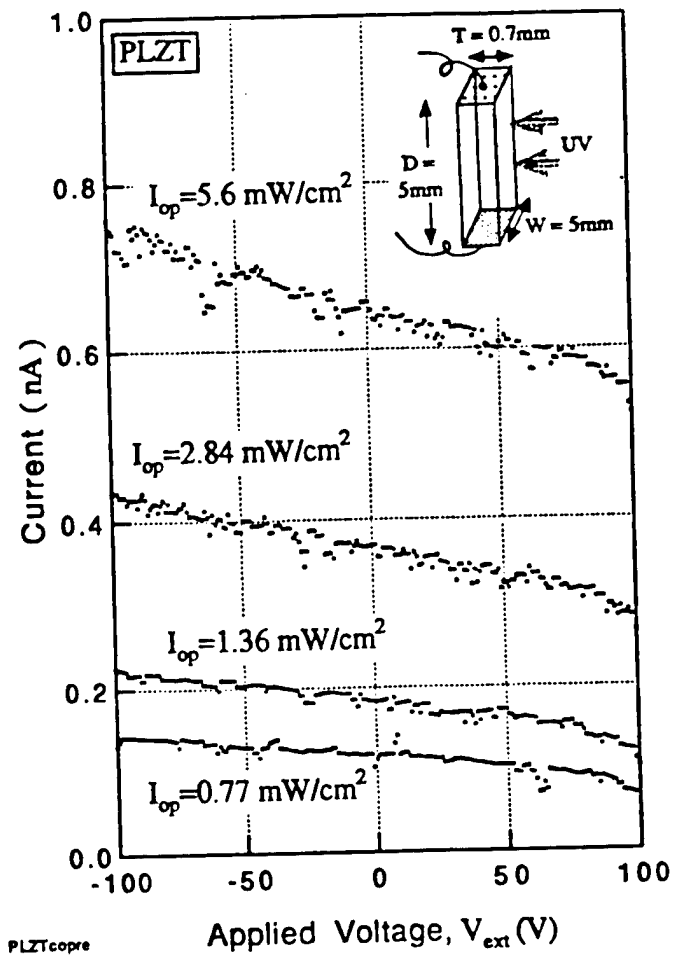
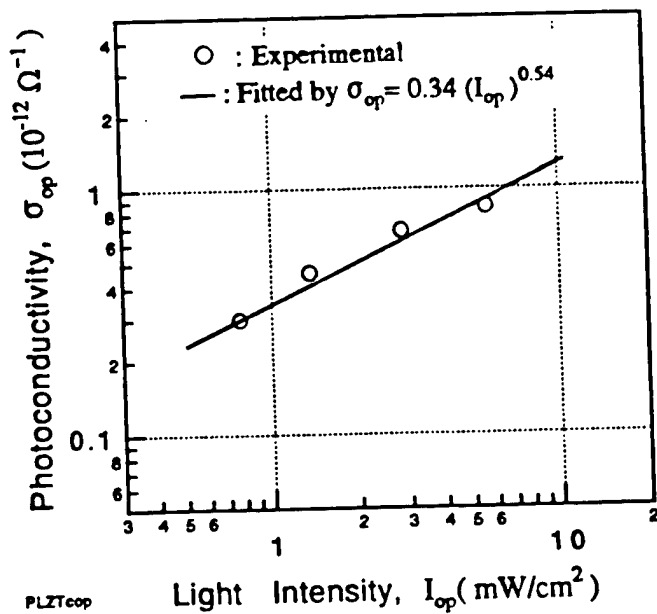


Fig. 4.



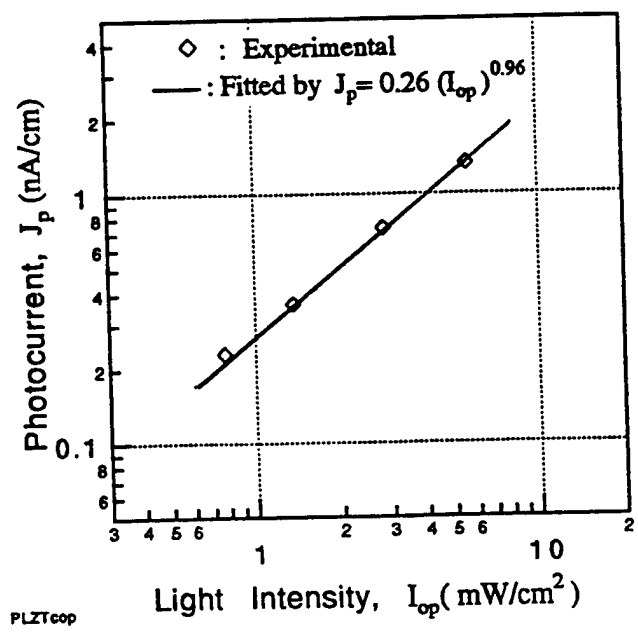


Fig. 6

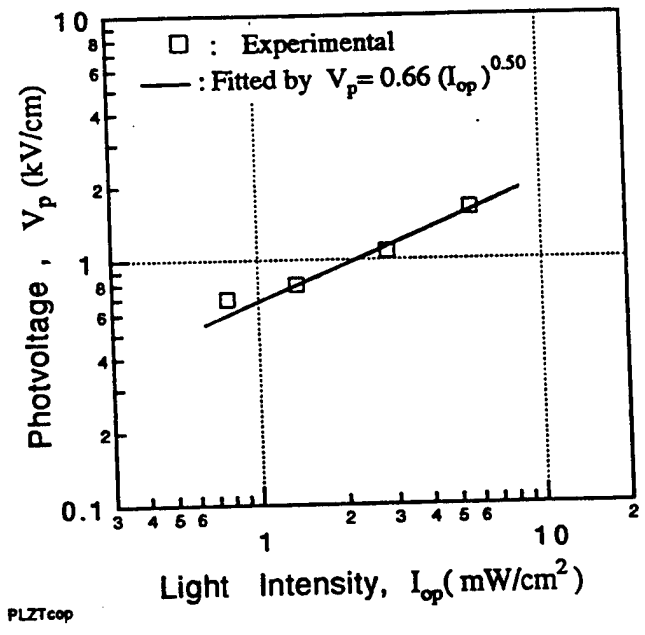


Fig. 7

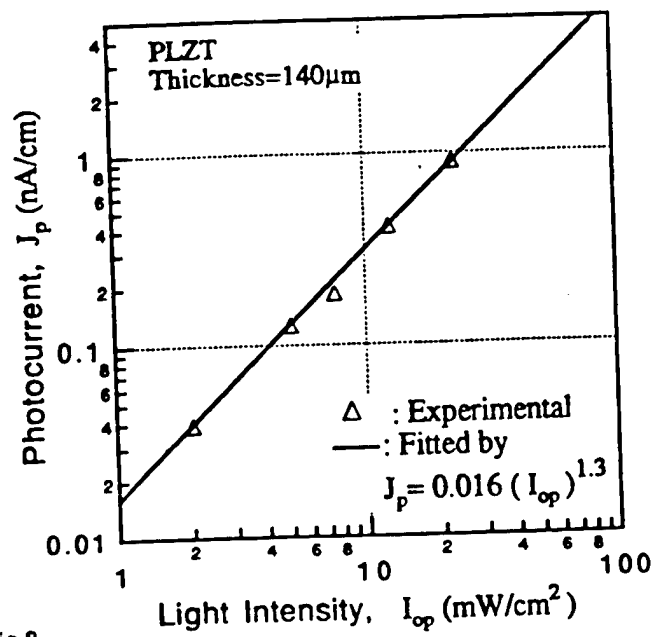


Fig.8

Fig. 8 Tonooka

# **APPENDIX 64**

## Dependence of Photostriction on Sample Thickness and Surface Roughness for PLZT Ceramics

Patcharin Poosanaas, A. Dogan\*, S. Thakoor\*\*, and K. Uchino

International Center for Actuators and Transducers, Materials Research Laboratory  
The Pennsylvania State University, University Park, PA 16802

\* Ceramic Engineering Department, Anadolu University, Eskisehir, Turkey

\*\* Jet Propulsion Laboratory, California Institute of Technology, CA 91109

**Abstract** The ferroelectric materials with high photovoltaic properties are of interest for the new optical devices such as photostrictive ceramic actuators. In pursuit of these high performance photostrictive materials, the present research examines the influence of sample thickness and surface roughness on photostriction of  $\text{WO}_3$  doped PLZT ceramics. A model for the calculation of optimum sample thickness having maximum photostrictive response is proposed. This model agrees well with the experimental results, and it will help in designing the photostrictive devices.

### INTRODUCTION

Photostriction is the light induced strain in a material by the virtue of photovoltaic and inverse-piezoelectric effect. Lanthanum-modified lead zirconate titanate (PLZT) is one of the proven photostrictive materials which are of interest for their potential usage as wireless photo-driven actuators, relays, and micro-robots [1,2]. The photostrictive effect is driven by the absorption of illumination in the surface layer of ceramics. Therefore, the surface characteristics such as sample thickness and surface roughness of the photostrictive material are expected to have strong bearing on the generation of photovoltage and photocurrent.

In the present work, ceramics of PLZT (3/52/48) doped with 0.5 at.%  $\text{WO}_3$  have been prepared by the conventional oxide mixing process. The dependence of photostrictive properties on sample thickness and surface roughness are examined. A theoretical model is proposed to quantify the influence of sample thickness on photovoltaic response. This model, well validated through experimental measurements, will help in optimizing the sample thickness of photostrictive materials.

### EXPERIMENTAL PROCEDURE

PLZT (3/52/48) ceramics with 3 at.% La and a Zr/Ti ratio of 52/48 and 0.5 at.%  $\text{WO}_3$  as dopant were prepared by the conventional oxide mixing process, where  $\text{PbCO}_3$ ,  $\text{La}_2\text{O}_3$ ,  $\text{ZrO}_2$ ,  $\text{TiO}_2$  and dopants ( $\text{WO}_3$ ) were mixed in the proper ratio and ball milled for 48 h. Subsequently, the slurry was dried, calcined at 950 °C for 10 h, and sintered at 1270 °C for 2 h. The detail of the process has been reported elsewhere [3].

PLZT samples were cut to the standard size of  $4 \times 5 \text{ mm}^2$  with various thickness 50  $\mu\text{m}$  -1 mm. Samples were polished, electroded with silver paste and electrically poled along the length (5 mm) direction in silicone oil at 120 °C under a 2 kV/mm for 10 min. Photovoltaic measurements were done by using a high-

input-impedance electrometer (Keithley 617) while the photostriction was measured by a displacement sensor (LVDT, Millitron model 1301). A high pressure mercury lamp (Ushio Electric USH-500D) was used as a light source. The white radiation was passed through an IR blocking filter and an UV bandpass filter to obtain a beam with a maximum strength around 370 nm wavelength. The 4x5 mm<sup>2</sup> polished surface of the sample was illuminated. The experimental set-up for photovoltaic and photostrictive measurements was reported in an earlier paper [3].

## RESULTS and DISCUSSION

### Sample Thickness Dependence

When a sample is illuminated, the incident radiation is absorbed as it penetrates into the crystal lattice. The amount of light intensity reaching at the thickness 'x' of the sample is given as:

$$I(x) = I_0 e^{-\alpha x} \quad (1)$$

where  $I(x)$  is the light intensity at thickness 'x',  $I_0$  is the incident light intensity respectively,  $\alpha$  is the absorption coefficient of the sample.

The absorption coefficient ( $\alpha$ ) was determined by measuring incident and transmitted light intensity, using a digital power meter (Newport model 815), as a function of sample thickness.

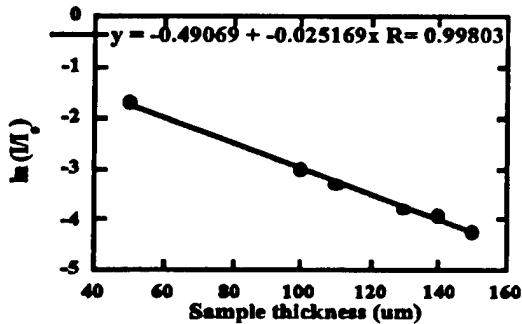


Figure 1: Light intensity as a function of sample thickness

Fig. 1 shows the plot between light intensity as a function of sample thickness. The absorption coefficient, determined from the slope of this plot was found to be 0.0252 μm<sup>-1</sup>.

In case of thinner sample, there will be substantial intensity 'I' throughout the sample thickness, whereas for thick sample after some distance the intensity 'I' will be very small or negligible. The relationship between light intensity and photocurrent density formulated by Glass [4] is given as:

$$J_p h = k \alpha I \quad (2)$$

where  $J_{ph}$  is photocurrent density, and  $k$  is photovoltaic coefficient. It is apparent from Eq. (2), that the photocurrent will increase with the intensity of radiation, resulting in a higher photocurrent in the thinner samples. As is expected, photocurrent increases (Fig. 2) with decrease in the sample thickness.

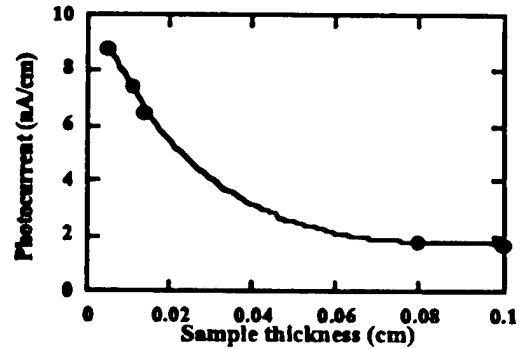


Figure 2: Photocurrent as a function of sample thickness

The relationship between sample thickness and photovoltaic response has been illustrated in Fig. 3. In this model, the absorption coefficient is assumed to be independent of light intensity and the photocurrent density is taken to be proportional to light intensity. The sample is assumed to comprise of thin slices along the thickness direction of the sample. A circuit diagram representing these layers is also shown in the same figure.

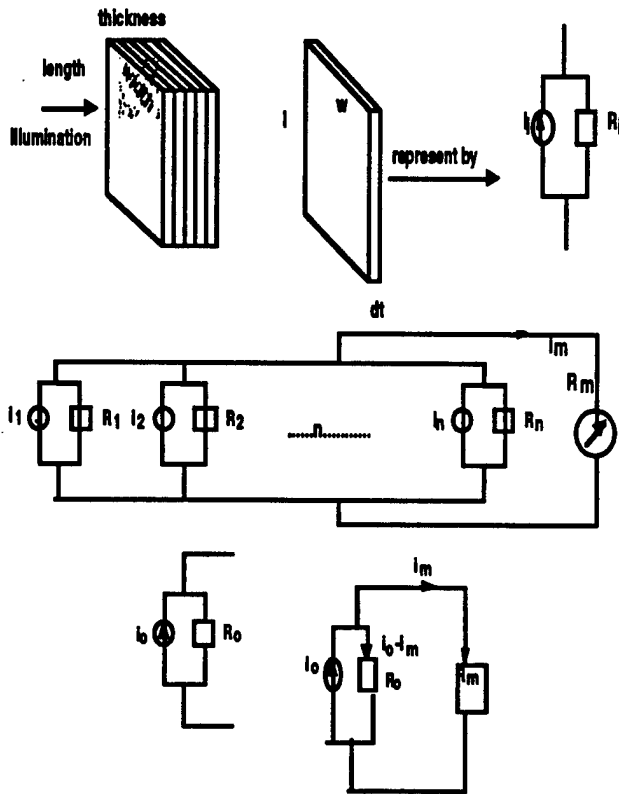


Figure 3: A proposed model for dependence of photocurrent on sample thickness

The photocurrent flowing through one of the layer of thickness 'dx', located at a distance of 'x' from the sample surface, can be obtained by combining Eq. (1) and (2):

$$di_0 = wk\alpha I_0 e^{(-\alpha x)} dx \quad (3)$$

where  $di_0$  is the photocurrent in this layer and  $w$  is the sample width. The total photocurrent  $i_0$  passing through the sample can be obtained by integrating Eq. (3), over the sample thickness:

$$i_0 = \int_0^t wk\alpha I_0 e^{(-\alpha x)} dx = wkI_0(1 - e^{(-\alpha t)}) \quad (4)$$

The conductivity of this layer ( $\sigma_x$ ) can be expressed as a sum of dark conductivity ( $\sigma_d$ ) and photoconductivity ( $\sigma_{ph}$ ), given as:

$$\sigma_x(x) = (\sigma_d + \sigma_{ph} I_0 e^{(-\alpha x)}) \quad (5)$$

The total sample conductance ( $G_0$ ) (i.e. inverse of resistance) can be obtained by integrating Eq. (5), over the sample thickness.

$$G_0 = \frac{1}{R_0} = \int_0^t \frac{w\sigma_x dx}{L} = \frac{w}{L} [\sigma_d t + \frac{\sigma_{ph} I_0 (1 - e^{(-\alpha t)})}{\alpha}] \quad (6)$$

where  $L$  is the electrode gap (length of the sample). In order to measure the photocurrent an external load of resistance  $R_m$  was used. The sample and external load are correlated as following:

$$R_0(i_0 - i_m) = R_m i_m \quad (7)$$

where  $i_m$  is the measured photocurrent and  $R_m$  is the external load (Keithley 617) resistance. The Eq. (4), (6) and (7) can be rearranged as:

$$i_m = \frac{wkI_0(1 - e^{(-\alpha t)})}{1 + R_m w (\frac{\alpha t}{L} + \frac{\sigma_{ph} I_0 (1 - e^{(-\alpha t)})}{\alpha L})} \quad (8)$$

Fig. 4 shows the plot between  $i_m$  (normalized with  $k$ ) and sample thickness calculated for the external resistance ( $R_m = 200 \text{ T}\Omega$ ).

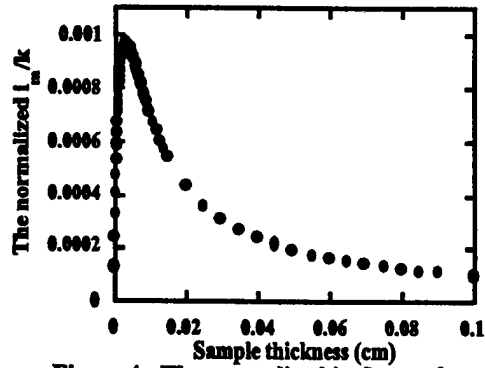


Figure 4: The normalized  $i_m/k$  as a function of sample thickness

As is evident from this figure, with increasing in sample thickness,  $i_m$  increases, reaches a maxima, and subsequently it decreases with the sample thickness. The optimum thickness (for the current set of samples) which yield maximum photocurrent is found at  $32 \mu\text{m}$  which is about the penetration depth of light. It must be noted that the samples used in this study are thicker than this optimum thickness.



It is also reflected in results shown in Fig. 2, where the photocurrent is found to increase with decrease in sample thickness.

### Surface Roughness Dependence

In order to observe the surface roughness effect, PLZT ceramics (3/52/48) with different surface roughness were prepared by using SiC powder of different grit size followed by final finishing with diamond paste. The surface roughness was measured by a profilometer (Tencor, Alpha-step 200). The average surface roughness was determined using the graphical center line method. Fig. 5 exhibits the photostriction of undoped PLZT as a function of surface roughness.

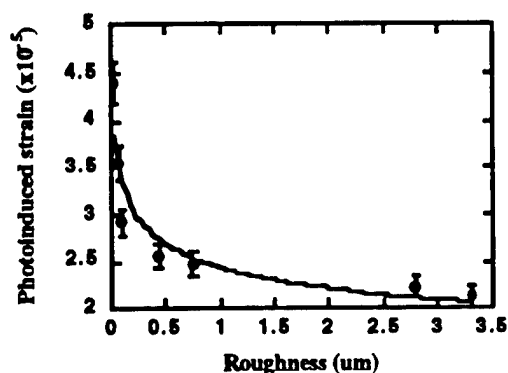


Figure 5: Photoinduced strain as a function of surface roughness

As is evident from this figure, photoinduced strain increases exponentially with the decrease in surface roughness. With increasing surface roughness, the penetration depth of the illumination decreases. This result also reiterates that photostriction is a surface effect and surface preparation is of extreme importance in the fabrication of high efficiency photostrictive materials.

## CONCLUSIONS

In the present study, dependence of photovoltaic and photostrictive properties on sample thickness and surface roughness of  $\text{WO}_3$  doped PLZT ceramics was investigated. The surface nature of photostriction was examined by using samples with different thickness and surface roughness. Photovoltaic response was found to increase with decrease in sample thickness. A model for the calculation of optimum sample thickness having maximum photostrictive response has been proposed. The optimum sample thickness for the sample used in present study is calculated to be  $32 \mu\text{m}$ . This model agrees well with the experimental results, and it will be very useful in designing the photostrictive devices. The photostrictive effect was observed to strongly decrease with an increase in sample surface roughness.

## REFERENCES

- [1] K. Uchino, "New Applications of Photostriction," *Innovations in Materials Research*, vol. 1, no. 1, pp. 11-22, 1996.
- [2] T. Sada, M. Inoue, and K. Uchino, "Photostriction in PLZT Ceramics," *J. Ceram. Soc. Jpn. Inter. Ed.*, vol. 95, pp. 499-504, 1987.
- [3] P. Poosanaas, A. Dogan, A.V. Prasada Rao, K. Komarneni and K. Uchino, "Photostriction of Sol-Gel Processed PLZT Ceramics," *J. Electroceramics*, vol. 1, no. 1, pp. 105-111, 1997.
- [4] A. M. Glass, D. von der Linde, D. H. Auston, and T. J. Negran, "Excited State Polarization, Bulk Photovoltaic Effect and the Photorefractive Effect in Electrically Polarized Media," *J. Electronic Materials*, vol. 4, no. 5, pp. 915-943, 1975.

# **APPENDIX 65**

## Photostriction of Sol-Gel Processed PLZT Ceramics

PATCHARIN POOSANAAS, A. DOGAN, A.V. PRASADARAO, S. KOMARNENI & K. UCHINO

*International Center for Actuators and Transducers, Materials Research Laboratory, The Pennsylvania State University, University Park, PA 16802, USA*

Received October 29, 1996; Revised January 13, 1997; Accepted January 13, 1997

**Abstract.** Lanthanum-modified lead zirconate titanate (PLZT) ceramic materials have gained considerable attention due to their photostriction, which is the superposition of photovoltaic and piezoelectric effects. However, the photovoltaic effect and the induced strain response are also influenced by the fabrication and processing conditions. The PLZT ceramics produced by conventional oxide mixing process exhibit moderate photostrictive properties due to the inhomogeneous distribution of impurities. In this study, ceramics of PLZT (3/52/48) doped with  $\text{WO}_3$  and  $\text{Nb}_2\text{O}_5$  were prepared by sol-gel technique using lead(II) acetate trihydrate, lanthanum(III) acetylacetonate hydrate, Zr, Ti, Nb, and W alkoxides. It was found that  $\text{WO}_3$  and  $\text{Nb}_2\text{O}_5$  were effective in suppressing the grain growth of PLZT, which lead to the enhancement of photovoltaic and photostrictive properties. Photovoltaic and photostrictive responses showed a maximum for samples with 0.5 at%  $\text{WO}_3$  doped sol-gel PLZT. It has been shown that the sol-gel derived PLZT ceramics with proper density possess the possibility of enhancing the photostriction over ceramics produced by conventional oxide mixing process.

**Keywords:** photostriction, photovoltaic effect, sol-gel, PLZT, doping effect, tungsten, niobium

### Introduction

Lanthanum-modified lead zirconate titanate (PLZT) ceramics are known to exhibit a range of interesting electro-optical properties. The advantages of PLZT ceramics are their high optical transparency, desirable electrooptic properties, and fast response (Xu, 1991). There have been many successful demonstrations of the applications of PLZT. Recently, the application of PLZT in photostrictive actuators has drawn considerable attention (Uchino and Aizawa, 1985; Uchino et al., 1985; Sada et al., 1987; Chu et al., 1994; Chu and Uchino, 1995).

Photostrictive effect is the superposition of the photovoltaic and piezoelectric effects. This effect is of interest in the development of wireless remote control photodriven actuators. Another promising application will be in the new generation photoacoustic devices. Photovoltaic effect and the strain response have been shown to vary greatly for the different preparation processes, even in materials with the same composi-

tion (Sada et al., 1987). In a ceramic material for electro-optic application, a combination of good ferroelectricity and high transparency is required. This requirement can be met by a ceramic material with high density, low porosity, and a homogeneous composition. However, the conventional oxide mixing process provides inhomogeneous distribution of impurities, resulting in moderate photostriction properties. The sol-gel process, involving chemical precipitation (solution reaction) for preparation of powder materials, has gained attention in comparison to the conventional techniques due to its inherent advantages in producing high density homogeneous powder with a greater control on stoichiometry (Chiou and Kno, 1990; Rahaman, 1995). In addition, the obtained powders are finely divided and greatly enhanced in reactivity, sinterability and transparency over powders prepared by the conventional processing.

In this study, ceramics of PLZT (3/52/48) doped with  $\text{WO}_3$  and  $\text{Nb}_2\text{O}_5$  were prepared by both the

conventional oxide mixing process and the sol-gel technique using lead(II) acetate trihydrate, lanthanum(III) acetylacetonate hydrate, Zr, Ti, Nb, and W alkoxides. The photostrictive effect and its dependence on dopant and fabrication method were investigated.

### Experimental Procedure

PLZT (3/52/48) ceramics with 3 at% La and a Zr/Ti ratio of 52/48 was selected due to its highest photovoltaic effect [2]. PLZT (3/52/48) doped with 0.5 at%  $\text{WO}_3$  and various concentrations of  $\text{Nb}_2\text{O}_5$  were prepared by the conventional oxide mixing process and the sol-gel technique. Figure 1 illustrates a flow chart for the sample preparation by the conventional oxide mixing process. In this method,  $\text{PbCO}_3$ ,  $\text{La}_2\text{O}_3$ ,  $\text{ZrO}_2$ ,  $\text{TiO}_2$  and dopants ( $\text{WO}_3$  or  $\text{Nb}_2\text{O}_5$ ) were mixed in the proper ratio corresponding to the composition and ball milled for 48 h. The slurry was dried and calcined at  $950^\circ\text{C}$  for 10 h. The calcined

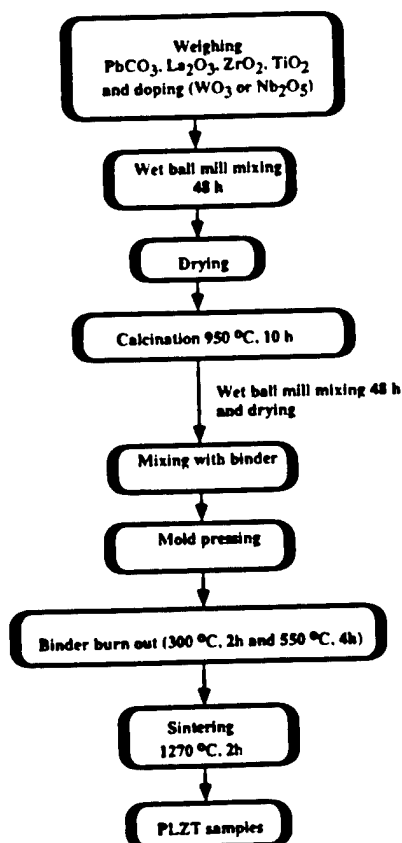


Fig. 1. Flow diagram of sample preparation by oxide mixing process.

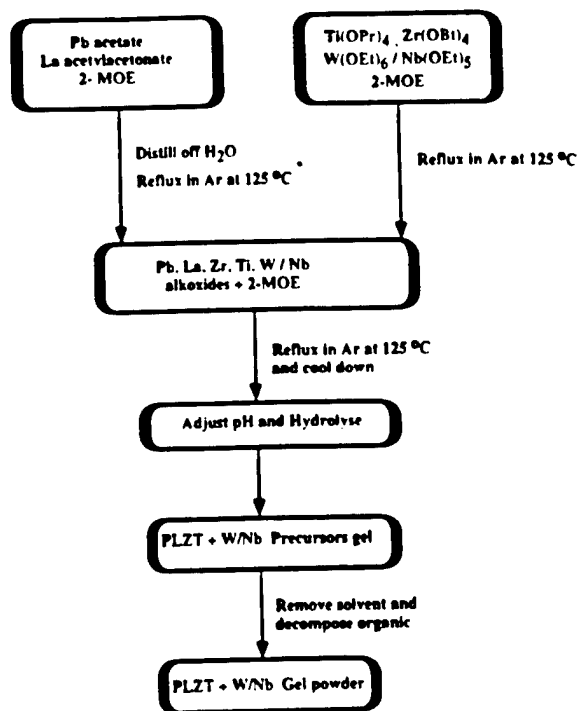


Fig. 2. Flow diagram of sample preparation by sol-gel process. 2-MOE: 2-methoxyethanol,  $\text{Ti}(\text{OPr})_4$ : Titanium(IV) isopropoxide,  $\text{Zr}(\text{OBu})_4$ : Zirconium(IV) butoxide,  $\text{W}(\text{OEt})_6$ : Tungsten(VI) ethoxide,  $\text{Nb}(\text{OEt})_5$ : Niobium(V) ethoxide.

powder was further ball milled for 48 h and subsequently sintered in air at  $1270^\circ\text{C}$  for 2 h. The flow chart for the sample preparation by the sol-gel technique has been shown in Fig. 2. In the sol-gel processing, lead(II) acetate trihydrate,  $\text{Pb}(\text{CH}_3\text{COO})_2 \cdot 3\text{H}_2\text{O}$ , lanthanum(III) acetylacetonate hydrate,  $\text{La}(\text{acac})_3 \cdot \text{H}_2\text{O}$ , zirconium(IV) butoxide,  $\text{Zr}(\text{OC}_4\text{H}_9)_4$ , and titanium(IV) isopropoxide,  $\text{Ti}(\text{OC}_3\text{H}_7)_4$ , were used as precursors while tungsten(VI) ethoxide,  $\text{W}(\text{OC}_2\text{H}_5)_6$  and niobium(V) ethoxide,  $\text{Nb}(\text{OC}_2\text{H}_5)_5$ , were used as dopants and 2-methoxyethanol (2-MOE) was used as a solvent. Pb and La precursors were mixed in the proper ratio and dissolved in 2-MOE and used as precursor site A. The solution was distilled and refluxed at  $125^\circ\text{C}$  and cooled to room temperature. Precursor site B comprising of Zr, Ti and dopant were mixed in the proper ratio using 2-MOE as a solvent. The solution was refluxed in Ar at  $125^\circ\text{C}$  and cooled to room temperature. Subsequently, the solution was added into the reflux solution of site A and was refluxed in Ar at  $125^\circ\text{C}$ . The pH of this solution was adjusted to 10 by using nitric acid, before its hydrolysis. The solution was then aged to yield a gel which was dried

to obtain the powder. After the removal of organics at 400°C for 6 h, the powder was calcined at 600°C for 1 h and sintered at 1250°C for 2 h in air.

The density of the sintered samples was determined by the Archimedes method. Microstructure and grain size of the samples were observed by scanning electron microscopy (ISI-SX-40X Scanning Electron Microscope, International Scientific Instruments, Inc., NY). Dielectric properties of PLZT samples were measured with an impedance analyzer (HP-4274A). Samples for dielectric measurements were polished to about 10 mm in diameter and 1 mm in thickness, then electroded with platinum (Pt) by sputtering. Piezoelectric properties of all the samples were measured by using a Berlincourt  $d_{33}$  meter (Channel Products, Inc.) at 100 Hz. Samples for piezoelectric measurement were of the same configuration as for dielectric measurements, except they were poled in silicone oil at 120°C under a 2 kV/mm electric field for 10 min.

Photovoltaic measurements were done by using a high-input-impedance electrometer (Keithley 617), while the photostriction measurement was done by using the displacement sensor (LVDT, Millitron model 1301). These measurements were done by radiating the light perpendicular to the polarization direction. The samples of  $5 \times 5 \times 1 \text{ mm}^3$  were cut and polished for these measurements. The  $5 \times 1 \text{ mm}^2$  surfaces were silver electroded. Poling was performed by applying 2 kV/mm electric field for 10 min. in silicone oil at 120°C. A high pressure mercury lamp (Ushio Electric USH-500D) was used as a light source for the measurement. The white radiation was passed through an IR blocking filter and an UV bandpass filter to obtain a beam with a maximum strength

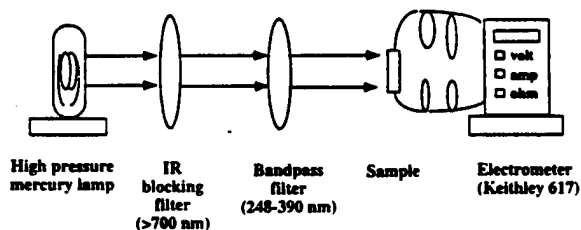


Fig. 3. Experimental set up for photovoltaic measurement.

#### Illumination

- High pressure mercury lamp
- Without polarizer
- Filter
  - IR blocking filter
  - Bandpass filter
- Wavelength - 370 nm
- Intensity - 3.25 mW/cm<sup>2</sup>.

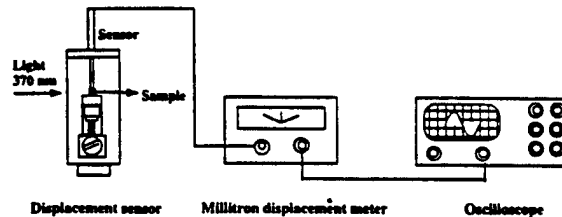


Fig. 4. Experimental set up for photostrictive measurement.

around 370 nm and an intensity of 3.25 mW/cm<sup>2</sup>, before illuminating the samples ( $5 \times 5 \text{ mm}^2$  polished surface). The light beam with this wavelength has been reported to yield the maximum photovoltaic properties (Uchino et al., 1985). The experimental set-up for photovoltaic and photostriction measurements are shown in Figs. 3 and 4, respectively.

## Results and Discussion

### Relative Density

Figure 5 shows the relative sintered density of Nb<sub>2</sub>O<sub>5</sub> doped PLZT as a function of sintering temperature. A relative density of 98% was achieved for PLZT oxide samples sintered at 1200°C. The sintered density saturated and remained constant as the sintering temperature increased to 1300°C. On the other hand, in the sol-gel PLZT a maximum density of 91% was observed at a sintering temperature of 1250°C. The

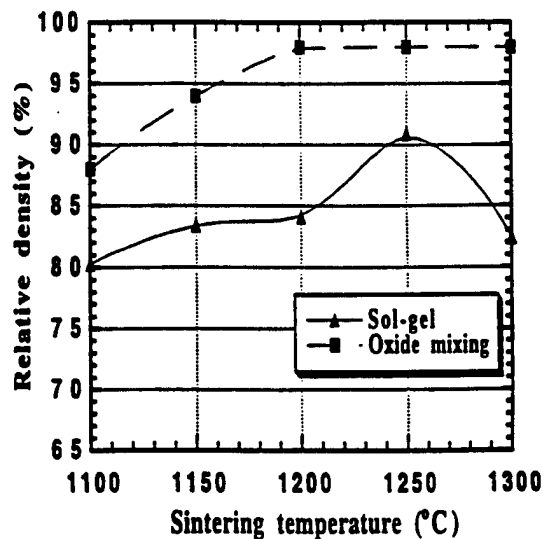


Fig. 5. Relative density as a function of sintering temperature after 2 h sintering.

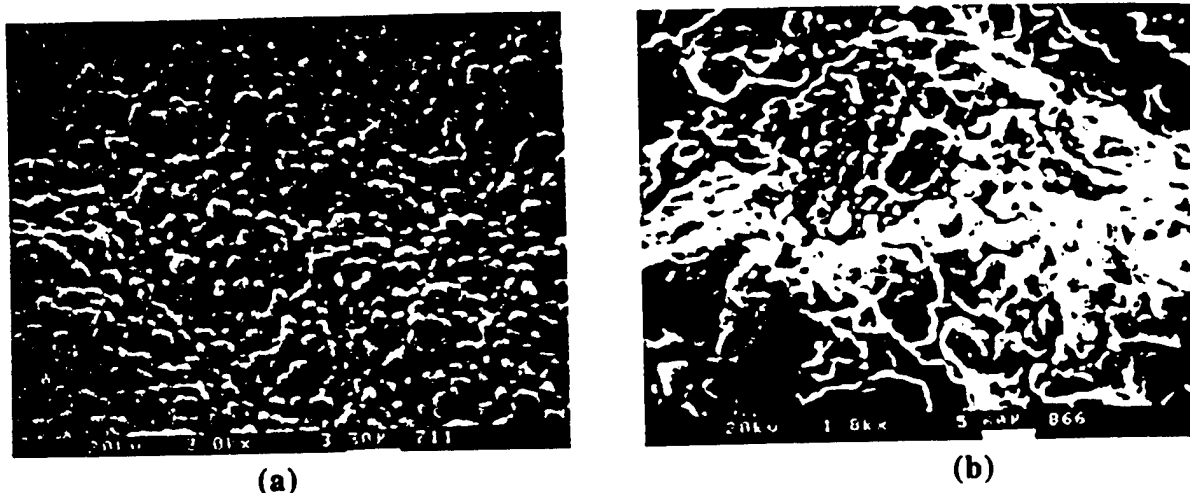


Fig. 6. SEM micrographs of 1.0 at%  $\text{Nb}_2\text{O}_5$  doped PLZT ceramics prepared by (a) oxide mixing (b) sol-gel methods.

sintered density decreased as the sintering temperature was further increased. This was probably due to the evaporation of  $\text{PbO}$  during sintering. As evident from Fig. 5, the sol-gel PLZT exhibits lower density as compared to the oxide PLZT at all the sintering temperatures. This lower density was probably due to finer and agglomerated particles, resulting in aggregation which was observed in some areas of  $\text{Nb}_2\text{O}_5$  doped sol-gel PLZT. However, the aggregation was not observed in 0.5 at%  $\text{WO}_3$  doped sol-gel PLZT, which is one reason for the higher relative density of this ceramic (93%) than  $\text{Nb}_2\text{O}_5$  doped sol-gel PLZT. The high density in PLZT oxide samples is probably

due to higher packing density without agglomeration as compared to sol-gel ceramics. Figure 6 shows the SEM micrographs of the sintered ceramic surfaces. The 1.0 at%  $\text{Nb}_2\text{O}_5$  doped sol-gel PLZT in (b) clearly showed large pores which were caused by the particle agglomeration.

#### Grain Size

The average grain size is shown in Fig. 7 as a function of doping concentration. The average grain size decreases with increasing doping concentration.  $\text{Nb}_2\text{O}_5$  was found to be more effective in suppressing

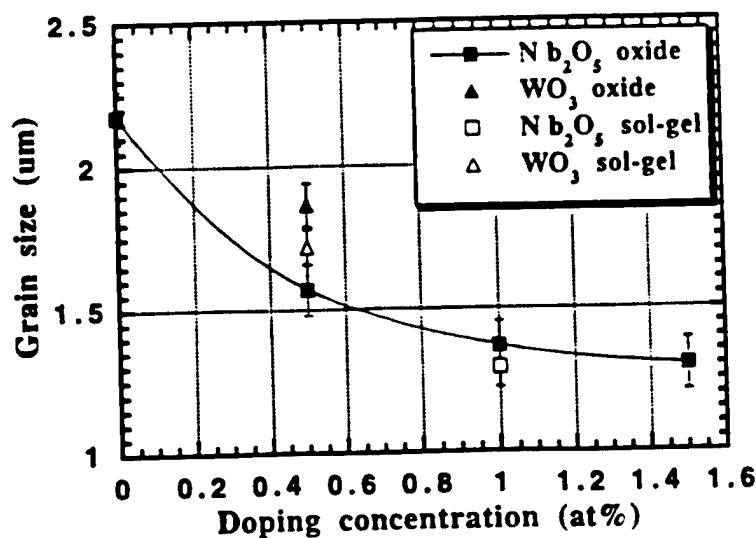


Fig. 7. Variation of average grain size with doping concentration.

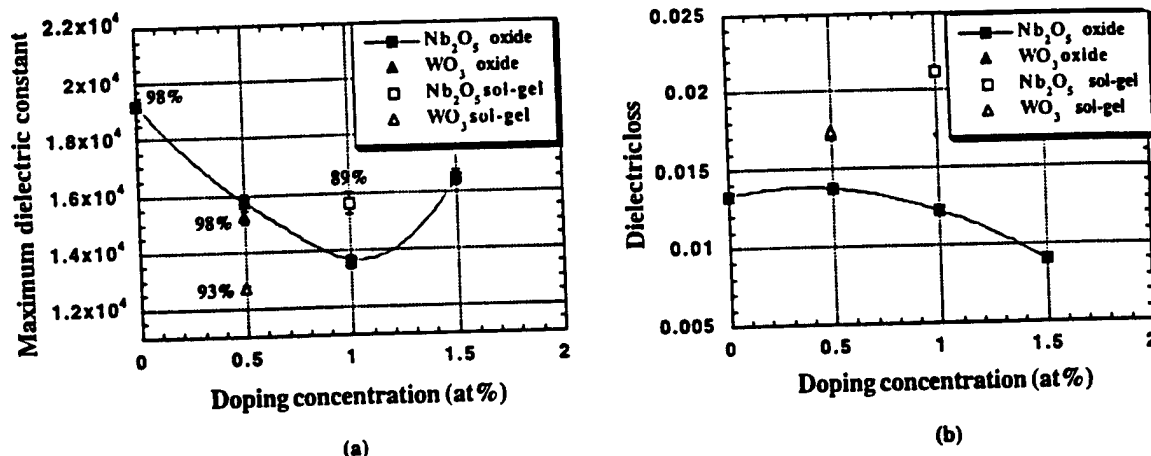


Fig. 8. Variation of (a) maximum dielectric constant (b) maximum dielectric loss with doping concentration.

the grain size as compared to  $\text{WO}_3$  as a dopant. The grain size of the sol-gel ceramics was smaller than that of the oxide mixing ceramics when sintered at  $1250^\circ\text{C}$  for 2 h.

#### Dielectric and Piezoelectric Properties

Figure 8(a) shows the change in the maximum dielectric constant with doping concentration. The number shown in the figure represents the relative density of the samples at each composition. The dielectric loss ( $\tan \delta$ ) as a function of doping

concentration is shown in Fig. 8(b). The maximum dielectric constant was found to decrease with increasing doping concentration for the case of oxide mixing samples. This was partially due to the lower grain size observed in PLZT doped oxide mixing ceramics. The dielectric constant showed a minimum at 1.0 at%  $\text{Nb}_2\text{O}_5$  doped oxide PLZT. Also, the sol-gel PLZT doped with  $\text{WO}_3$  has a lower dielectric constant compared to the oxide PLZT due to the smaller grain size. However, the  $\text{Nb}_2\text{O}_5$  doped sol-gel PLZT exhibits higher dielectric constant as compared to the oxide PLZT at the same composition.

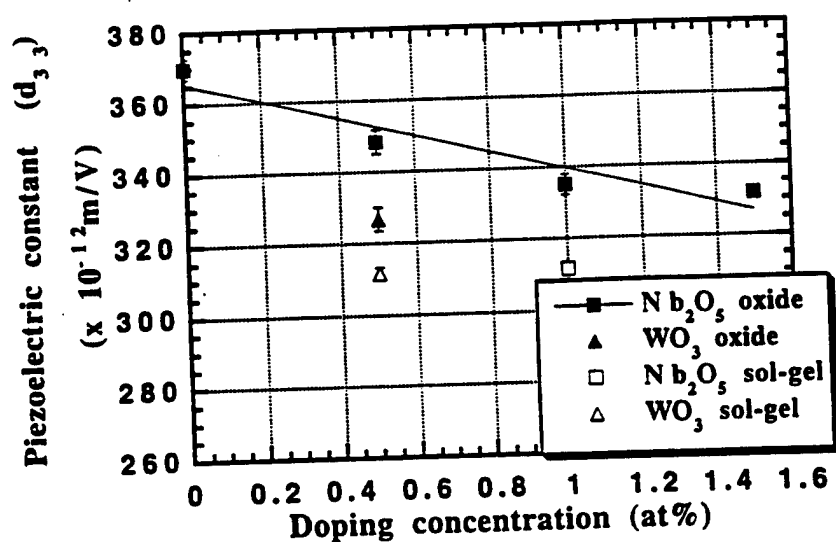


Fig. 9. Variation of piezoelectric constant with doping concentration.

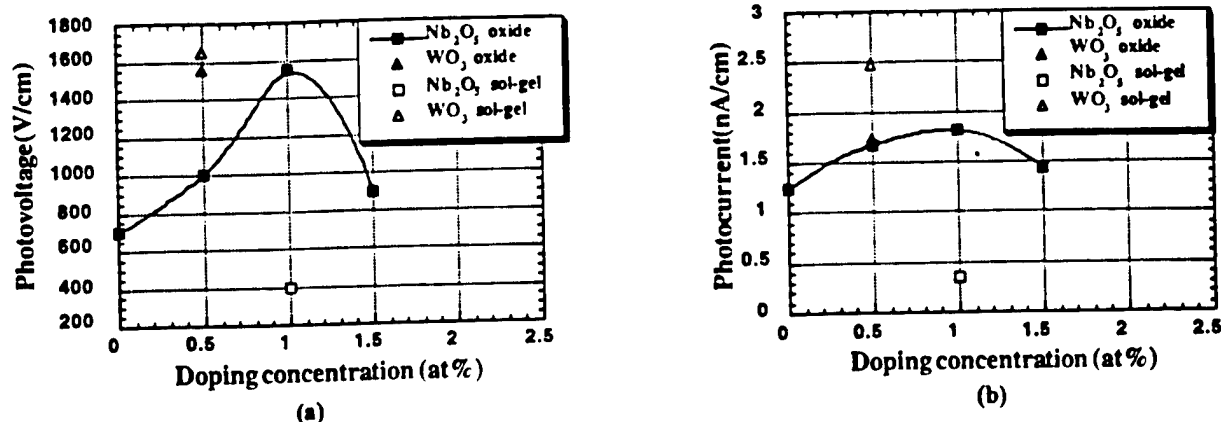


Fig. 10. Variation of (a) photovoltage (b) photocurrent with doping concentration.

This may be due to the high dielectric loss observed in this ceramic (Fig. 8(b)). Higher dielectric loss in sol-gel samples may be due to loss through grain boundaries and pores.

The piezoelectric constant as a function of doping concentration is shown in Fig. 9. The measured value of  $d_{33}$  decreases with increasing doping concentration. Also, the sol-gel ceramics exhibit lower  $d_{33}$  as compared to the oxide ceramics. With decrease in grain size, the domain wall contribution to the piezoelectric properties drops off, leading to this decrease in piezoelectric constant.

#### Photovoltaic and Photostrictive Properties

Figure 10 shows the variation of photovoltaic responses with doping concentration for the samples doped with WO<sub>3</sub> and Nb<sub>2</sub>O<sub>5</sub>. All dopants were found to enhance the photovoltaic responses. The photo-

voltage reached more than 1 kV/cm and the photocurrent was of the order of nA/cm. As in the previous papers, the current density was normalized only with respect to the width of the illuminated surface, but not to the depth. Both the photovoltage and photocurrent revealed a maximum at 1 at% of doped Nb<sub>2</sub>O<sub>5</sub> in the oxide PLZT. WO<sub>3</sub> doped sol-gel PLZT showed the maximum photovoltaic response among all the samples. This may be attributed to higher degree of homogeneity and uniform distribution of dopant and a stoichiometry in compositions for this sample. Lower photovoltaic properties were observed in Nb<sub>2</sub>O<sub>5</sub> doped sol-gel PLZT. In general, increase in photovoltage will enhance photostriction and increasing photocurrent will increase the response speed. The photostriction is estimated as the product of the photovoltage and the piezoelectric coefficient (Uchino and Aizawa, 1985; Sada et al., 1987; Chu and Uchino, 1995). It can be expressed by

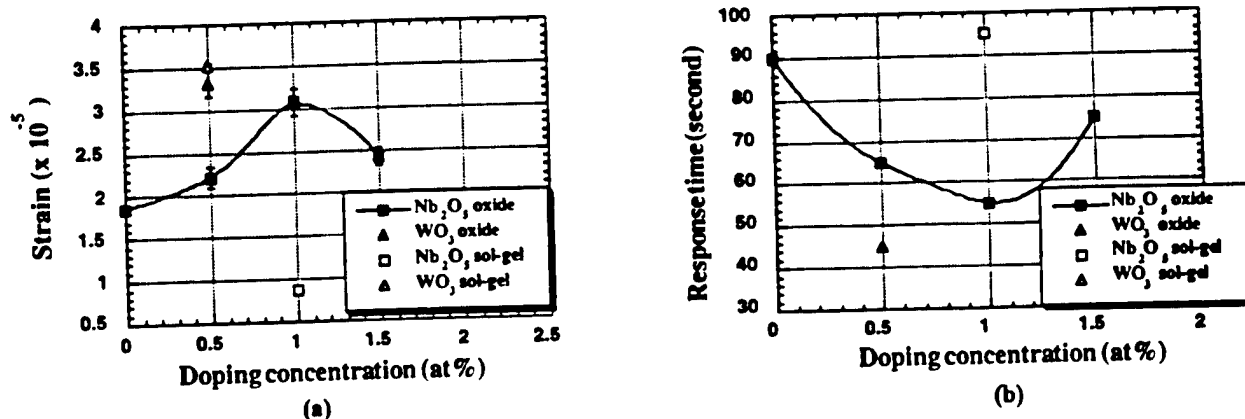


Fig. 11. Variation of (a) photoinduced strain (b) response time with doping concentration.



$$x_{ph} = d_{33}E_{ph}(1 - \exp(-t/RC))$$

where  $x_{ph}$  is photoinduced strain,  $d_{33}$  is piezoelectric coefficient,  $E_{ph}$  is the saturated photovoltage,  $t$  is time,  $R$  is the resistance, and  $C$  is the capacitance of samples.  $RC$  is referred to as time constant or response speed which suggests that a sample with high photocurrent will give fast response speed as compared to slow response samples. These effects are confirmed in Figs. 11(a) and 11(b), where the change in photostriction and response speed are shown as a function of doping concentration. Similar changes in photovoltaic behavior with doping concentration was observed in the photostrictive effect. The maximum photostriction was found in  $WO_3$  doped sol-gel PLZT. In the  $Nb_2O_5$  doped oxide PLZT, the largest photostriction was observed in the sample with 1.0 at%  $Nb_2O_5$ . Also, the  $WO_3$  doped sol-gel PLZT exhibited the fastest response time among all the samples. The fastest response time among  $Nb_2O_5$  doped oxide PLZT, was obtained at 1.0 at%  $Nb_2O_5$ . The lower photostriction and the slow response speed in  $Nb_2O_5$  doped sol-gel PLZT can be due to the agglomeration of fine powder which resulted in a lower density.

## Conclusions

$WO_3$  and  $Nb_2O_5$  were effective in suppressing the grain growth which leads to the enhancement of photovoltaic and photostrictive properties in PLZT. Although  $WO_3$  was less effective in suppressing the grain size, due to its inherent dopant property, it was more effective in enhancing the photovoltaic and photostrictive responses. Dielectric and piezoelectric properties were found to decrease with increasing doping concentration due to the smaller grain size. In general, the dielectric and piezoelectric properties can be enhanced by doping with donors such as  $WO_3$  and  $Nb_2O_5$ . However, they also decrease with decreasing grain size due to a drop in domain wall contribution. The lower dielectric and piezoelectric properties found in doped ceramics indicate the dominance of the grain size effect. Although the relative density of sol-gel PLZT is lower than oxide PLZT at the same composition, the preliminary results showed that the maximum photovoltaic and photostrictive effect were

obtained for 0.5 at%  $WO_3$  doped sol-gel PLZT. This may suggest that a better homogeneity and a closer control of stoichiometry in sol-gel technique as compared to oxide mixing process give rise to higher photovoltaic and photostrictive properties. The aggregation and low density observed in  $Nb_2O_5$  doped sol-gel PLZT was the reason for lower photovoltaic and photostrictive responses as compared to the  $WO_3$  doped sol-gel PLZT.

In conclusion, the preliminary results in this study suggest that the sol-gel technique possesses the possibility in enhancing the photostriction in PLZT. It must also be noted that if the density of sol-gel processed PLZT can be increased through particle size distribution and by controlling the agglomeration, even further improvement in photostrictive response will be achieved.

## Acknowledgments

This work is partially supported by Army Research Office through Grant No. DAAL 03-92-G-0244. One of the authors (P. Poosanaas) would like to acknowledge the Royal Thai Government and Dr. Harit Sutabutr from the National Metal and Materials Technology Center (Thailand) for granting a MOSTE fellowship.

## Bibliography

- Chiou, B.-S. and Kno, J.N., 1990, The Preparation of PLZT Ceramics from a Sol-Gel Process, *J. Elec. Mater.*, 19(4), 393-397.
- Chu, S.-Y. and Uchino, K., 1995, Photostrictive Effect in PLZT-Based Ceramics and its Application, *Ferroelectrics*, 174, 185-196.
- Chu, S.-Y., Ye, Z., and Uchino, K., 1994, Photovoltaic Effect for the Linearly Polarized Light in (Pb, La) (Zr, Ti)  $O_3$  Ceramics, *Smart Mater. Struct.*, 3, 114-117.
- Rahaman, M.N., 1995, Ceramic Processing and Sintering, Marcel Dekker Inc., New York, 207.
- Sada, T., Inoue, M., and Uchino, K., 1987, Photostriction in PLZT Ceramics, *J. Ceram. Soc. Jpn.*, Inter. Ed., 95, 499-504.
- Uchino, K. and Aizawa, M., 1985, Photostrictive Actuator Using PLZT Ceramics, *Jpn. J. Appl. Phys. Suppl.*, 24, 139-141.
- Uchino, K., Aizawa, M., and Nomura, S., 1985, Photostrictive Effect in (Pb, La) (Zr, Ti)  $O_3$ , *Ferroelectrics*, 64, 199-208.
- Xu, Y., 1991, Ferroelectric Materials and Their Application, Elsevier Science Pub. Co., New York, 164.